DEVELOPMENT OF A PATIENT-SPECIFIC FINITE ELEMENT MODEL OF THE TRANSCATHETER AORTIC VALVE IMPLANTATION (TAVI) PROCEDURE

University of Cape Town

Mohammad Mehdi Shirzadi

Department of Mechanical Engineering

UNIVERSITY OF CAPE TOWN

April 2016

The copyright of this thesis vests in the author. No quotation from it or information derived from it is to be published without full acknowledgement of the source. The thesis is to be used for private study or non-commercial research purposes only.

Published by the University of Cape Town (UCT) in terms of the non-exclusive license granted to UCT by the author.

University of Cape Town

Submitted in fulfilment of the requirements for the degree of

Master of Science in Mechanical Engineering

at the University of Cape Town

Declaration

I know the meaning of plagiarism and declare that all the work in the document, save for that which is properly acknowledged, is my own. This thesis/dissertation has been submitted to the Turnitin module (or equivalent similarity and originality checking software) and I confirm that my supervisor has seen my report and any concerns revealed by such have been resolved with my supervisor.

Signature: ..... 

Date: 16/7/2016

Acknowledgements

I would like to thank my supervisor Professor Daya Reddy for all of his continuous guidance, encouragement and support throughout this project. Further, I would like to thank my co-supervisor Dr. Harish Appa, and express my gratitude to Strait Access Technologies for providing the topic, funding and the necessary data for this project. I would like to also thank Dr. Greg Mitchell for his assistance with Abaqus. I would like to express my heart felt appreciation to my parents, Dr. and Mrs. Shirzadi for all their support towards the completion of this project. Finally, I would like to thank all my friends at CERECAM for their help and encouragement.

Abstract

Transcatheter Aortic Valve Implantation (TAVI) is a procedure developed for replacing the defective aortic valve of a patient as an alternative to open heart Surgical Aortic Valve Replacement (SAVR). In the TAVI procedure a prosthetic valve, which is assembled on to a stent, is crimped and delivered to the patient's aortic root site through several available percutaneous means. The percutaneous nature of TAVI, which is its core advantage in comparison to other SAVR procedures, can however also be its main disadvantage. This is due to lack of direct access to the calcified leaflets, and hence reliance on the host tissue for the proper positioning and anchorage of the deployed prosthetic valve. Therefore, it is desired to have a preoperative quantitative understanding of patient-specific biomechanical interaction of the stent and the native valve to be able to maximise the chance of success of the procedure.

The aim of this study was to develop a patient-specific Finite Element (FE) model of the Transcatheter Aortic Valve Implantation (TAVI) procedure for two patients, using a model of the 23 mm percutaneous prosthetic aortic valve developed by Strait Access Technologies (SAT), for the purpose of its post-operative performance. In this regard, the image processing software ScanIP was used to extract the 3D models of the patient-specific aortic roots and leaflets from the provided Multi-Slice Computer Tomography (MSCT) images of the patients.

An anisotropic hyperelastic material model was implemented for the roots and leaflets, using two and one families of collagen fibres for their tissues respectively. The stent is made of a cobalt-chromium alloy and its mechanical response was modelled as an isotropic elasto-plastic material, with a linear elastic initial response, followed by plastic behaviour with isotropic hardening. The prosthetic leaflets are made of polymer and were modelled as an isotropic hyperelastic material, using the provided experimental test data. The results for the first patient showed that the stent maintained its structural integrity after deployment, and successfully pushed the native leaflets back to keep the aortic root clear of all impediments. No obstruction of the coronary ostia was observed, and prosthetic leaflets were seen to function normally. The stent radial recoil was calculated to be between 2 to 4.28 % after deployments. Its foreshortening was calculated to be approximately 20%. The stent was observed to move back and forth by approximately 3 mm in the last simulation step in

which cardiac cycle pressure were applied to the aortic root and prosthetic leaflets. Also, two openings were observed between the stent and aortic root wall during this simulation step, which indicates the possibility of paravalvular leakage. From the second patient simulation, it was observed that the 23 mm stent was not a good choice for this patient, and will cause severe damage or tissue tearing. The maximum principal stress in the aortic root and valve tissues were observed to follow approximately the defined collagen fibre directions.

Contents

List of Figures

List of Tables

Nomenclature

Abbreviations

AE	artificial energy
AR	aortic regurgitation
ARF	acute rheumatic fever
AS	aortic stenosis
BAV	balloon aortic valvuloplasty
BAVD	bicuspid aortic valve disease
CAD	computer aided design
CVD	cardiovascular disease
DICOM	digital imaging and communications in medicine
FE	finite element
FEA	finite element analysis
IE	internal energy
KE	kinetic energy
MDCT	multi-row detector computer tomography
MSCT	multi-slice computer tomography
PDE	partial differential equations
RHD	rheumatic heart disease
RVP	rapid ventricular pacing
SAVR	surgical aortic valve replacement
SAT	strait access technologies
TAVI	transcatheter aortic valve implantation

TAVR	transcatheter aortic valve replacement
THV	transcatheter heart valve
VEC	valvular endothelial cells
VHD	vavular heart diseases
VIC	valvular interstitial cells

Greek Symbols

$\emptyset$	diameter
Δ	change
Ψ	Helmholtz free energy function
λ	the stretch along a particular direction
$\boldsymbol{\sigma}$	Cauchy stress
γ	the angle between the two defined family of fibre directions (in degrees)
κ	the constant that specifies the dispersion of fibres
ρ	material density
ω	eigenvalue
∂	partial derivative
$\boldsymbol{\varphi}$	a motion that takes a solid body form its reference to current configuration

Symbols

$\mathbf{u}$	displacement
$\mathbf{u}$	velocity
$\mathbf{u}$	acceleration
Δt	stable time increment
$\mathbf{M}$	diagonal lumped mass matrix
T	period
$f_{structural}$	structural frequency
c_d	dilatational wave speed in a material

E	Young's modulus
L^{e}	characteristic elemental length
$\mathbf{F}$	deformation gradient
$\mathbf{C}$	right Cauchy-Green tensor
I_i	invariants of C
$\mathrm{R}_{\%}^{Recoiled}$	percentage elastic radial recoil
$D_{avg}^{Recoiled}$	average diameter of the recoiled stent after crimping
$D^{Crimped}$	designated crimped diameter of the stent
$\mathrm{L}_{\%}^{Recoiled}$	percentage lengthening of a stent after crimping and recoiling
$L_{avg}^{Recoiled}$	average length of the recoiled stent after crimping
$L_{avg}^{Original}$	average original length of the stent
S1, S2, S3	the three generated meshes for the stent
$\mathcal{B}_0$	a solid body in the reference or unreformed configuration
$\mathcal{B}$	a solid body in the deformed or current configuration
X, Y	material points in the reference configuration
x, y	material points in the current configuration
$\mathbf{a}_{01}$, $\mathbf{a}_{02}$	the two preferred fibre directions in the reference configuration
$\mathbf{a}_1$, $\mathbf{a}_2$	the two preferred fibre directions in the current configuration
$\mathbf{A}_1, \mathbf{A}_2$	second order structural tensors
$\mathbf{Q}$	a proper orthogonal tensor
$\mathbf{S}$	the second Piola-Kirchhoff stress
$\mathbf{I}$	identity tensor
k_1, c_{10}	stress-like material parameters
k_2	a dimensionless material parameter
$\mathrm{R}_{\%}$	percentage radial recoil of the stent after deployment
$D^{Expanded}$	designated expanded diameter of the stent
$D_{avg}^{Deployed}$	average diameter of the recoiled stent after deployment

$L_{\%}$	percentage foreshortening of the stent after deployment
$L_{avg}^{Deployed}$	average length of the deployed stent after recoiling

Units

mm	millimetre
s	seconds
ms	millisecond
mJ	millijoules
mmHg	millimetres of mercury (133.3 pascals)
Hz	hertz
kPa	kilopascal
MPa	megapascal
GPa	gigapascal
deg	degrees
μm	micrometre (micron)

Glossary

Abaqus	A unified finite element analysis software package for computer-aided engineering
Analysis step	The definition of a particular analysis phase in which a specific process is modeled, for which the duration, boundary conditions, loads and output requests desired are specified
Anisotropic	A property that implies directional dependency as opposed to Isotropy, which means similar response in all directions
Atherosclerosis	A disease in which fatty deposits builds up in the arteries, which leads to their narrowing or blockage, and considerably stiffness their tissue
Coronary arteries	The arteries that branch off form the aorta, and supply the heart with blood
Hourglassing	A numerical phenomenon that occurs due to the presence of spurious zero energy modes, and interfere with the true response of the element, which can severely affect the solution accuracy
Hyperelasticity	An idealistic material property that implies recoverability of large elastic strains. The stress-strain relation in hyperplastic material are driven form a strain energy density function.
Lesion	An abnormal change or injury in a section of a tissue
Lumen	A term that refers to a cavity within a blood vessel or an organ in some medical imaging modalities. In CT imaging modality, blood appears a luminous medium
Mesh	A term given to a collection of elements that has been designated to represent a structure in a finite element analysis simulation
Percutaneous	A term meaning “through the skin” which is given to a medical procedure in which accesses to inner organs is achieved through needle-puncture

Shear locking	A numerical phenomenon that results in the prevalence of parasitic shear stresses that absorbs strain energy, which results in smaller bending displacement and stiffer reaction
Stenosis	The narrowing of a passage or blood vessel in the body
Valvuloplasty	The process of widening a stenotic aortic valve by using a balloon
Viscoelastic	A material property that implies rate dependency and viscous-elastic response during deformations

Chapter 1

Introduction

This chapter introduces the topic of this thesis and presents its background. It also mentions the approach taken and the result of some of the similar studies reviewed, and defines the scope and objectives of the project. It concludes with a presentation of the the structure of the thesis.

1.1 The global burden of valvular heart disease

According to the World Heart Federation, Cardiovascular Disease (CVD) is the leading global cause of death [1]. In 2012, an estimated 17.5 million deaths occurred due to CVD and this number is expected to grow to more than 23.6 million by 2030 [1,2]. Africa's contribution to this figure in 2012 was 1.25 million, approximately 7.2%, with CDV remaining as the second most common cause, after infectious diseases, in most African countries and as one of the top five in South Africa [1,3].

One of the major branches of CVD is Valvular Heart Diseases (VHD) and its burden is rising mainly due to two reasons; prevalence of Rheumatic Heart Disease (RHD), which occurs due to Acute Rheumatic Fever (ARF), and degeneration. The heart has four valves that allow for unidirectional flow of blood from atria to ventricles, namely the tricuspid and the mitral valve, and from ventricles to the aorta and the pulmonary artery, namely the aortic and the pulmonic valve [4]. Permanent damage to the heart valves tissue, mainly the mitral/aortic valve or both, is the associated symptom of ARF that can become chronic leading to congestive heart failure, endocarditis, stroke and death [5].

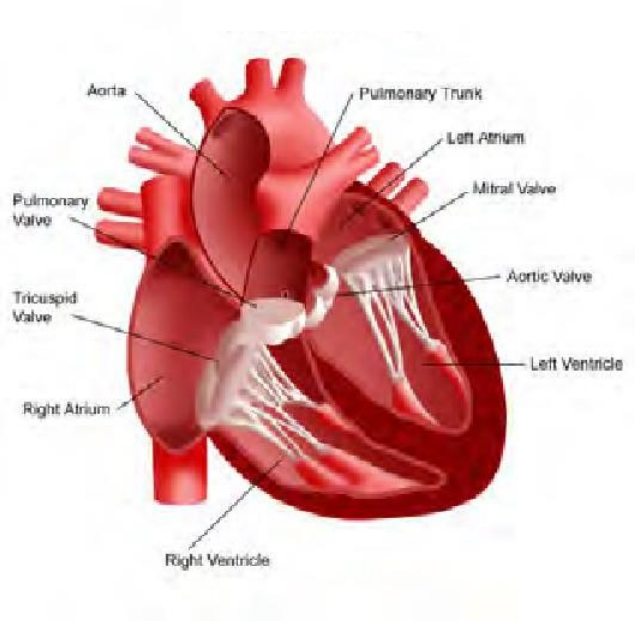

Figure 1.1 *Valves of the heart [6].*

Although ARF is a significant public health concern globally, it is the developing nations specifically that are bearing the brunt. In Africa, ARF is the predominant cause of VHD and mainly affects children and young adults [7]. Sub-Saharan Africa has the highest prevalence of RHD with 5.7 per 1000 as compared to North Africa with 1.8 per 1000 and the developed countries with 0.3 per 1000 [7].

In the developed countries, the main cause of aortic VHD is degeneration as a result of ageing, since rheumatic disease has substantially reduced due to improved living conditions. According to the collected data of 5001 patients with mean age of 64 ± 14 years across Europe in 2001 who had significant primary VHD or infective endocarditis, the most common lesion was aortic stenosis (43%) followed by mitral regurgitation (32%), aortic regurgitation (13%) and mitral stenosis (12%) [8]. The main aetiologies of aortic stenosis and regurgitation along with mitral regurgitation were degeneration, whilst 85% of the cases with mitral stenosis were due to RHD [8,9]. The global prevalence of clinically significant aortic stenosis in patients over 70 is approximately 1 to 3% and it is estimated that up to 40% of those aged 60 or over, and 75% of those aged over 85 have mild calcified aortic valve [9].

1.2 Treatment of aortic valve disease

Surgical Aortic Valve Replacement (SAVR) remains the gold standard methodology [10] to treat severe aortic valve disease/defect. Generally there are two types of SAVR: open heart (full sternotomy) and minimally invasive [10]. In open heart SAVR, the surgeon makes a 10 inch-long cut in the middle of the patient's chest to expose the heart and the aortic root. A

heart-lung bypass machine will be used to take over the normal operation of the heart and lung for the duration of the procedure [11]. The patient's aortic valve is then removed and a new mechanical or biological valve is sutured in place. With regard to the minimally invasive approach, the incision length is considerably smaller than the full sternotomy and its location varies according to the surgeon's decision based on the optimal location for accessing the aortic valve.

The general advantage of the minimally invasive approach includes less trauma, less pain, faster recovery, less blood loss and therefore decreased transfusion requirements, less risk of infection, better cosmetic results and decreased cost. Most definitely there are also disadvantages associated with minimally invasive procedures and therefore not all patients are appropriate candidates.

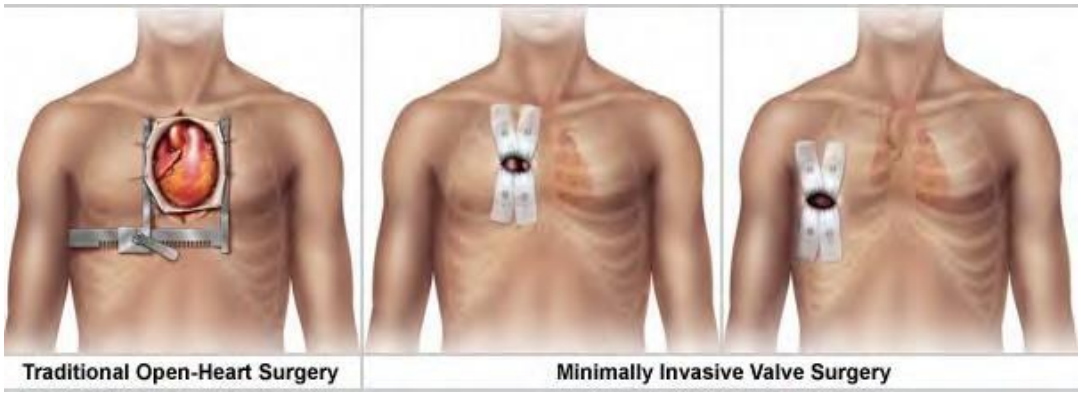

Figure 1.2 *A Schematic drawing of open heart and minimally invasive SAVR (from [12]).*

The implanted prosthetic valves used in open heart and minimally invasive aortic valve replacement surgeries are of two types (see Figure 1.3): mechanical and biological. The advantage of mechanical valves in comparison to biological valves is that, ideally, they would not degrade over the life span of the patient. However, anticoagulation medication should be used by the patient for the remainder of his/her life to prevent blood clotting. With regard to the biological valves, however, no anticoagulation medication is necessary, but these valves have a life span limitation associated with them and have an average life of about ten to fifteen years. Therefore, most probably, the patient would need a second SAVR at about 15 years from the initial surgery [13].

In recent years, a new intervention has been developed as a result of a major advancement in the prosthetic heart valve designs. Transcatheter Aortic Valve Implantation (TAVI) or Transcatheter Aortic Valve Replacement (TAVR) is a new method in which a specially developed, balloon expandable or self-expanding stented prosthetic valve is delivered to the aortic root location, using a catheter, without the requirement of an incision for the exposure

of the aortic root. With this revolutionary intervention, the procedure time, complexity, trauma and post-operative rehabilitation period are drastically reduced.

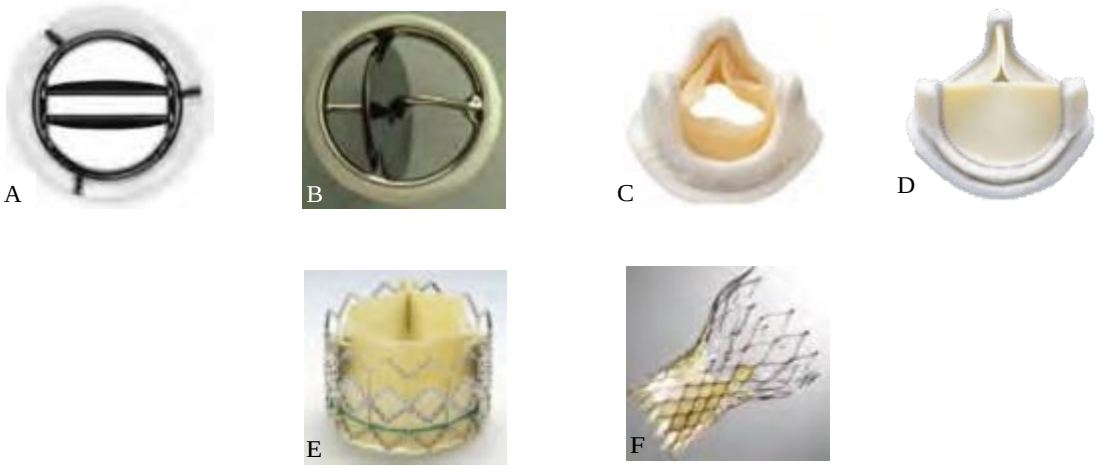

Figure 1.3 *Different types of prosthetic aortic valves: (A) Bileaflet mechanical valve (St Jude); (B) monoleaflet mechanical valve (Medtronic Hall); (C) stented porcine bioprosthetic (Medtronic Mosaic); (D) stented pericardial bioprosthetic (Carpentier-Edwards Magna); (E) percutaneous bioprosthetic balloon expanded (Edwards Sapien); (F) self-expandable percutaneous bioprosthetic (CoreValve) (from [14]).*

According to the EuroHeart survey on VHD [8], as many as one-third of the patients with symptomatic aortic stenosis do not undergo surgical valve replacement due to old age and other comorbidities, such as high-risk cardiac disease and/or lack of referral to surgery. In addition to this group, a significant number of patients in the developing countries, in which RHD is mostly prevalent, are not treated due to lack of adequate healthcare professional and cardiac surgery equipment. For these groups of patients TAVI can provide a new vital option.

1.3 Transcatheter Aortic Valve Implantation (TAVI)

In the mid-1980s, Professor Alain Cribier and his research team developed a minimally invasive procedure for the management of AS. The goal of the Balloon Aortic Valvuloplasty (BAV) was to provide an alternative option for the symptomatic patients with AS who at the time were deemed unable to go through open SAVR, mainly due to age and other comorbidities. BAV allowed for midterm improvement of quality of life of the patients and therefore it was rapidly adopted globally. But due to the lack of survival benefits and high recurrence rate of 80 %, its use was drastically reduced [15].

Building upon the experience gained with BAV, Cribier went on to pursue a long term solution for the treatment of AS and the idea of deploying a prosthetic valve, within the diseased aortic valve emerged. The general concept however was not new. In the 1970s, there had been several experimental projects seeking to treat aortic regurgitation [16,17]. In 1989 Henning-Rud Andersen implanted the first model of a catheter-mounted balloon-expandable stented valve in the aorta of pigs [18]. Philip Bonhoeffer performed the first human implantation of a stented bovine jugular vein conduit, which he developed, in a right ventricle to pulmonary artery in 2000 [19]. From the late 1980s to the year 1999, Cribier and his team worked on and developed the first balloon-expandable transcatheter heart valve (THV) through international collaboration and did considerable amount of laboratory work and animal trials. The first human implantation of the developed valve was carried out by him in 2002 and the result was excellent [15]. Since then, there has been great interest in TAVI and many medical/engineering research groups and biomedical companies have done extensive studies on this technology in order to improve the design of the valve, both hemodynamically and structurally, and develop better materials to increase its chance of success.

1.3.1 Percutaneous valves and the TAVI procedure

The specially designed percutaneous-type valves that make TAVI possible, are comprised of three leaflets (biological or polymeric) to mimic an actual human tri-leaflet aortic valve. These leaflets are mounted in a stent structure that has the ability to be crimped to a small diameter, in order to be delivered to the deployment site using a catheter and through the arteries. The balloon expandable valves are usually made of medical-grade stainless steel or cobalt-chromium, and are specifically designed to withstand the large elastic-plastic strains that they are subjected to during the crimping and expansion processes. In addition to this, they are able to tolerate the cyclic biomechanical loading due to cardiac cycle, and have excellent durability against corrosion. The self-expandable valves, on the other hand, are mainly made of Nitinol (Nickel-Titanium), which is a super-elastic metallic alloy that is mostly known for its shape memory property [20].

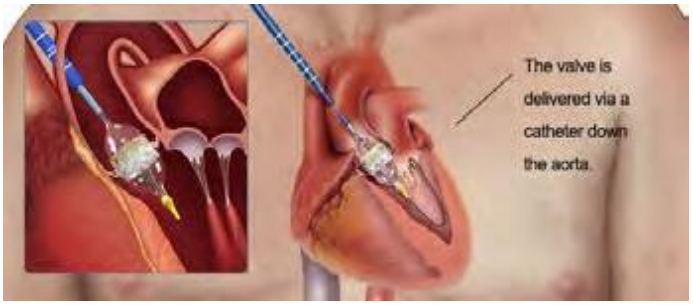

Figure 1.4 *A graphical representation of transaortically delivered Edwards SAPIEN valve (from [21]).*

TAVI procedure is performed using fluoroscopy, which is a real-time X-ray imaging modality that allows for planar visualization of the entire process [22]. Due to the nature of the TAVI procedure that limits the surgeons from having direct access to the native aortic valve, pre-surgery echocardiography and Multi-Row Detector Computer Tomography (MDCT also known as Multi-Slice Computer Tomography MSCT) are utilized to visualize the patient's aortic root [23]. These images allow for performing the required annular measurements, and aid in determination of the severity of the leaflets calcification. They are also often used for finding an appropriate fluoroscopic projection angle for having an orthogonal view of the deployment site during the TAVI procedure [24].

In order to ensure the success of the intervention and prevent any post-operative incidents relating to suboptimal anchorage of the stent, its size is chosen based on the native valve's "annular" diameter, measured during the systolic phase of the patient's cardiac cycle. This is because typically the annulus is the tightest section of the native valve and will provide the first anchorage load on the stent. Valvuloplasty might be used prior to the deployment of the prosthetic valve to dilate the aortic root's annulus and "soften" the highly stiff leaflets to allow for proper siting of the stent [25]. Rapid Ventricular Pacing (RVP) might be induced to temporarily arrest left ventricle ejection for the duration of valve deployment [26]. The TAVI procedure can be done either under general anaesthetic or conscious sedation, and the patient does not need to be connected to a heart-lung machine. The actual implantation procedure usually takes about an hour, and the patient is normally discharged after a week or two post-surgery.

Currently there are four approaches by which the prosthetic valve is delivered to the root; transfemorally, transapically, transaortically or via the subclavian artery. Depending on the condition of the patient, surgeons choose the type of valve and delivery approach that has the highest chance of success.

1.3.2 Challenges associated with TAVI and the need for a reliable predictive tool

The percutaneous nature of TAVI, which is its core advantage in comparison to the SAVR procedures, can also be its main disadvantage. This is due to lack of direct access of the surgeons to the calcified leaflets and hence reliance on the host tissue for the proper positioning, maintenance and function of the deployed prosthetic valve. Some of the published intraoperative and postoperative adverse events of TAVI procedure include aortic injury due to excessive radial expansion force during deployment [27], paravalvular leak or impairment of coronary flow or both, stroke, cardiac tamponades [28] and valve migration [29]. Figure 1.5 shows two fluoroscopic images from a published case report [29] of a TAVI intervention taken immediately after the prosthetic valve deployment and 43 days later when the patient complained of acute shortness of breath. It was found that the implanted valve had rotated and migrated caudally into the left ventricle, partially obstructing the

inflow of the mitral valve. Open heart surgery was performed to retrieve the implanted valve and replace the native malfunctioning valve.

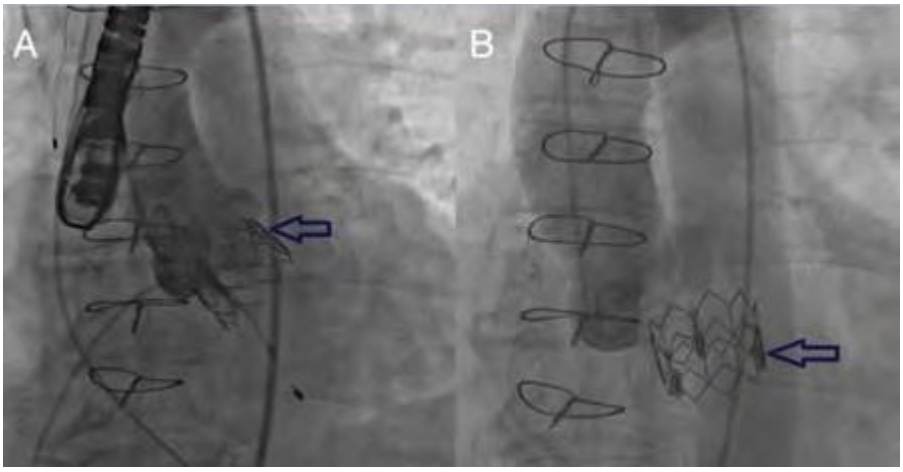

Figure 1.5 *Fluoroscopic images of a TAVI procedure showing the position of implanted valve when deployed (A) and when rotated and migrated in to the left ventricle (B) (form [29]).*

From these events and some of the clinical published data, it can be deduced that surgeons are not able to predict reliably the outcome of the procedure due to the nature of the intervention. In the absence of a reliable predictive tool, surgeons are left to rely on personal experiences, guidelines from the prosthetic valve manufacturers and published reports on previous interventions to be able to make decision regarding the optimal valve size and positioning site. In this regard, Professor Tirone E. David, a pioneer in heart valve surgery, states that "like most reconstructive procedures in cardiac surgery, the actual performance of the operation remains more art than science" [30]. It is therefore essential to have a preoperative quantitative understanding of patient-specific biomechanical interaction of the prosthetic valve and the native valve to be able to maximise the chance of success in the TAVI procedure [31].

In recent years, close collaboration between cardiac surgeons and engineers has led to the development of patient-specific Finite Element (FE) models of TAVI procedures that can be used as a predictive tool by surgeons to be able to perform trial deployment simulation and assess the results.

1.4 Modelling of the aortic root, its tissue properties and the patient-specific TAVI procedure

1.4.1 Patient-specific three-dimensional model of the aortic root

For the creation of a finite element model of a patient-specific prosthetic valve deployment procedure, a three-dimensional computer model of the patient's aortic root must be extracted from the pre-operative cardiac MDCT imagies. Currently a few medical image processing software packages, such as ScanIP (Simpleware Ltd, Exeter, UK) and Mimics (Materialise, Leuven, Belgium), are available for conversion of MDCT images to modifiable three-dimensional computer models. These models are initially imported into a Computer Aided Design (CAD) software to be processed, and are then imported into a Finite Element Analysis (FEA) software package for analysis.

1.4.2 The aortic root and valve tissue property and constitutive material model

The first mathematical studies on the aortic valve were carried out in the 1970's [32,33] to characterize the mechanics of the leaflets and computed the stress and strain distributions on them. Over the past two decades, many computational and experimental studies have been conducted to determine the valve's tissue properties for the purpose of material modelling, and to gain a better understanding of its general functioning, pathology and biomechanics. The aortic root's tissue is known to be nearly incompressible and exhibit viscoelastic, anisotropic and nonlinear behaviour [34]. However, to have a reproducible and stabilized mechanical response, preconditioning loading is used to reduce tissue hysteresis [35].

Billiar et al. [36] developed a specialized biaxial testing technique and performed several experiments using natural and glutaraldehyde treated specimens of porcine aortic leaflets tissue for the purpose of property data generation and hence constitutive model development. The results confirmed the predicted nonlinear and anisotropic behaviour of the tissue is due to its histological architecture.

Due to the limited availability of human samples, researchers often make use of porcine and ovine material data to approximate human tissue response. In an effort to study the differences between the material properties of aged human and porcine aortic sinuses, Martin et al. [37] performed planar biaxial tests on ten samples from the aortic roots of each species and reported major mechanical property differences between the two tissues. In a subsequent study [35], similar experiments were conducted on ovine, porcine and aged human aortic leaflets and the results showed significant histological and mechanical property differences between the three species. These differences raise many questions regarding the validity of studies that approximate the behaviour of an aged human valve tissue with that of porcine or ovine.

To date, several finite strain theory based phenomenological, isotropic and anisotropic, constitutive material models have been proposed for soft tissue and arterial wall [38-41]. Some of these models have been further developed, modified and successfully implemented for a particular type of tissue. Since then, they have been adapted by a large number of researchers experimenting with that particular type tissue. Fung et al. [38] developed a general two-dimensional strain-based orthotropic model for arterial walls to approximate its mechanical response when subjected to internal pressure and longitudinal stretching. It remains one of the most versatile and widely used constitutive models that capture the response of many types of tissues, including aortic sinuses and leaflets, with reasonable accuracy.

Another well-known model, developed for the arterial wall by Holzapfel et al. [39], is an invariant based hyperelastic model that allows for up to three families of fibre directions with arbitrary angles between them. This model was later improved by Gasser et al. [42] to account for the dispersion of the collagen fibres that is shown to significantly affect the response of the tissue. It therefore provides more modelling freedom and allows for somewhat better representation of anisotropic behaviour of the tissue, especially when the tissue's histological structure is altered by a disease affecting the collagen fibre orientation.

Isotropic hyperelastic material models are more often utilized for the aortic root finite element models than anisotropic models. This is either done to simplify the FE model and avoid the complexity associated with the anisotropic models, or due to a suggestion by some of researchers that fixation of tissue affects its histology and alters its response to behave more isotropically [43, 44]. Mooney-Rivlin [45, 46], Ogden [40] and Yeoh [41] are some of the more used isotropic constitutive models, specifically adapted for the aortic root's tissues.

Morganti [47] developed a FEA model in Abaqus and separately implemented isotropic and anisotropic hyperelastic material models for a set of bioprosthetic valve leaflets made of bovine pericardium tissue to analyse the difference between the stress distribution and valve structural behaviour (see Figure 1.6). The anisotropic hyperelastic material model presented by Holzapfel et al. and a simple hyperelastic isotropic model with a Young's modulus of 8 MPa and Poisson's ratio of 0.49 were implemented for the respective cases. From the results it was reported that the anisotropic case showed a more homogenous stress distribution and smoother valve closure along with significantly larger (more than twice) leaflets coaptation area.

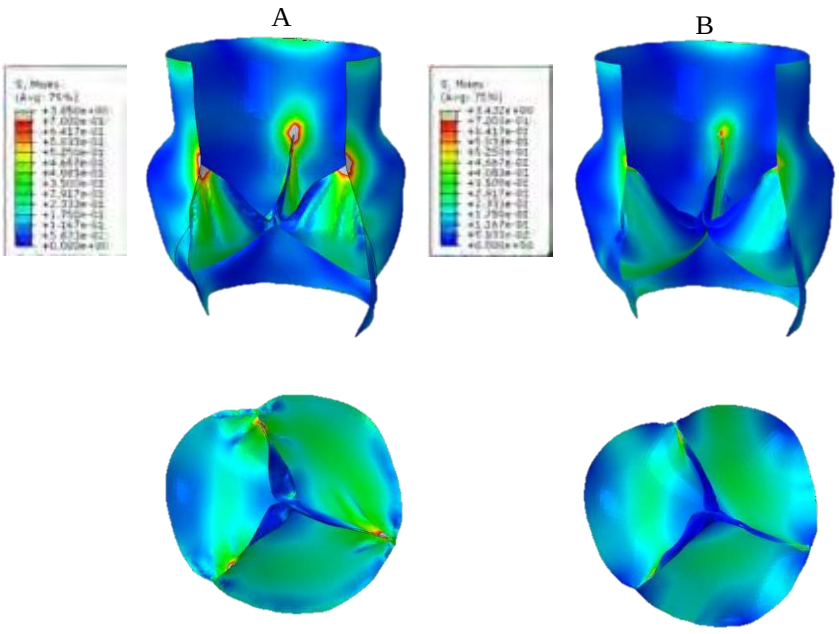

Figure 1.6 *Stress (MPa) distribution at the end of diastole for (A) isotropic and (B) anisotropic material models (from [47]).*

1.4.3 Some of the existing studies on patient-specific finite element analyses of the TAVI procedure

Finite element analysis of patient-specific TAVI was conducted by Morganti et al. [48] to model the biomechanical interaction of an Edwards SAPIEN XT valve deployed in the aortic root of two different severely symptomatic aortic stenosis cases (see Figure 1.7). The patients were injected with iodinated contrast agent to obtain contrast-enhanced CT images, which were used to extract the patient-specific aortic root and calcific component's three-dimensional models. Leaflets were later separately drawn and added to each root, taking into account their unique morphologic structure. The calcific components were then added to the sections of the leaflets that were observed to have the lesions in the images. An isotropic hyperplastic material model, based on the work by Yeoh [41], was implemented for the native root and leaflets. The calcifications were characterized by a density of 2000 kg/m^3, elastic modulus of 10 MPa and Poisson ratio of 0.3. A von Mises plasticity model with isotropic hardening was implemented for the cobalt-chromium alloy stent, along with an isotropic elastic model for the biological leaflets that were made of bovine pericardium. Two cylindrical surfaces, with displacement boundary conditions, were used to crimp and expand (deploy) the stent. The prosthetic leaflets were not included in the crimping and expanding steps and were later mapped into the deployed stent. The simulations were performed using Abaqus/Explicit and the results were compared with the actual surgical results.

Regions of high stress along with anatomical conformation of the aortic roots and the stent were observed in both patients. The eccentric shapes of the deployed stents are seen to

directly affect the non-symmetrical prosthetic coaptation of the leaflets in both patients. The isotropic material model of the prosthetic leaflets could also be one of the contributing factors to their non-symmetrical coaptation, which has been observed previously by Auricchio et al. [49]. The resulting mild prosthetic's leaflets leakage predicted by FEA was also observed in the post-operative follow-up evaluations of both patients. The FEA and the surgical results were observed to be in good agreement.

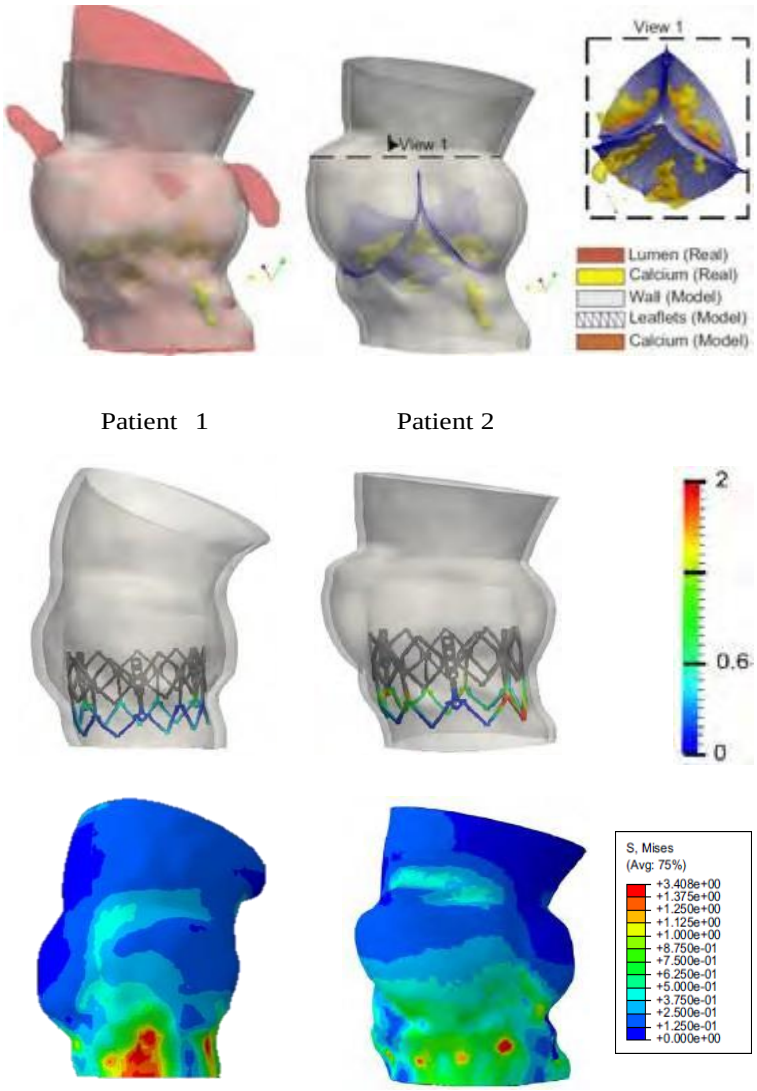

Figure 1.7 *The extracted 3D patient-specific aortic root and calcific components of one of the patients and the created leaflets model (top). The final shape of the deployed stent, showing the point-wise distance contours of the crown of the stent from the aortic wall (middle). Stress (MPa) distribution in the aortic roots of the two patients as a result of stent implantation (from [48]).*

Similar work was conducted by Wang et al. [31] using a model of the same prosthetic valve, without the inclusion of the prosthetic leaflets. The finite element model of an aortic root

and left ventricle of a patient was extracted from MSCT images, and a similar approach to Morganti et al. was taken with regard to the addition of the native leaflets to the root (see Figure 1.8). The section of myocardium that surrounds the annulus of the root is also included in the FEA model to investigate its effect on biomechanical interaction of the stent with the root. The effect of rapid ventricular pacing on the aortic root was also included in the model as a ten percent reduction in the annulus diameter due to a resulting pressure reduction (from 21 to 19 mm). The material model developed by Holzapfel and Gasser et al. [39, 42] was implemented for the sinus, leaflets and myocardium, incorporating two families of fibre directions, using tissue specific material parameters. The local calcium deposits were modelled with the properties of hydroxyapatite, using a Young's modulus and a Poisson's ratio of 60 GPa and 0.3 respectively.

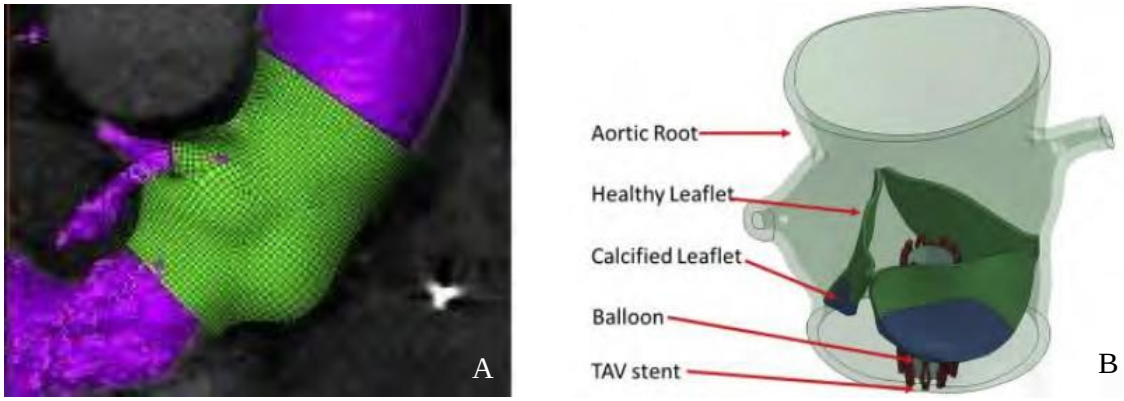

Figure 1.8 *Image segmentation and the aortic root model extraction (A). Assembly of the aortic root and leaflets, with inclusion of the calcifications (B). The catheter and stent are positioned concentrically with the annulus and are ready for deployment simulation (from [31]).*

Two different simulations were carried out in Abaqus to investigate the individual effects of inclusion of annulus diameter reduction as a result of induced RVP, and the combined effects of RVP and addition of the myocardium section surrounding the annulus. The results were then compared to a third simulation that did not include any of the mentioned effects in the first two simulations. In these simulations, the stent was expanded by applying a controlled displacement boundary condition to a catheter positioned inside the stent to act like a balloon. It is reported that the contact forces between the stent and the aortic root and the resulting stress distributions were considerably lower in the third simulation in comparison to the other two. With regard to the first two simulations, it was also observed that with inclusion of the myocardium section, the contact forces were slightly higher than the case with only RVP condition.

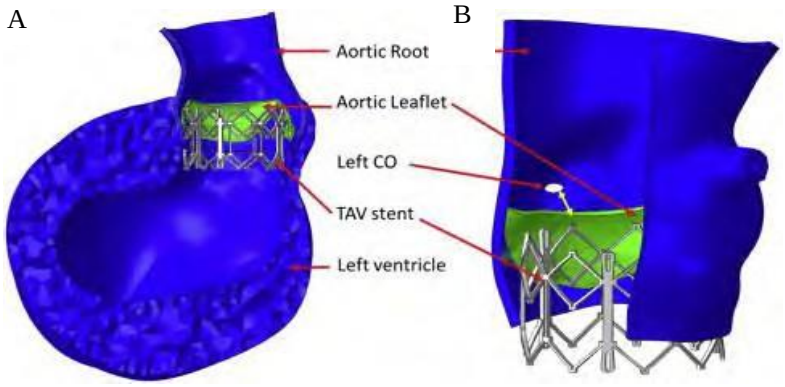

Figure 1.9 *Cut-away views of the deployed stent in native valve and root with inclusion of the surrounding myocardium section (A), and without the myocardium section (B) (from [31]).*

Auricchio et al. [49] performed their simulation using a different model of the Edwards SAPIEN valve. They extracted the aortic root model from computer tomography-angiography images without the inclusion of the native leaflets (see Figure 1.10). The material model proposed by Holzapfel et al. [39], with two families of fibres, was adopted for the aortic root in this study. The Abaqus/Explicit solver was used for performing the simulation. The stent was crimped without the prosthetic leaflets, using a cylindrical surface to mimic the action of a crimper. The deployment of the stent was, however, done by applying pressure boundary condition to inflate the created balloon model, positioned concentrically within the stent, to mimic the actual expansion process. The leaflets were later mapped onto the expanded stent and their closure in the diastolic phase was simulated by gradually applying a pressure to their inner surface. The prosthetic valve was deployed in two different positions, proximal and distal to coronary Ostia, to study its performance and the resulting stress distributions on the root. The stress distribution in the root was observed to be 22.4% higher when the stent was deployed in the distal position. No significant difference is reported for the stent's stress distribution between both positions.

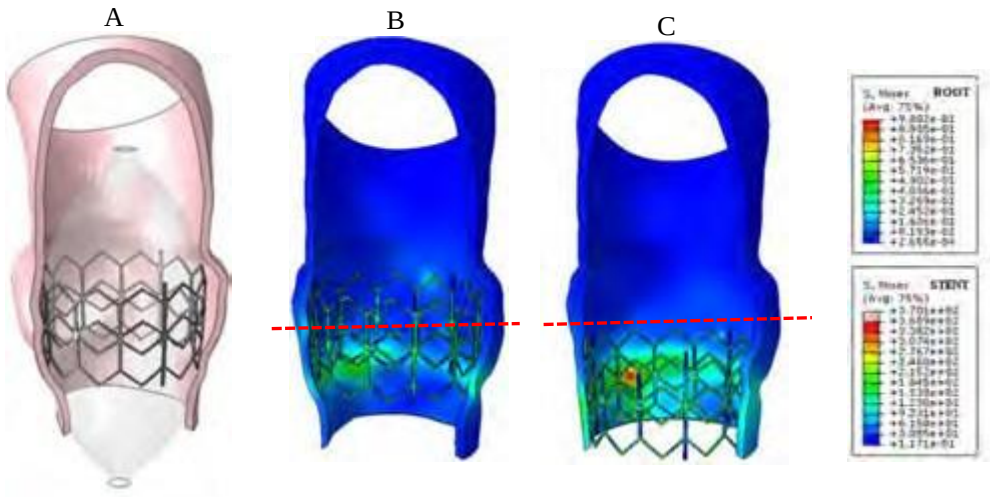

Figure 1.10 *Sectional views of the patient's root at the end of the expansion process, showing the stent and the balloon (A), stress distribution in the root as result of the stent implantation in the proximal (B), and distal (C) positions (from [49])*

The study by Capelli et al. [50] focused on five patients, of whom four were diagnosed with severe aortic stenosis and one with aortic valve incompetence. The four patients were deemed fit for open heart aortic valve replacement and prosthetic valves were surgically implanted in them. However, these valves had failed due to prosthetic leaflets stenosis and these patients were now being considered for TAVI intervention. The aortic root models of all the patients were extracted from post-operative CT images and their FE model was created in Abaqus. The individual shape of the previously implanted valves was observed in the CT images and their FE model was created and positioned in the respective patient's aortic FE models. An FE model of the Edwards Sapien stent was used for all the patients and its deployment was done using a balloon model. The Mooney-Rivlin [45,46] isotropic hyperelastic constitutive material model was adopted for the roots and native leaflets of the patients, and the Abaqus/Explicit solver was used for the analysis. For the first four patients, the stent was deployed in the existing prosthetic valve and had minimal interaction with the native root. For the fifth patient, however, the stent was deployed in three different positions and the results were analysed (see Figure 1.11). The stent's radial recoil was measured after deployment for all the patients, with the average being 13.1%. For the fifth patient, the highest radial recoil was measured to be 20.2% when the stent was deployed at the distal position from the median line (Ep model) of the native valve. The maximum principal stress distribution for the root and native leaflets were also measured at this point. For the stent, the highest von Mises stress was measured at its strut junctions for all cases. For the first four patients, the distance of the deployed stent was measured from the coronary ostia and no occlusions were reported.

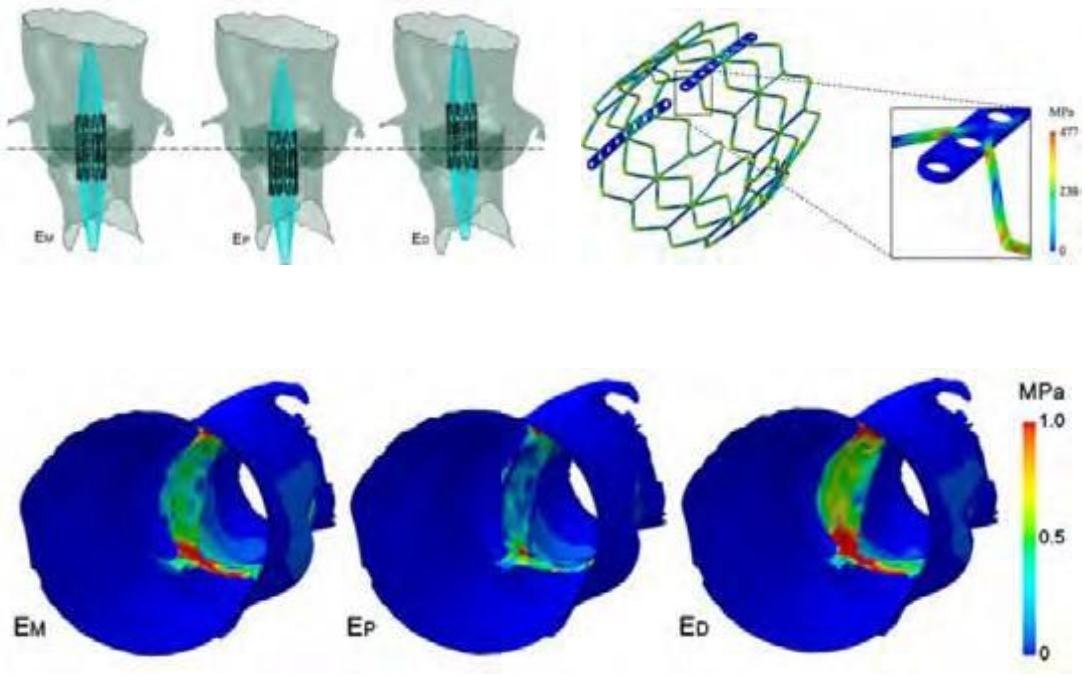

Figure 1.11 *The three positions in which the stent was deployed in the fifth patient (top left). Stress contours in the stent for the distal "Ep" position (top right), principal stress distribution in the native root and leaflets of the fifth patient (bottom) (from [50]).*

1.5 Aims of the thesis

The aim of this research is to develop two efficient patient-specific finite element simulations of Transcatheter Aortic Valve Implantation procedure using a model of the 23 mm percutaneous prosthetic aortic valve developed by Strait Access Technologies (SAT), for the purpose of its mechanical assessment and post-operative performance.

MSCT images of the chest area of two patients, in DICOM (Digital Imaging and Communications in Medicine) format, were provided by SAT, from which the 3D models of the aortic roots were to be extracted. These models were to be imported separately into Abaqus v6.13 (Dassault Systems, SIMULIA, Providence, RI, USA) for the purpose of finite element model generation, material assignment and simulation.

One-third cyclic symmetric section of the stent, and a computer model of the prosthetic leaflet along with its material property data were also provided by SAT. The balloon used for deploying the stent is to be simplified as a catheter to reduce the complexity of the model.

The FE model developed in this research project will serve as a platform for further realistic simulation of TAVI procedure, using the SAT developed percutaneous valves, and a framework for performance assessment of future valve design. The model will also be part of

the basis for the Computational Fluid Mechanics (CFD) models needed for the ISO requirements to assess the flow fields in the vicinity of the valve.

1.6 Structure of the thesis

In Chapter 2, the anatomy, histology, physiology and the relevant pathology of the aortic root and valve is presented, and the biomechanics of their tissues is briefly discussed. Further, the decisions made with regard to the chosen material model for each tissue are outlined, and the process of extraction of the three-dimensional patient-specific aortic roots is explained. In Chapter 3, the process of generating the required finite element models of the stent and the prosthetic valve is outlined and the details of the material models implemented for each part is explained. Further, the created models of the crimper and the balloon used for crimping and deployment of the stent are presented. Finally, the analysis procedure chosen for performing the simulations is described, and the results of the mesh sensitivity studies conducted in order to choose the most appropriate mesh for the stent and the prosthetic leaflets, are presented. In Chapter 4, the process of further improving the geometries of the patient-specific roots and their finite element model generation and material models implementation is described. Further, the process of creation of the patient-specific valve leaflets is also described and the result of the mesh sensitivity study conducted for the roots and leaflets is presented. Thereafter, the steps taken for the creation of the analysis models for the TAVI simulations for each patient are outlined. In Chapter 5, the results of the simulations are presented, and the mechanical interaction of the stent with the patient-specific anatomies is analysed. Finally, conclusions of the work are presented along with final remarks and recommendations in Chapter 6.

Chapter 2

The Aortic Root and Valve

This chapter presents a description of the relevant anatomical and histological features of the human aortic root and valve, and briefly outlines the effects of tissue alterations, due to relevant pathological processes, on the mechanical response of their tissues. Thereafter, the physiology of the aortic valve is also briefly discussed, with special focus on its biomechanics and characterization of its tissue property. Finally, the processes followed for extracting the patient-specific three-dimensional models of the aortic roots of the two patients who were diagnosed with aortic stenosis is described.

2.1 Anatomy and physiology of the aortic root and leaflets

The aortic root is defined as the section of the aorta that connects the left ventricle to the ascending aorta. Its function is to allow for unidirectional flow of blood from the left ventricle to ascending aorta, and in turn to the rest of the body. It consists of the Sinuses of Valsalva and three leaflets that are referred to as the aortic valve.

The anatomic features of the root are [4, 51, 52]:

- the commissures
- the interleaflet triangles
- the sinotubular junction
- the anatomic ventriculo-aortic junction
- the virtual basal ring (also known as the annulus)

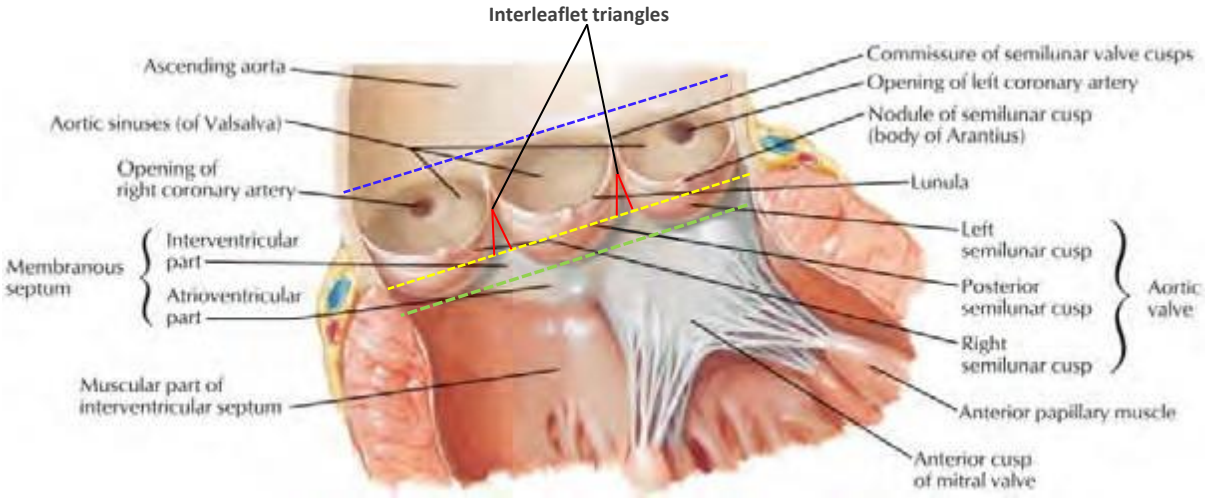

Figure 2.1 *Detailed anatomy of the aortic root (adopted from [4] with reference to figure 2.3 (right))*

The leaflets are semilunar in shape, flexible and structurally thinner than the sinuses. Three pronounced features of a leaflet are [4]:

- the belly – the central section of the leaflets, from the attachment points to the Lunula.
- the Lunula – the slightly thicker band that is located towards the top of the leaflet.
- the nodule of Arantius – the sectional thickening of the leaflet's tunica intima layer in the middle-upper region of the Lunula [53].

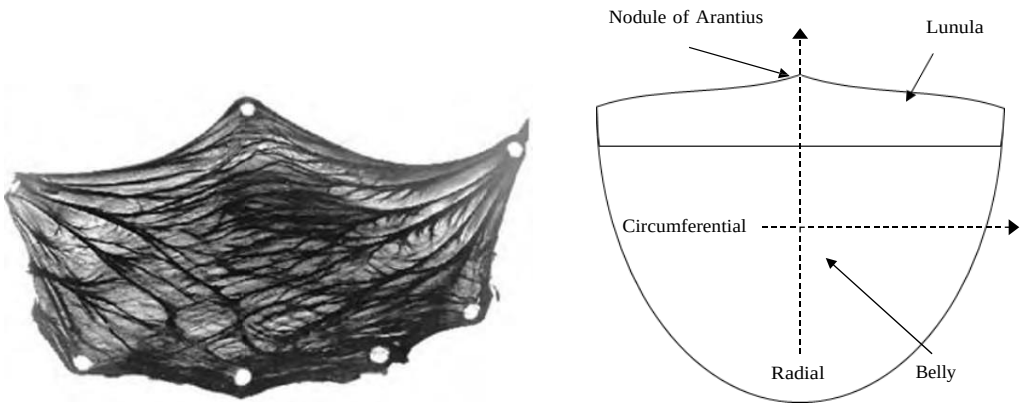

Figure 2.2 *A photograph of an excised leaflet of an aortic valve that shows its general fibre architecture (left) (from [54]). A schematic drawing of a leaflet outlining its features, and presenting the generally accepted directional convention (right).*

A healthy leaflet has variable thickness along its geometry and on average is less than one millimetre thick [55]. Its thickest section is located on the upper central region and near the nodule of Arantius.

The Sinuses of Valsalva are the three distinct dilations on the root that support the leaflets and are named according to their inclusion of the coronary ostia (Figure 2.3 (left)). The right, left and non-coronary sinuses extend from the sinotubular junction to the anatomic ventriculo-aortic junction, whilst the leaflets extent slightly further to the virtual basal ring, which is the nadir point of the semilunar attachments of the leaflets, and is usually referred to as the annulus [51,52]. The triangularly shaped spaces in between the neighbouring leaflets, with their sides and base being the semilunar attachments of the leaflets and the virtual basal ring respectively, are known as the interleaflet triangles.

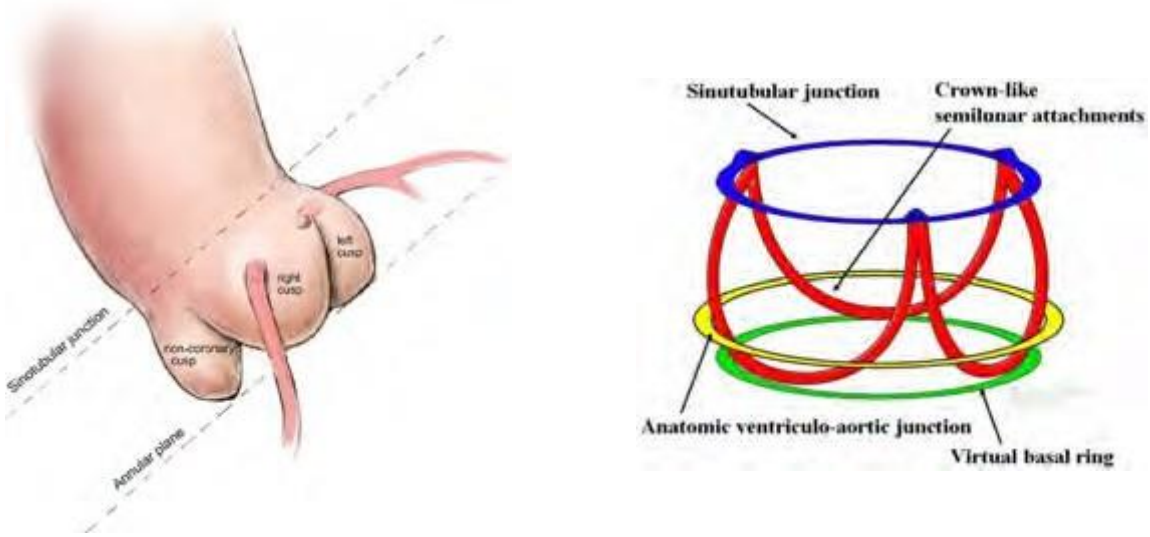

Figure 2.3 *Exterior view of the aortic root, indicating the position of the coronary ostia on the sinuses (left) (from [56]), and the outlined features of the aortic root and the conventional naming adapted in this text (right) (from [52]) - in reference to Figure 2.1.*

The sinotubular junction, which is nearly circular, is defined as the ring outlined by connecting the upper most peripheral attachment points of the leaflets to the sinuses and is the border line between the aortic root and the ascending aorta [51, 52]. Starting from this border, the commissures are the small parallel running sections of two neighbouring leaflets. The ventriculo-aortic junction is a ring-like border between the muscular ventricle structure and the fibro-elastic wall of the aortic sinuses [52].

The aortic valve functions passively and opens during the systolic phase of the cardiac cycle as a result of blood being forced to push open the leaflets on its way to the ascending aorta. The ventricular pressure reduces after reaching its peak, at about 120 mmHg, and in turn causes the aortic pressure to reduce which results in closure of the valve at just below 100

mmHg [52]. All structures proximal to the leaflets-sinuses semilunar attachment lines are subjected to the ventricular pressure changes, whilst the distal sections are subjected to aortic pressure changes [52]. The upper portion of the root expands during the systolic phase to facilitate the retraction and opening of the leaflets. The lower part of the root however expands during the initial stages of the systolic phase, and contract when the ventricular pressure is at its peak in order to reduce the traveling distance required for leaflets coaptation [51].

The sinuses play two crucial roles in the general physiology of the aortic root. Firstly, they provide an adequate amount of space behind the leaflets so that they do not occlude the coronary ostia when fully opened. Secondly they allow for the development of eddy currents in these spaces that hold off the leaflets at an optimal point, so that they can easily be caught by the reversely flowing bloodstream and coapt at the end of the systolic phase [51].

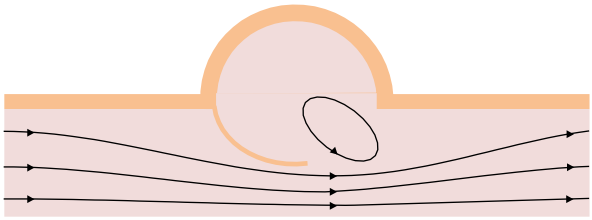

Figure 2.4 *Two-dimensional schematic drawing of the aortic root flow pattern (adapted from [57])*

The average resting heart rate of an adult is between 60 to 80 beats per minute (bpm) [58], which is an indication of the amount of complex cyclic dilation/contraction that the aortic root goes through every second. It is therefore essential to have a good understanding of the histology of the aortic root and valve tissues to be able to develop a reliable computational model that can correctly estimate its biomechanical behaviour.

2.2 Histology of the aortic root and valve tissues

2.2.1 Histology of the aortic valve's leaflets

The aortic valve leaflets are mainly made up of three layers that are named according to their anatomic location, cellular composition, extracellular matrix and biomechanical properties [55].

These layers are:

- Fibrosa
- Spongiosa
- Ventricularis

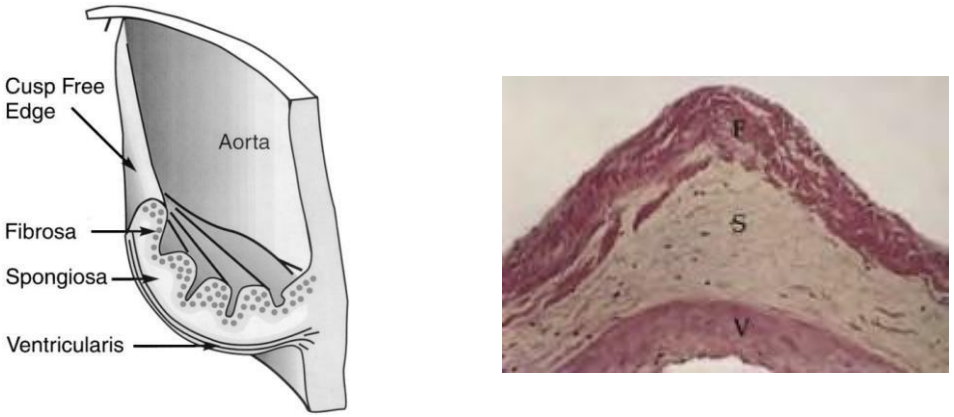

Figure 2.5 *A schematic sectional view of the aortic valve leaflet showing its layered configuration of Fibrosa, Spongiosa and Ventricularis [59] (Note the folded, stacking configuration of the collagen fibres in the Fibrosa at the central region of the leaflet) (left). Sectional microscopic image of an aortic valve leaflet, outlining its three layers [60](right).*

The cellular architecture of the leaflets is mainly made up of valvular interstitial cells (VIC), smooth muscle cells and myofibroblasts that are enclosed by a layer of valvular endothelial cells (VEC) [55] (Figure 2.6). The fibrosa, which is the main load-bearing layer, contains type one and three fibrillar collagens that have folded configuration at the leaflets central region and unfold when the leaflet is radially stretched [55]. These are mainly oriented circumferentially, hence making the fibrosa stiffer in this direction. The ventricularis consists of a radially aligned matrix of elastin that adds more compliance to the leaflets. The glycosaminoglycans (GAG) in the spongiosa layer facilitate the rearrangements of the fibres in the ventricularis and fibrosa during the considerably high deformations.

Leaflets, by dry weight, contain approximately 50% collagen and 13% elastin [61]. Although this might suggest that elastin's contribution to the leaflets biomechanics is minimal relative to collagen, it is believed that elastin is responsible for the considerable part of the leaflets ability to extend beyond 50% strain and successful recoil - in addition to the collagen realignment and straightening action before full engagement- during the diastolic phase of the cardiac cycle [59].

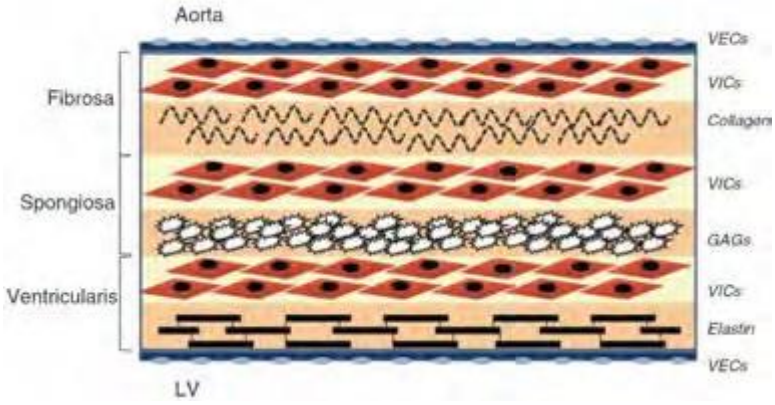

Figure 2.6 *Cellular architecture of the aortic valve leaflts [55].*

Studies conducted to investigate the influence of collagen fibres on the biomechanics of leaflet tissue have reported that for the duration of the high strain stage, these fibres help to efficiently reduce the critical stress in the sensitive parts of the leaflets and stabilize their motion, in both systolic [62] and diastolic [63, 64] phase of the cardiac cycle.

2.2.2 Histology of the aortic sinuses

Histologically, the aortic sinuses have layered structure similar to those of large arteries and are made up of three layers:

- Intima
- Media
- Adventitia

A schematic of the idealized architecture of the layers is shown in Figure 2.7. The Intima (I), which is the thinnest and innermost layer, mainly consists of a single sheet of endothelial cells followed by a membrane base and sub-endothelial layer of collagen fibrils. The Media (M) is separated by elastic laminae in to a number of fibre-reinforced transversely isotropic sub-layers consisting of elastic and collagen fibrils along with smooth muscle cells. The Adventitia (A), which is the outermost layer, is mainly composed of thick bundles of collagen fibrils that are helically arranged [65].

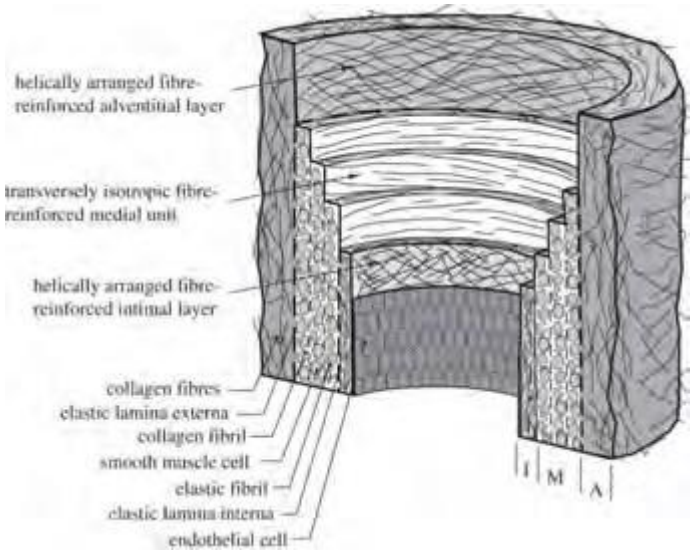

Figure 2.7 *Idealized histological architecture of a healthy human artery, outlining its layered structure (from [42,65]).*

2.3 Biomechanics of the aortic root and valve and characterization of their tissue properties

The aortic root is a dynamic structure that experiences continuous and complex mechanical loading patterns during the cardiac cycle that can initiate permanent tissue scarring and degradation. Figure 2.8 shows a schematic of a normal aortic root during the systolic and diastolic phase of the cardiac cycle, and outlines the types of forces experienced by the leaflets. It also shows the histological layers of the tissue, and how their constituents react in response to the induced forces.

In normal physiological conditions, the leaflets are subjected to an orthogonally acting transvalvular pressure of between 80 to 120 mmHg, with Fibrosa being the main supporting structural layer [34]. Thubrikar [66] who made use of marker-fluoroscopy with radiopaque markers positioned on canine aortic leaflets, assuming cylindrical geometry of the aortic root, measured a membrane circumferential stress of 0.167 and 2.4 kPa during systole and diastole. Somewhat similar results has been reported by other researchers utilizing finite element models with the major sources of discrepancy being the simplistic assumptions and approximations made for the tissue material behaviour and the root geometry. In one of the earlier FE models developed by Cataloglu et al. [67], based on a human aortic leaflet thickness of 0.6 mm and a pressure of 144.7 mmHg, the maximum principal stress was reported to be 2.19 kPa, which is comparable to the experimental results from Thubrikar's study.

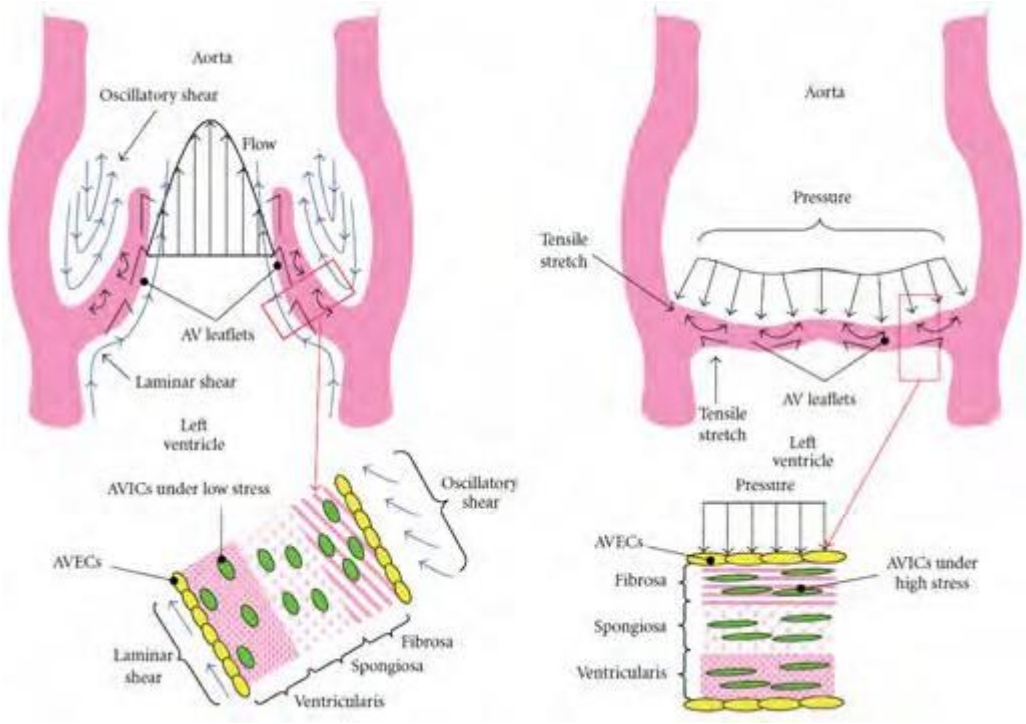

Figure 2.8 *Two-dimensional schematic drawing that outlines the mechanical forces experience by the aortic valve leaflets during systole (left) and diastole (right), from both structural and histological points of view (from [34]).*

High regional shear and bending stresses experienced by the leaflets, which can cause tissue degradation, is of major physiological and pathological importance. If the tissue is already affected by a disease, such as RHD or endocarditis, these regions become even more vulnerable due to the existing lesions. During the systolic phase, the ventricular sides of the leaflets experience shear stress as a result of blood flowing past the leaflets. In the diastolic phase, the aortic side of the leaflets experiences oscillatory shear stress due to blood pooling in to the sinuses and the formation of vortices. These vortices are, however, proven to reduce bending stress on the leaflets and aid coronary flow [66].

The leaflets are subject to a considerable amount of bending during the cardiac cycle. When the tissue bends, the convex and concave sides of the leaflets are under tensile and compressive stress respectively. The collagen and radially aligned elastic fibres can freely bend circumferentially and do not have significant resistance in this direction. The leaflet's semilunar attachment lines, which act like a hinge to allow for their easy movement, and the leaflets belly, which experiences curvature reversals, are the two regions particularly under a considerable amount of bending stress.

Figure 2.9 (left) shows the two common patterns of degradation and calcification observed form structural examination of affected leaflet tissues. It can be seen that the coaptation band and the semilunar attachment lines (extending towards the belly region) are the most affected regions due to the highest shear and bending stress occurring in these sections.

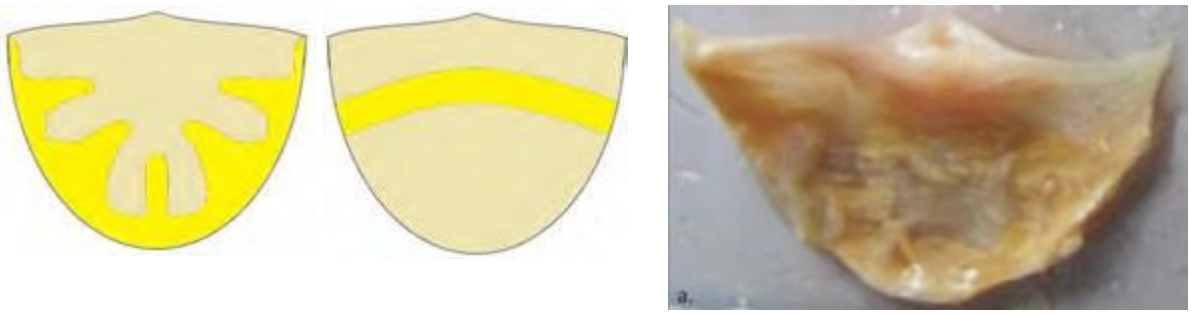

Figure 2.9 *The common patterns of age related degradation and calcification observed from structural examination of affected leaflets (left) (adapted from [68]). An excised leaflet of an aged human (right) (from [35]).*

2.4 Pathology of the aortic valve leaflets

Aortic Stenosis and regurgitation are the two major conditions that may severely disrupt the function of the aortic valve. In this section, a brief explanation of each condition will be provided.

2.4.1 Aortic stenosis

Aortic Stenosis (AS) is the medical term for the narrowing of the aortic valve due to congenital malformation or degeneration/damage of the leaflet, which is either due to deposition of calcium or ARF, that cause inflammation and thickening of the tissue. The abnormally thick or fused-together leaflets either do not close properly or obstruct the flow of blood, forcing the heart to work harder to compensate [69].

In the congenital case, the abnormalities include leaflet malformation, abnormal attachment of the leaflets to the root, and incorrect valve size formation. Bicuspid Aortic Valve Disease (BAVD) is the most common congenital aortic valve disease and it is estimated that about 2% of the population is affected by it [70]. As the name suggests, the valve consists of only two leaflets which may severely affect its function.

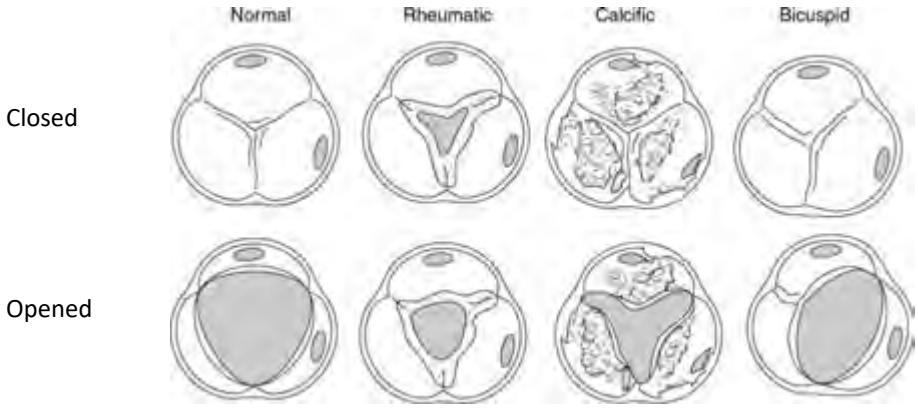

Figure 2.10 *Comparison between normal and malfunctioning aortic valve leaflets in opened and closed arrangements [71].*

Calcific aortic stenosis, on the other hand, can occur due either to age-related inflammatory degradation of the leaflet tissue, which is being subjected to continuous "wear and tear", or as a result of biochemical and humoral processes [72].

It is believed that the mechanism of calcific AS development is, in many ways, similar to atherosclerosis. In the initial stage of the process, mechanical stress causes endothelial injury which allows for the penetration and accumulation of inflammatory cells and lipids [72]. Progression beyond this stage will cause the tissue to considerably thicken and the inflammation process to continue, with bone lamellar and calcific lesion formation in the fibrosa that extends to the surface on the leaflet on the aortic side. This process ultimately stiffens the leaflets up to an extent that they are not able to flex adequately and will lose their compliance. This in turn hampers the valves functionality by causing blood flow blockage that can be fatal if not treated. A histological sectional view of this process is presented in Figure 2.11 (right), showing the significant structural change that caused considerable thickening of the leaflets.

Rheumatic AS is identified by a triangular orifice formation due to commissural fusion, calcification and thickening of the leaflets. The inflammation, scarring and degeneration mainly occurs on the edges of the leaflets and is due to the reaction of the body's immune system to the infection caused by the group A streptococci bacteria. Rheumatic fever almost always affects the mitral valve first. Therefore, rheumatic aortic valve disease is usually occurs in conjunction with rheumatic mitral valve disease.

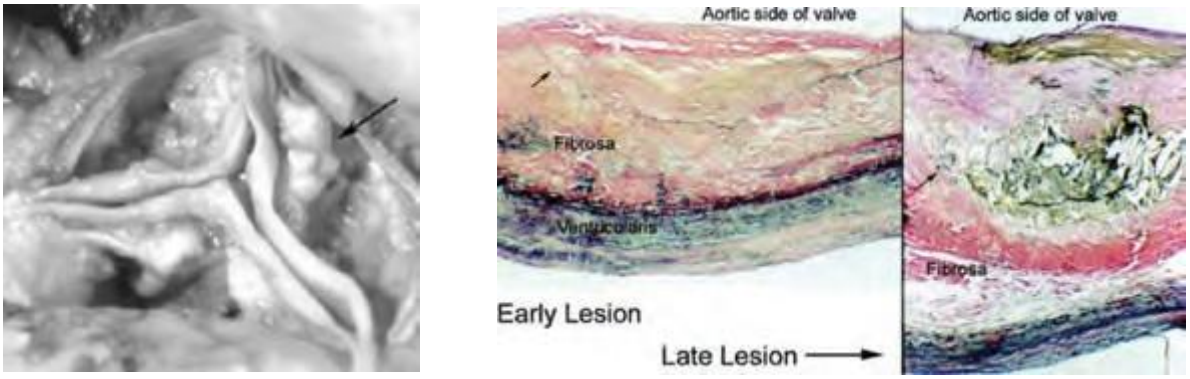

Figure 2.11 *A photograph of a calcified aortic valve leaflets (left), and histological sectional view of a leaflet affected by calcification that shows its histological alteration (right) (from [55]).*

2.4.2 Aortic regurgitation

Aortic regurgitation AR is the condition in which the aortic valve leaflets cannot effectively stop the backflow of blood in to the left ventricle at the end of the systolic phase. In addition to the factors that cause AS, infective endocarditis and disease that affect the aortic root and annulus -such as the idiopathic aortic root dilation- are also the reasons behind AR.

2.4.3 Diagnoses of aortic valve disease

For the past three decades, major advancements have been made in understanding and diagnostics of aortic valve disease. The diagnosis is made by running a few tests that help the cardiologist to evaluate the type and severity of the disease. Echocardiography is the key non-invasive imaging technique used in this regard [71]. It utilises ultrasound waves to generate real-time 2D or 3D dynamic images of the heart that allow the cardiologist to observe, listen and make the necessary measurements to be able to assess and make the correct diagnoses.

2.5 Characterization of the aortic root and valve biomechanical tissue property

Uniaxial and biaxial testing is performed on specimens taken from human and animal aortic root tissues in order to characterize and compare their mechanical behaviour. The aortic root's tissues are known to be inhomogeneous, viscoelastic, anisotropic and nonlinear [33]. However, in an effort to simplify and allow for reproducibility of the experimental results, an appropriate preconditioning cyclic loading regime is adopted to reduce tissue hysteresis and

stabilize its mechanical response. In these experiments, the common assumption is that the tissue is homogeneous and incompressible.

Figure 2.12 shows two samples of stress-strain plots from two different studies performed on aged human leaflets, with the presence of calcific deposits, and sinuses. These plots allow for graphical representation and quantification of the nonlinear and anisotropic behaviour of the tissues in their respective two dimensional axes (circumferential/radial for the leaflets and circumferential/longitudinal for the sinuses).

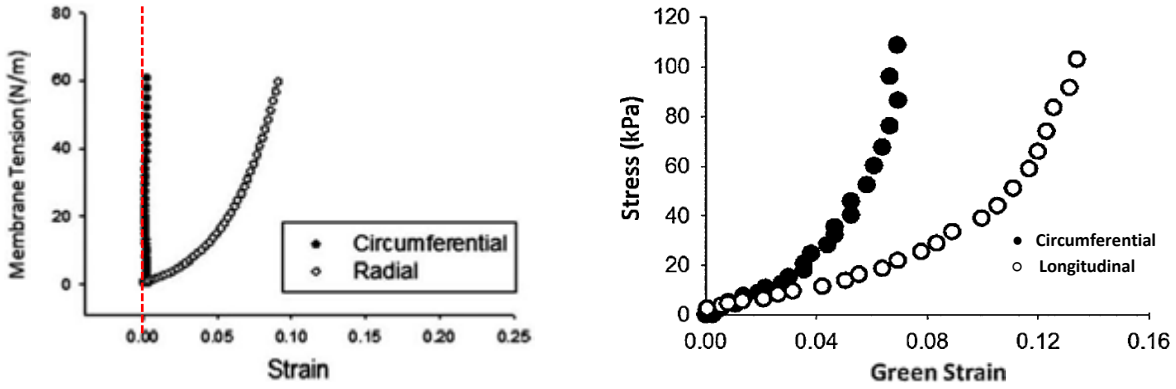

Figure 2.12 *Equibiaxial experimental stress-strain data of aged human specimens: the aortic valve leaflets (left) (from [35]) and sinuses (right) (from [37]).*

For the purpose of better understanding the tissue response, each plot can be divided into three phases according to Figure 2.13. In the initial stage of loading, the tissue behaves isotropically and is much more compliant relative to the second and third stages, which is due to the straightening/realignment action of the wavy collagen fibres and the presence of elastin. It is known that the collagen fibres are stiffer than elastin and as they unfold and become straighter and more aligned with loading axis, the tissue becomes stiffer and the strain increase is considerably less than the previous stage.

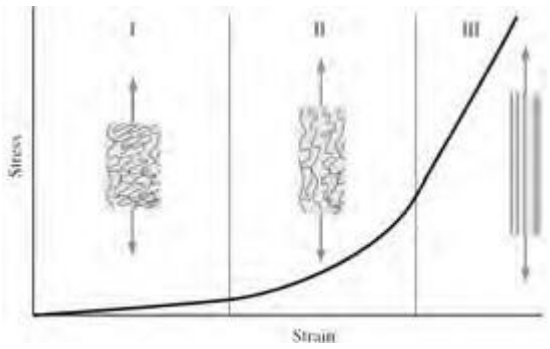

Figure 2.13 *The schematic diagram of a typical stress-strain plot, showing the suggested categorization in to three main stages according to collagen fibre morphology (from [73]).*

Although the circumferential response of the leaflets is expected to exhibit a relatively stiffer response due to the mainly circumferentially aligned collagen fibres, from the plot in Figure 2.12 (left) it can be seen that very low to no strain increase is visible in this direction, and cannot easily be divided in to the suggested three stages. This is due to the existence of calcium deposits on the leaflets that has affected the histological structure of the tissue and severely stiffened its response.

With regard to the material response of the sinuses, it has been reported that with ageing, the aortic collagen density increases and their waviness is considerably reduced [74]. These factors cause the tissue to exhibit stiffness response and become less compliant in both the longitudinal and circumferential directions.

Due to the limited availability of human samples, porcine and ovine aortic root tissue data are commonly used as an approximation for aged human data in the material models employed in computational simulations. Martin et al. [37] has recently performed biaxial tests on sample lealets of young porcine, ovine and aged human (80.6 ± 8.34) aortic leaflets, to put in perspective the differences between the tissues of these species. He has reported that, anatomically, the human and the ovine leaflets samples were the thickest and thinnest of the three, with the porcine sample being considerably thinner than the other two. From the histological point of view, the human and porcine leaflets samples had considerably more collagen fibres in comparison to ovine sample and that the Spongiosa layer in ovine sample where the thickest of the three species. Further, the human samples exhibited a considerably stiffer mechanical response in the circumferential direction than the other two samples.

A similar study [35] was carried out for the comparison of the sinus's tissue responses of aged human and young porcine tissues. Ten aged human tissues, with a mean age of 90.1 ± 6.8 years, were compared against ten 6 to 9 month old porcine tissues. It was reported that the thickness of the samples were somewhat similar, and histologically the porcine tissue contained relatively higher amount of elastin, which made it more compliant than the human sample. The elastin fibres of the human tissue were appeared to be straighter and thinner than that of the porcine sample. Further, the mechanical response of the human tissue exhibited a much stiffer mechanical response than that of the porcine and that the porcine tissue showed a somewhat "linear" response with greater compliance at low stresses.

Both of these studies conclude that there are significant differences in structural composition and mechanical response between the considered samples, and questions the validity of the studies conducted by approximating the response of aged human aortic tissues with that of porcine or ovine.

2.6 Multi-Slice Computer Tomography imaging and the aortic root three-dimensional model extraction

2.6.1 Multi-Slice Computer Tomography (MSCT)

MSCT images are obtained via a CT scanner that has an X-ray tube and rows of detectors, which rotate around the patient, capturing both volumetric data and cross-sectional images (see Figure 2.14). The various atomic densities of different tissues cause different attenuation of the X-ray fan beam passing through, with the highest attenuation occurring in tissues with the highest atomic density, hence producing grey-scaled image slices. The rotation allows for the calculation of attenuation at every single point of the slice and therefore produces a cross-sectional image of the concerned section of the patient's body. MSCT is the most recent development in the spiral computed tomography technology with the scanners being equipped with multiple thinner detector rows and allowing for faster x-ray tube rotation, hence improving the quality of the data captured and therefore improving the quality of the 3D model that is later extracted [75].

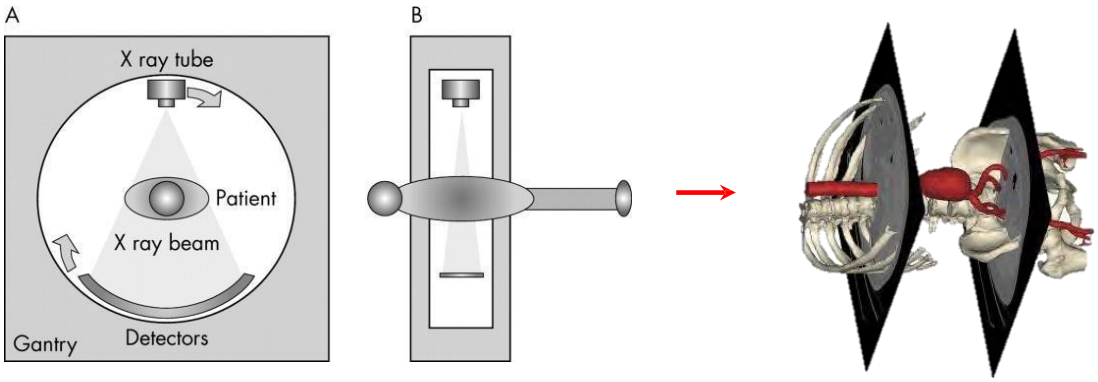

Figure 2.14 *Simplified schematic of a MSCT or MDCT scanner showing it main components (left) (from [75]) and the samples of thinly sliced images that are recorded and later processed for the purpose of 3D anatomical model extraction (right) (from [76]).*

2.6.2 Three-dimensional model extraction of the aortic root

The mid-chest area MSCT images of two patients were provided by SAT, in the DICOM (Digital Imaging and Communication in Medicine) format, for the purpose of three-dimensional aortic root model extraction[1]. The image processing software ScanIP was used for this purpose, which allows for 3D image data visualization and model generation [76].

[1] The use of these images was approved by the University of Cape Town's Ethics Committee (see Appendix A).

Hence, each patient's aortic root model was extracted by firstly cropping the aortic root's region and a small section of the left ventricle and ascending aorta from the rest of the image. Several experiments were carried out to determine the optimal grayscale threshold band that allow for the optimal segmentation of the lumen (meaning blood which appears as a luminous medium in CT images) in the aortic root and aid in clutter reduction. The segmented lumen was then extracted as a 3D model and the surrounding unwanted three-dimensional clutter, which was unavoidable during segmentation, were deleted by using a combination of 3D modification tools. The Gaussian recursive filter and several other 3D model processing tools were utilized to smoothen the raged surface of the 3D model and to further improve its shape. Although the walls of the aortic root were faint and mostly invisible, a combination of the available enhancing filters that allow for outlining some of the faint feature in the images were used to improving its visibility. Thereafter, the lumen model was duplicated and dilated until it was observed that the aortic root walls were fully covered with little to no overextension. The core lumen model was then deleted. The appearance of the aortic root model was further enhanced and compared with the CT images to ensure that it is as similar as possible to the imaged anatomy. Figure 2.15 shows the step by step evolution of this process for the first patient. The extracted roots are shown in Figure 2.16.

It should be mentioned that due to the thin structure of the aortic leaflets, their segmentation and extraction were not possible. Therefore, the native leaflets models were created in SolidWorks (Dassault Systemes, USA), based on the observation from the MSCT images, and were later attached to the roots. This process is described in Chapter 4. Each patient-specific root's short and long diameters were measured using Simpleware's 3D measuring tool and are shown in Table 2.1.

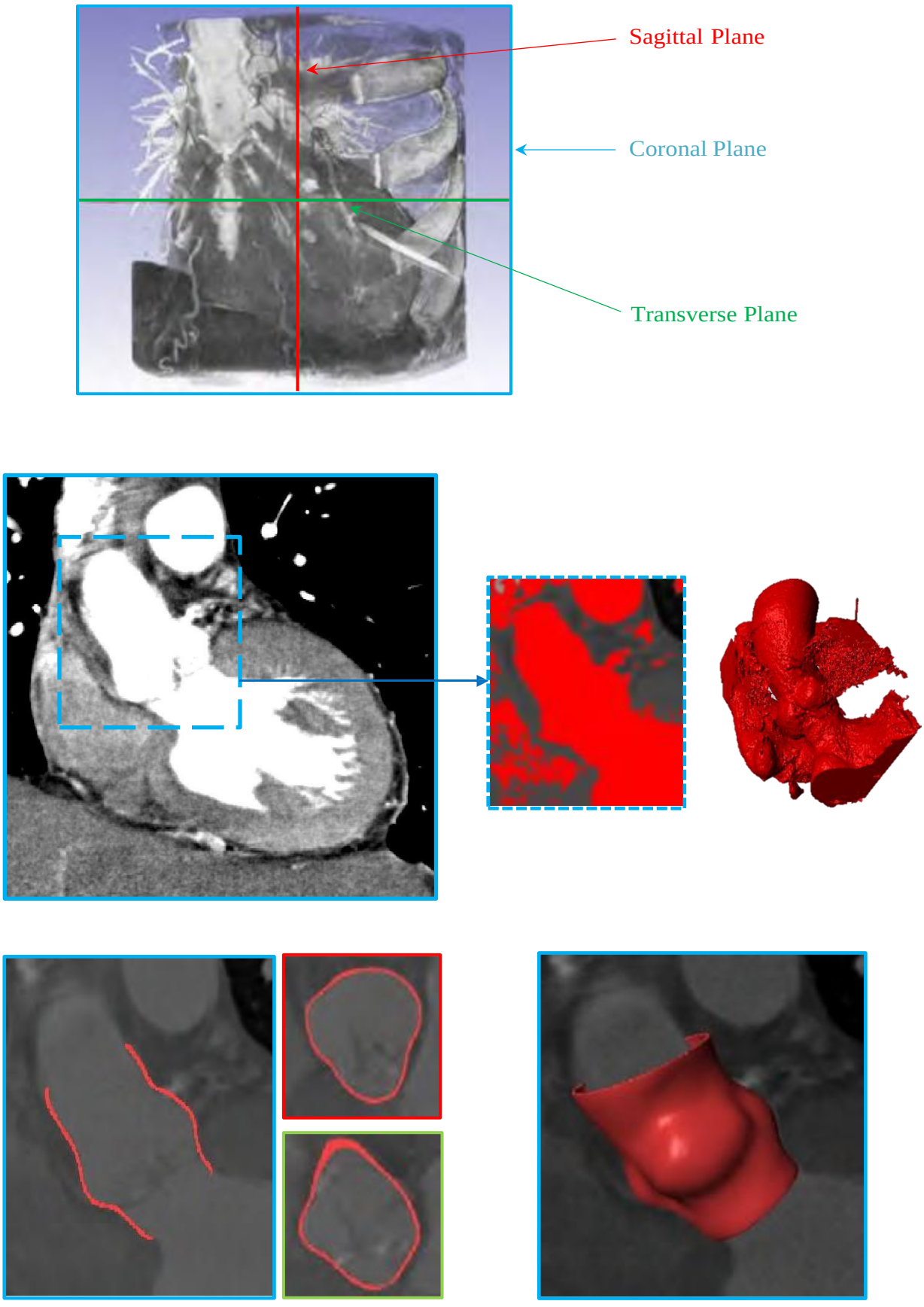

Figure 2.15 *The step by step process of extracting the first patient's aortic root. At the top, the orientation of the anatomical planes, used for visualizing and segmenting the root, are shown.*

These models were initially imported into Solidworks for further 3D processing and leaflets model creation, and then were imported to Abaqus for their FE model creation and assembly.

First patient	Second patient
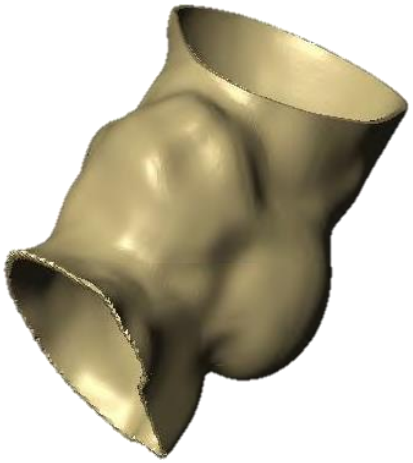	

Figure 2.16 *The extracted three-dimensional models of the first and second patient's aortic roots. For both patients the measured wall thickness was approximately 1.35 mm.*

Table 2.1 *The measured dimensions of the annulus of the patients.*

	Short axis (mm)	Long axis (mm)
First patient	19.65	22.3
Second patient	17.0	18.8

Chapter 3

Finite Element Model of the Stent and Prosthetic Valve

This chapter presents a description of the procedures followed in developing a finite element model of the 23 mm percutaneous prosthetic aortic valve, designed by Strait Access Technologies (SAT), which will be used for the patient-specific TAVI simulations in chapter 4. The flow chart below shows a summary of this process:

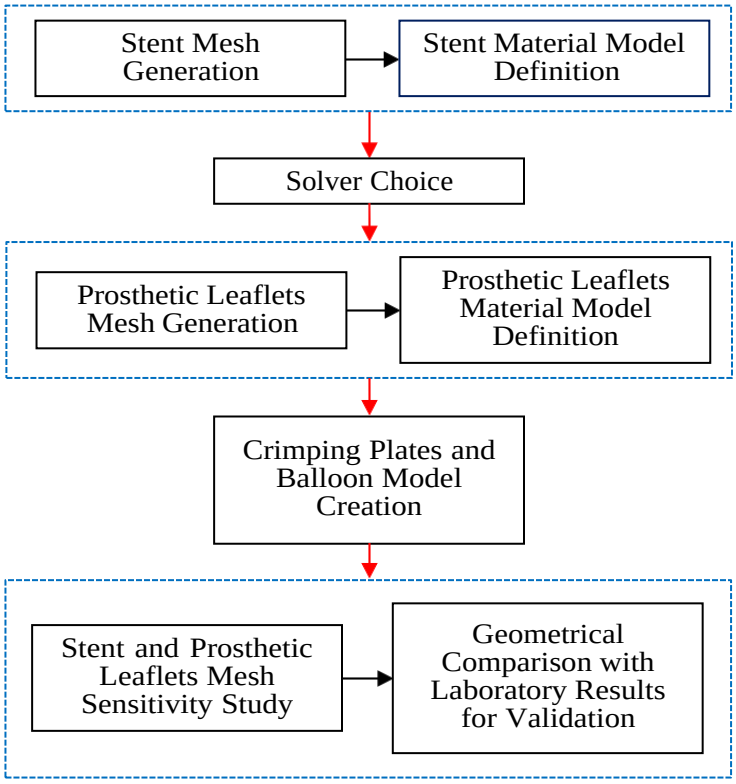

Figure 3.1 *The flow chart of the procedure followed in developing the finite element model of the stent and prosthetic valve.*

3.1 The finite element method

Many scientific and engineering physical phenomena can be described using partial differential equations (PDE), which are often of nonlinear nature. Solving these equations by analytical methods for arbitrary geometries is almost impossible [77]. The finite element method is a powerful numerical approach through which these PDEs can be solved approximately. In all applications, the purpose of the analysis is to solve for a field quantity such as displacement or temperature [77].

The basic idea of the finite element method is to divide the domain of interest into a number of subdomains or finite elements, such as quadrilaterals, triangles, tetrahedra or hexahedra (see Figure 3.2). The relevant field quantity, for example displacement for stress analysis, over an element is interpolated from its nodal values, which are the inter-elemental connection points. The solution for the entire geometry can then be obtained when the elements are connected together and the field quantity is interpolated over the entire domain in a piecewise manner. In general, the accuracy of the solution improves with an increase in the number of elements (and hence nodes); however, this increases the computation time and hence results in an increase in the cost of the analysis [77].

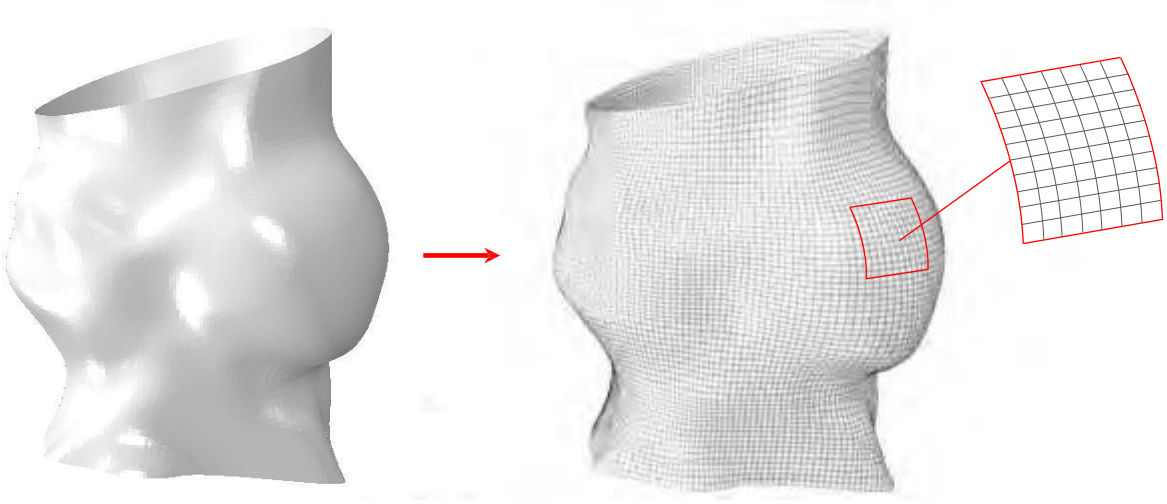

Figure 3.2 *An example of a complex geometry (patient-specific aortic root) which is discretized using quadrilateral shell elements.*

In the context of TAVI, finite element simulations can be used to study the following topics:

- stress distribution in the stent as a result of large deformations due to crimping, deployment, and interaction with the aortic root and leaflets;
- the percentage of radial recoiling and axial extension/foreshortening of the stent after crimping and deployment;

- stress development in the aortic roots and leaflets for predicting potential tissue damage; and
- the possibility of coronary ostia obstruction by the prosthetic valve and/or the defective native leaflets;

3.2 Finite element model of the stent

3.2.1 Element selection and considerations

Depending on the geometry of the stent, occasionally these are modelled using beam or shell elements. However, hexahedral elements are more frequently used [31,48-50,78] to capture the local peak stress and strain. This is due to their ability to provide a good balance between accuracy and computational efficiency. As stents are mainly loaded in bending, the linear fully integrated hexahedral element is not suitable for this type of application due to its tendency to become overly stiff in such loading applications, a condition commonly known as "shear locking". This phenomenon occurs due to the sides of the element not being able to bend to curve when it is subjected to bending, and as a result, conforming to an auxiliary shape shown in Figure 3.3 (right). This in turn results in development of tensile and compressive stresses in the upper and lower surfaces of the elements respectively, which is visible from lengthening and shortening of these faces. Looking at the plotted lines going through the integration point, it can be seen that their orthogonality is lost in the auxiliary shape, which indicates the existence of shear stress σ_{12} at these points. Theoretically this is not correct due to the assumption that in a section of a material that is subjected to pure bending, the shear stress is zero. The consequence of this phenomenon is that the parasitic shear absorbs strain energy that results in smaller bending displacement, stiffer reaction and spurious stresses [79,80].

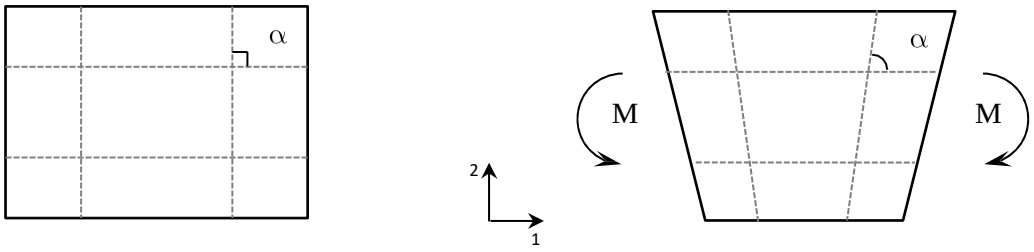

Figure 3.3 *A 2D view of a fully integrated linear hexahedral element (left) that is deformed (right) by being subjected to pure bending (adapted from [79]).*

The shear locking problem is alleviated with the incompatible mode and reduced-integration linear hexahedral elements. The incompatible mode element's displacement field is

augmented internally with additional displacement modes, which improve their behaviour when subjected to bending by eliminating the parasitic shear stresses that cause the artificial stiffness in fully integrated element. However, this element is computationally more expensive than the reduced-integration elements due to the added extra modes and its usage of full integration [80].

With regard to reduced-integration elements, locking is mitigated by the uniformly reduced integration scheme it utilizes, therefore making it computationally more efficient due to only having a single central integration point. A major disadvantage of this element is that it can result in a mesh instability phenomenon commonly known as "hourglassing". This phenomenon occurs due to the presence of spurious zero energy modes that interfere with the true response of the element and can severely affect the solution accuracy. Figure 3.4 shows a 2D schematic drawing of a linear hexahedral reduced-integration element and its inability to detect strain at its integration point due to the hourglassing effect. In order to avoid any potential problem, at least four elements should be used through the thickness of the structure along with appropriate hourglass controls. With this approach, each element detects either tensile or compressive axial strain, not both, and hence the problem is alleviated. To make sure that hourglass controls do not significantly alter the solution, the Artificial Energy (AE) used to control hourglassing should be monitored to be not more than 1-2% of the Internal Energy (IE) [79].

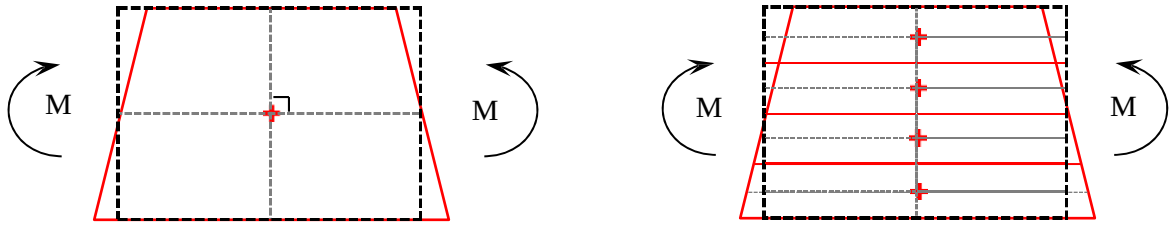

Figure 3.4 *A 2D view of a reduced-integrated linear hexahedron element being subject to pure bending, outlining its inability to detect strain at its integration point (a). The usage of four elements across the concerned thickness will mitigate this problem (b) (adapted from [79]).*

The linear reduced-integrated hexahedral element are used more often than the incompatible mode element in studies concerning finite element analysis of stents, despite their underestimation of stress values. This is due to their ability to provide a good balance between accuracy and efficiency. However, a well-structured mesh of incompatible mode elements, with a minimum of four elements across the thickness and width is known to give good results in bending dominated problems [79]. In this study, efficiency was one of the major considerations and hence reduced integrated elements were primarily chosen for the

stent, and provision was made during mesh generations to allow for upgrading to the incompatible mode elements for the mesh sensitivity study.

3.2.2 Mesh generation for the stent

The 23 mm diameter balloon expandable SAT stent was designed to have one-third cyclic-symmetric geometry. A 3D computer model of its one-third geometry was provided by SAT to be used for its full model generation. As can be seen in Figure 3.5, it has a relatively complex geometry and is comprised of several thickness and width changes throughout its structure. In order to be able to generate an optimal structured mesh of hexahedral elements, the one-third model was partitioned into 10 geometrical sections that were categorized in sets so that they could be selected separately and meshed using a suitable meshing technique. However, even with this approach, the formation of structurally sub-optimal elements in the geometrically complex regions, such as the central section which is the meeting point of the two halves of the scallop and the bottom section, continued to affect the quality of the mesh in the surrounding region. Comparing the two meshes generated with and without the employed technique, it was observed that the shape quality of the elements in these regions was noticeably improved in the latter case and their adverse effects on the mesh quality of the surrounding partitions were substantially reduced.

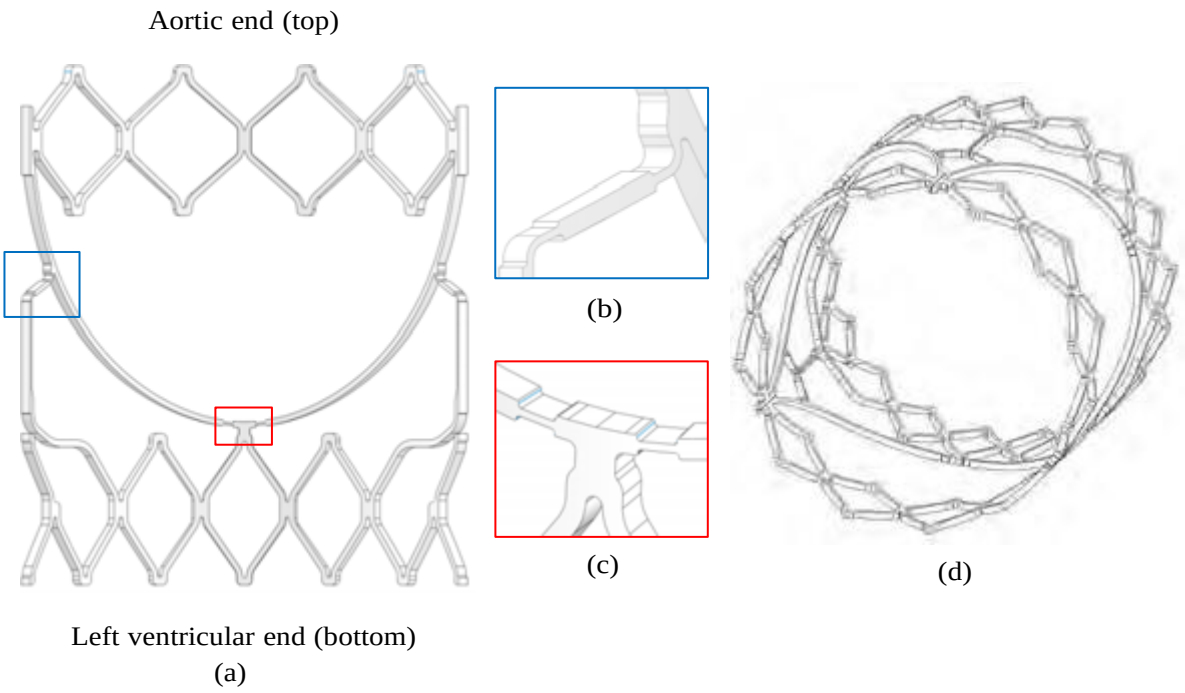

Figure 3.5 *The front view (interior) of the one-third cyclic-symmetric geometry of the SAT stent (a), showing two of its most complex regions, i.e. the upper side arms (b) and the central section (c). The full 3D solid model of the stent (d) was created in Abaqus.*

For the partitioning to be possible, the virtual topology tool in Abaqus was used extensively to combine faces and edges, and to correct some of the extremely small faces that were not recognised by Abaqus during the importing process. Among a few meshing techniques and algorithms that Abaqus utilizes, the structured, sweep and bottom-up techniques performed optimally and hence were utilized for the appropriate partitions.

Based on the observations made from other similar studies and the recommendations on the usage of the reduced-integrated hexahedral element in bending dominated problems, and finally, keeping in mind the possibility of upgrading to incompatible mode elements later, initially a mesh architecture of at least 4 elements across all thickness and 6 elements per 90° bend was adopted, which resulted in a total of 319008 elements. In order to conduct a mesh sensitivity study to determine the most appropriate mesh density for the final FE model of the stent later, the initial mesh density was doubled and used as the second mesh (see Figure 3.6). These details of these generated meshed are shown in Table 3.1.

Table 3.1 *Details of the three generated meshes for the stent.*

Mesh	Type of element	Number of elements
S1	C3D8R	319008
S2	C3D8R	638016
S3	C3D8I	319008

The generated meshes were checked and their quality verified using the mesh verification tool in Abaqus, which examines factors such as elemental shape and size metrics characteristics and reports any potential problems.

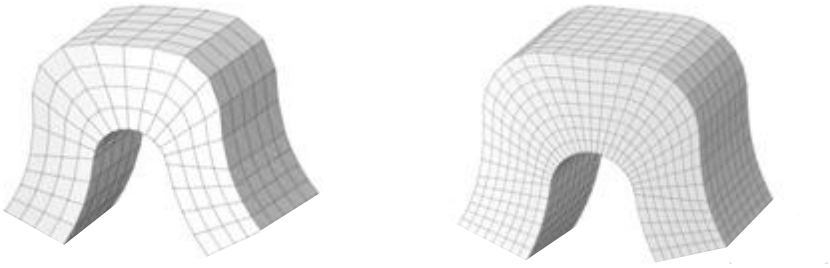

(a) (b)

Figure 3.6 *Two cutaways sections of the stent's top crown, showing the density of the first (a) and second (b) meshes genrated for the mesh sensitivity study.*

3.2.3 The material model for the stent

The SAT stent is made of cobalt nickel chromium molybdenum (CoNiCrMo) alloy, originally known as MP35N, which is highly corrosion resistant and has relatively superior fatigue strength that makes it a suitable material for this type of application [81]. In this study, the mechanical response of this alloy is modelled as an isotropic elasto-plastic material, with a linear elastic initial response followed by plastic behaviour with isotropic hardening, using the mechanical properties and the stress-strain experimental data shown in Table 3.1 and B.1 (see Appendix B). This is the most common approch adapted for the material modelling of stents made of similar materials in other relevent studies.

Table 3.2 The mechanical properties of the MP35N alloy used in this study (from SAT)

Parameter	Value
Density	8415 kg/m^3
Young's modulus	239.5 GPa
Poisson's ratio	0.3775
Yield stress	350 MPa
Ultimate Tensile Stress	1520 MPa

3.3 Solver choice

Finite element analysis of TAVI contains all forms of nonlinearity in structural mechanics, namely material geometric and contact. Hence, a decision had to be made on the type of analysis procedure to be employed based on its ability to handle the severe nonlinearities present in the process. For this reason, following the work by Auricchio et al. [49], a trial simulation was set up by using the first generated mesh of the stent and creating a catheter part for crimping it (see Figure 3.7), which was meshed with 8760 reduced-integrated surface elements. The catheter diameter was set to be slightly larger than the stent outer diameter to avoid initial contact between the two. A radial displacement boundary condition was defined for the catheter's outer surface to crimp the stent to 6 mm diameter. An axial displacement boundary condition was defined for a single node of an element in one of the struts of the stent to constrain the geometry from axial movement. A static general analysis step, as part of Abaqus/Standard, was defined for this analysis with a surface-to-surface contact for catheter-stent interaction and self-contact for the stent's self-interaction. A frictionless hard contact property was assigned to these interactions to avoid any associated numerical issues.

Figure 3.7 *The assembly of the stent and catheter, showing the applied displacement boundary condition to the catheter (arrows) to crimp the stent to 6 mm diameter.*

Many issues were observed as the process for solving the problem progressed. Convergence was the main issue, and despite many modifications made with regard to the incrementation variables and contact settings, all of the simulations aborted at some stage of the simulation process.

Thereafter, the focus was shifted to Abaqus/Explicit which is the second finite element analysis product incorporated in the package and is primarily designed for short duration dynamic events such as ballistic impact and drop testing simulations. Based on the information provided in the documentation of the software, its ability to efficiently handle all forms of nonlinearities and simulations involving large models, for a given limited computer hardware, makes it well suited for the simulation of variety of quasi-static events. Almost all of the studies on the FEA simulation of TAVI, which used Abaqus, and were viewed by the author chose the explicit dynamic solver for their analysis due to its ability in handling the numerical complexities associated with this type of application. However, there are special considerations in utilizing this solver for the particular class of problems that this study is concerned with. These are will be discussed in the next two sections.

3.3.1 An overview of the Abaqus explicit dynamic solver

The explicit dynamic procedure in Abaqus duly makes use of an explicit integration scheme, commonly referred to as forward Euler or central-difference method, for integrating the equations of motion [79]:

$$\mathbf{u}^{i+\frac{1}{2}} = \mathbf{u}^{i-\frac{1}{2}} + \frac{\Delta t^{i+1} + \Delta t^{i}}{2}\mathbf{u}^{i} \ ,$$

$$\mathbf{u}^{i+1} = \mathbf{u}^{i} + \Delta t^{i+1}\mathbf{u}^{i+\frac{1}{2}} \ ,$$

where $\dot{\mathbf{u}}$, $\ddot{\mathbf{u}}$ and $\mathbf{u}$ are velocity, acceleration and displacement respectively, with "i" denoting the increment number. The computational efficiency of this procedure is due to its utilization

of diagonal elemental mass matrices that makes the calculation of the accelerations at the beginning of an increment simpler, since both the inversion of a lumped matrix and its multiplication with a vector are much less computationally intensive [79]. Thus

$$\mathbf{u}^{i} = \mathbf{M}^{-1}(\mathbf{F}^{i} - \mathbf{I}^{i})$$

where $\mathbf{M}$ is the diagonal lumped mass matrix, with $\mathbf{F}$ and $\mathbf{I}$ denoting the applied and internal load vectors. The central difference method is conditionally stable and its stability is dependent on the magnitude of the time incrementation Δt The limit on the time increment, given in terms of the highest eigenvalue of the system (without damping), can be written as

$$\Delta t \leq \frac{2}{\omega_{max}} .$$

Abaqus/Explicit has two methods for estimating the appropriate time incrementation: element-by-element and global. An analysis always starts with the element-by-element estimation, since it is the more conservative than the other, and may switch to the global method if the accuracy of the solution is acceptable. However, for the latter method, if the cost of determining the global time estimation is more than its benefit, the code will only implement the element-by-element method to save computation time. An additional "improved" elemental characteristic length estimation is available for certain element types (plane stress and three-dimensional continuum elements) that result in larger stable time increment utilization compared to more traditional methods [79].

Despite the need for large amounts of small time increments in an analysis using the explicit dynamic solver, these increments are relatively inexpensive. Hence, it is an attractive analysis procedure for problems where the dynamic response time to be modelled is longer by a few orders of magnitude relative to the incremental stability limit. Abaqus/Explicit can efficiently treat severely discontinuous forms of nonlinearities, such as complex contact, which also makes it an attractive candidate for modelling static processes where very general complicated three-dimensional contact is present in deformable bodies. Its general contact algorithm allows for easy and efficient definition of contact between all or selected regions of the model with a single definition. However, it should be mentioned that its elemental library has fewer element types than Abaqus/Standard and mostly includes first-order elements with some exceptions [79].

3.3.2 Quasi-static analyses

In the context of dynamic analyses, a static solution is a long-time solution and hence often computationally impractical to be solved in its real time scale using the explicit dynamic procedure due to the excessive number of very small time increments required. The aim is to model the problem in the shortest possible time, whilst ensuring that the inertial forces are insignificant. Increasing the *loading rate* and *mass scaling* are generally the two ways in which this can be achieved, whilst ensuring that the total Kinetic Energy (KE) is a small fraction, i.e. between 5 to 10%, of the total Internal Energy (IE) of the system [79].

With regard to the loading rate, in order to be able to model a problem that involves a rate-insensitive material quasi-statically, the time period T associated with the lowest frequency of the relevant mode of the structure at hand is of interest since the response of the structure is dominated by this mode [79,82]. This period can be determined by using the equation

$$\mathrm{T} = \frac{1}{f_{structural}} , \tag{3.1}$$

with $f_{structural}$ being the frequency of the relevant mode of the structure. This period is the minimum time that can be used for the loading step and is used for the estimation of the impact velocity for loading the structure. The general recommendation is that the impact velocity should be less than 1% of the wave speed in the material of the structure [79]. In conjunction with a smooth and gradual application of load, this will allow for a quasi-static response of the structure and avoid localization, whilst keeping the kinetic to internal energy ratio within acceptable limits [79].

Mass scaling, on the other hand, allows for an artificial increase in the stable time increment by increasing the mass of the structure. This has a direct impact on the dilatational wave speed in the material, resulting in the reduction of the analysis time. The dilatational wave speed in a material and the stable time increment can be roughly estimated by the equations [79]

$$\mathrm{c_d} = \sqrt{\frac{\mathrm{E}}{\rho}} , \qquad \Delta t = \frac{\mathrm{L^e}}{\mathrm{c_d}} ,$$

where $\mathrm{L^e}$, E and ρ are the smallest characteristic elemental length, Young's modulus and material density respectively. Similar to increasing the loading rate, mass scaling adds unwanted inertial effects and can cause undesired deformations in the concerned structure. Hence, trial simulations should be conducted to find the optimal mass scaling factor so that the simulation time can be reduced whilst obtaining acceptable results.

In Abaqus there are two mass scaling approaches available, namely fixed and variable, which allow for specifying either a direct scaling factor or a desired stable time increment as bases for calculating the corresponding scaling factors. The difference between the two methods is

that for the fixed approach, the scaling factor is applied at the beginning of each analysis step, whilst for the variable approach the masses of the elements are periodically scaled during the step. The second method is most useful when elements experience large deformations or their stiffness properties change drastically during the analysis step [79].

With regard to the trial crimping simulation of the stent that was carried out at the beginning of this section, a natural frequency extraction analysis was performed to determine its lowest radial mode frequency, which was found to be 769.2 Hz. Using equation (3.1) the minimum period that could be used for the concerned quasi-static analysis step was calculated to be 1.3×10^{-3} (s). Hence an explicit dynamic simulation was subsequently defined with the previously mentioned boundary conditions, using the calculated period for its duration. The simulation was conducted using a quadcore desktop computer, which took 31 hours to complete and encountered no problems. Therefore Abaqus/Explicit was chosen to perform the required TAVI simulations in this study. Figure 3.8 shows the deformed configuration and stress distribution of the stent.

3.4 The finite element model of the prosthetic valve

3.4.1 Mesh generation for the prosthetic leaflets

A single 3D shell model of the SAT's one-third cyclic-symmetric leaflet was used to generate the full geometry of the prosthetic valve in Solidworks (see Figure 3.9). The linear reduced-integrated large strain triangular shell element was used for meshing the leaflets. This element is computationally efficient, has no propagating hourglass modes [79] and is better suited for this particular topology and application where the geometry is subjected to large rotations and folding during the crimping and deployment procedure [79].

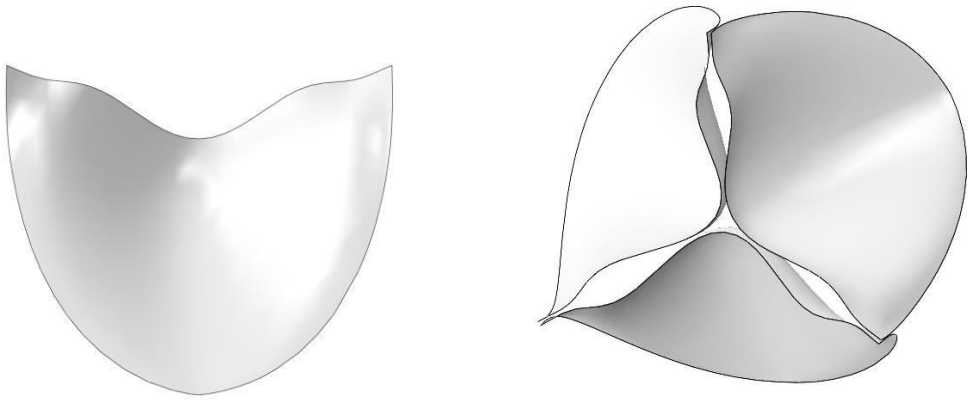

(a) (b)

Figure 3.8 *The front view (interior) of a single shell model of the SAT prosthetic leaflet(a) that was used to generate the full geometry of the valve (b).*

Initially, the quadrilateral shell element with reduced integration was used for meshing the leaflets. However, due to the repeated occurrence of excessive mesh distortion as a result of structurally suboptimal elements, and the need for repeated mesh refinement, which required having to start with an approximate global element size of 0.1 mm, it was decide to switch to triangular elements. With this element, the maximum approximate global elemental size that could be used for the first mesh, with no mesh distortion problem, was 0.3 mm, which allowed for a much more efficient mesh sensitivity study. Table 3.2 shows the details of the five generated meshes for the prosthetic valve that will be used for the mesh sensitivity study.

Table 3.3 *The details of the prosthetic valve meshes.*

Mesh	Approximate global element size (mm)	Number of elements per leaflet
1	0.3	6273
2	0.25	10382
3	0.2	17002
4	0.15	24812
5	0.1	67949

3.4.2 The constitutive material model for the prosthetic valve

The leaflet of interest is made of polymer and is $150\mu m$ thick. The stress-strain results of the uniaxial test conducted on the polymer to characterize its mechanical response (see Table B.2 in Appendix B) were provided by SAT and were used to determine the most suitable constitutive material model for it. The material evaluation tool in Abaqus was utilised for this purpose, which allowed for fitting a suitable material formulation to the test data. The isotropic hyperelastic material model proposed by Marlow [83] matched the experimental data optimally and hence was chosen for the leaflets (see Figure 3.10). This model is given by

$$\Psi = U(J) + \overline{\Psi}(\bar{I}_1)$$

$$\text{where } I_1 = \overline{\lambda}_1^{\,2} + \overline{\lambda}_2^{\,2} + \overline{\lambda}_3^{\,2} \text{ with } \overline{\lambda}_i = J^{1/3}\lambda_i$$

with the $U(J)$ and $\overline{\Psi}(\bar{I}_1)$ denoting the volumetric and deviatoric part of the potential respectively and $\overline{\lambda}_i$ being the deviatoric stretches [79,83]. According to the Abaqus documentation, when only one set of data is available for isotropic hyperelastic material, the model proposed by Marlow is recommended to be adapted for the material. In this process, Abaqus constructs an energy potential to reproduce the uniaxial data exactly, which will

perform reasonably well in the other forms of deformations [79]. The version of Marlow's hyperelastic model that is implemented by Abaqus is a special case of the proposed dual strain invariant based potential, where only the first strain invariant is used, allowing for the exact fitting to the experimental data. For this material, the deviatoric part of the potential was defined by the uniaxial test data and the volumetric part from the defined Poisson's ratio of 0.41.

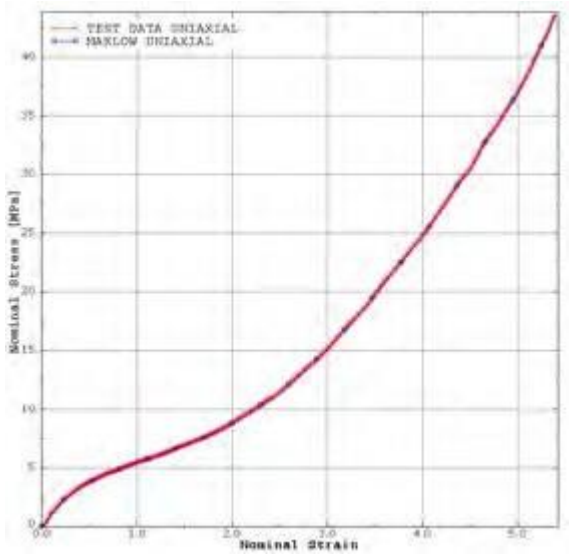

Figure 3.9 *Curve fitting to the experimental uniaxial test data, using the isotropic hyperelastic material model proposed by Marlow.*

3.5 The crimper and the finite element model of the balloon

The SAT stent is crimped to 6 mm diameter before being delivered to the aortic valve location for deployment. The crimper used for this purpose consists of 12 plates which are designed to apply a radial force to the stent to crimp it to the desired diameter. In this study each of these plates was modelled as a single analytical rigid plate with a length and width of 40 and 25 mm to avoid loss of contact when the stent elongates as a result of crimping. It is then patterned circumferentially around the stent to a total number of 12 plates and was only allowed to interact with the stent and prosthetic leaflets during the simulations.

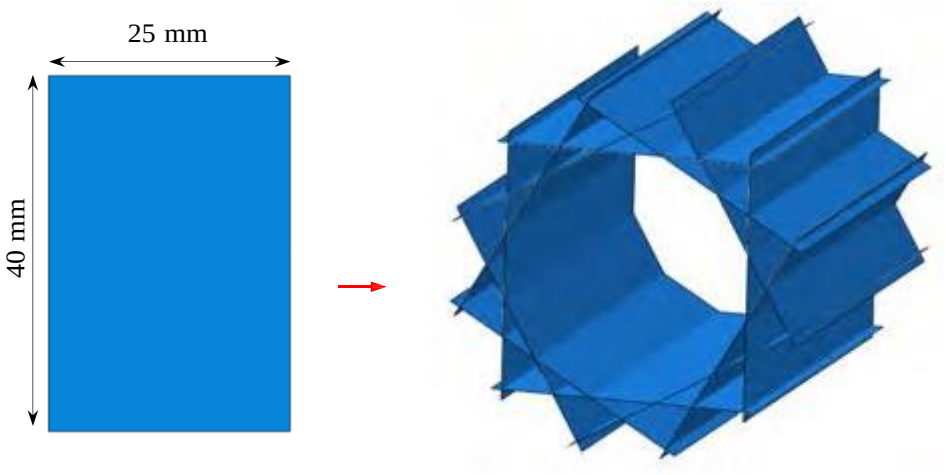

Figure 3.10 *An analytical rigid plate (left) that is patterned circumferentially (right) to mimic the action of an actual crimper.*

The catheter to be used for the expansion and deployment of the stent was designed to have an initial diameter and length of 0.8 and 35 mm respectively to fit axially in between the prosthetic leaflets without any initial interaction. It was modelled as a deformable surface, and was meshed with reduced-integrated four-noded quadrilateral surface elements, which is computationally efficient and suitable for this kind of application. According to the study conducted by Grogan et al. [84] the use of a catheter as a replacement for the balloon to deploy the stent yields similar results for both deformation and stress distribution, whilst eliminating the complexities associated with modelling a balloon and simulating its inflation. A rigid cylinder with the same length as the catheter and a diameter of 0.9 mm was created for the purpose of enfolding the balloon and preventing the crimping prosthetic leaflets from deforming it in the crimping analysis step. It should be noted that the interaction between these two parts are disabled during the TAVI simulations.

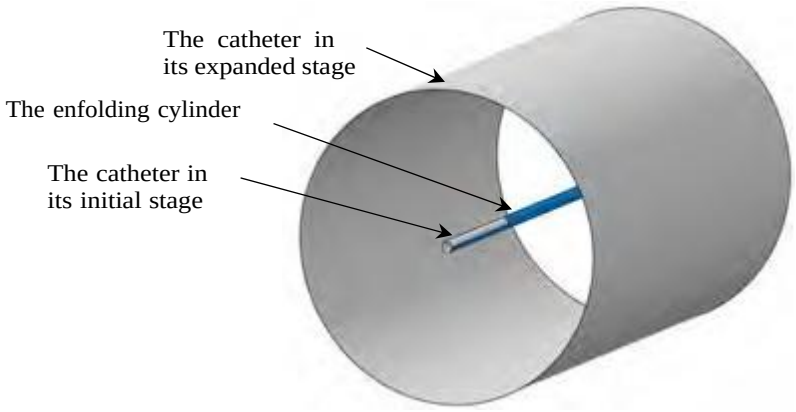

Figure 3.11 *The created model of the catheter (and the enfolding cylinder (blue)) shown in its initial (cutaway view) and expanded form.*

3.6 The crimping of an actual model of the stent for use in validation of the numerical results

In order to be able to validate the results of the mesh sensitivity simulations, an actual model of the stent was crimped in the SAT laboratory, using the manual crimper that consists of 12 plates (see Figure 3.13). Before doing so, its top and bottom diameters and its length were measured and recorded. These measurements were repeated for the recoiled stent, and the results are shown in Table 3.2. It should be mentioned that all measurements were repeated three times and the presented values are the calculated means.

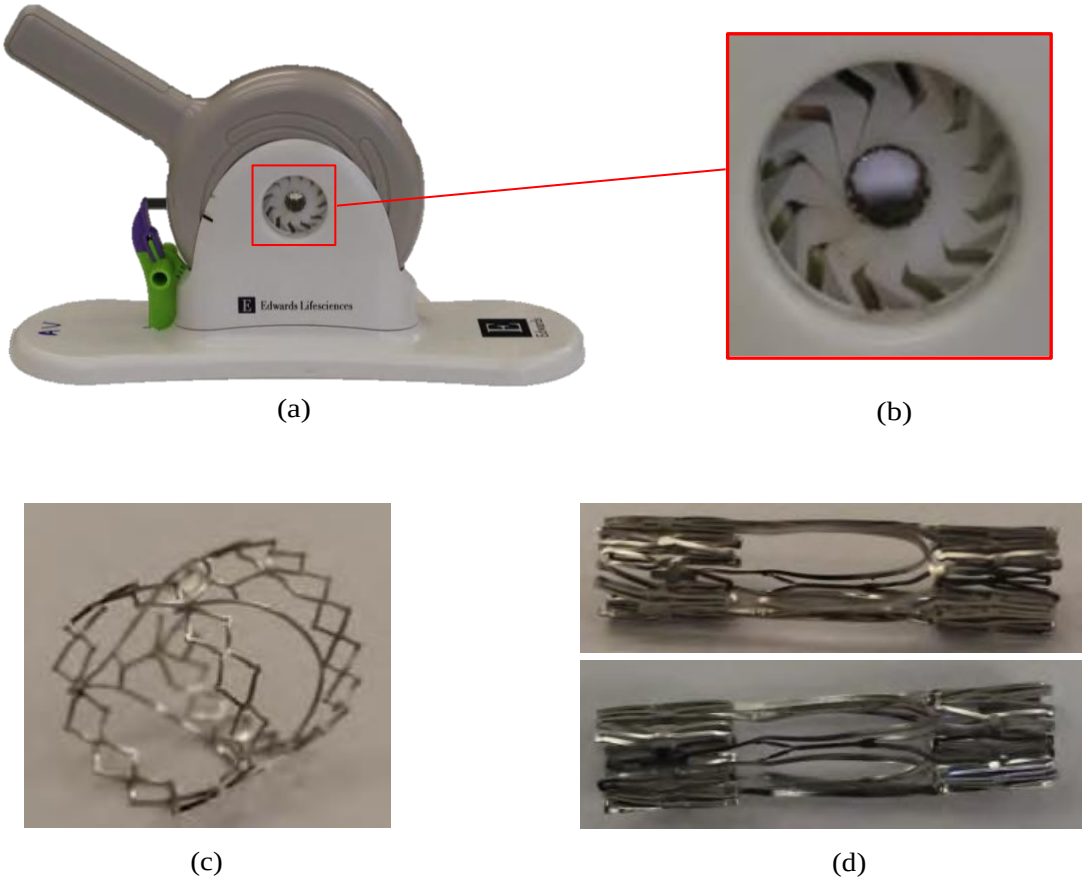

Figure 3.12 *A photograph of the crimper used in the experiment (a), outlining the configuration of plates during the crimping process (b). The undeformed geometry of the stent used in this experiment (c), and two views of its crimped geometry (d).*

The elastic radial recoil "$R_{\%}$" of a stent is mainly dependent on its geometry, material and strut dimension [85] and is best expressed as a percentage. It is a major design factor, which is generally desired to be minimized specifically after the stent's deployment. Percentage radial recoiling of a stent after crimping can be calculated using the following [86]

$$\mathrm{R}_{\%}{}^{Crimped} = \frac{D_{avg}^{Recoiled} - D^{Crimped}}{D^{Crimped}} \times 100 \quad ,$$

where "D" denotes the diameter of the stent at a particular stage, which is indicated as a superscript. Following a similar logic, the percentage lengthening of a stent after crimping and recoiling can be calculated by the following equation

$$\mathrm{L}_{\%}{}^{Recoiled} = \frac{L_{avg}^{Recoiled} - L_{avg}^{Original}}{L_{avg}^{Original}} \times 100 \quad ,$$

with "L" being the length of the stent at a particular stage. Using these equations, the percentage radial recoil of the stent's top and bottom crown and percentage lengthening were calculated and are also shown in Table 3.2.

Table 3.4 *The recorded measurements (mm) of the stent's dimensions before and after the crimping experiment, and its calculated percentage radial recoil and lengthening.*

Geometry	Top Crown ∅	Bottom Crown ∅	Length
Undeformed	22.60	22.91	23.67
Recoiled	6.43	6.63	29.06
	$\mathrm{R}_{\%}{}^{Crimped}$		$\mathrm{L}_{\%}{}^{Recoiled}$
	7.17	10.50	22.77

3.7 Determining the most suitable mass scaling factor for the stent and its mesh sensitivity study

3.7.1 Mass scaling

Before conducting a mesh sensitivity study for the stent, the most suitable mass scaling factor had to be determined by running a number of trial simulations. Hence, an analysis model was created for the first mesh of the stent to be crimped by the crimping plates. The analysis step time for this simulation was set to be equal to the time period associated with the lowest radial mode frequency of the mesh found in Section 3.3.2. A boundary condition was defined for a node in a designated section of the stent to prevent axial translation. A displacement boundary condition with a smooth amplitude curve was prescribed for the plates to crimp the stent from 23 mm to 6 mm diameter (see Figure 3.13).

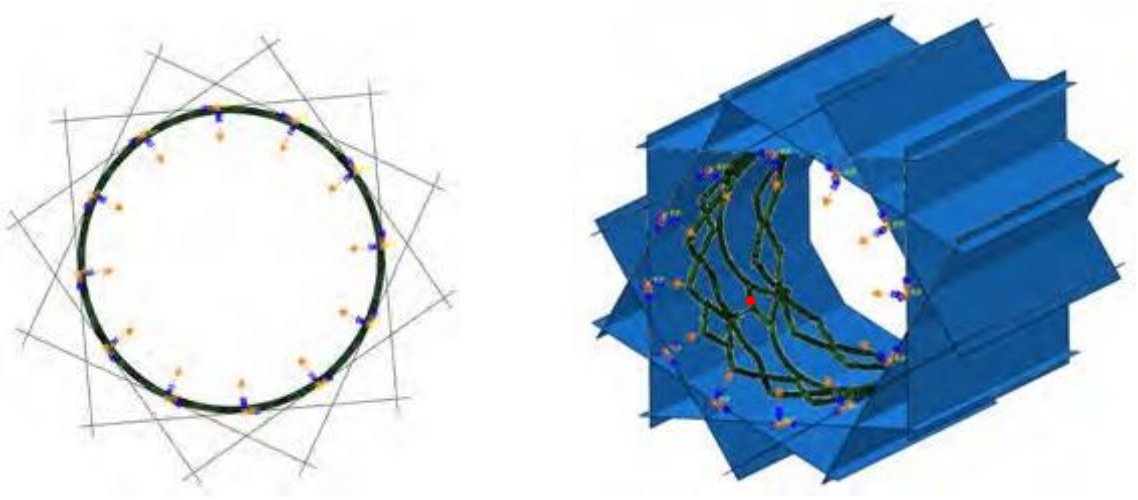

Figure 3.13 *The assembly of the crimping plates and the stent. The displacement boundary condition applied to the plates to crimp the stent is shown with orange arrows. The magnified red dot outlines the position of the displacement boundary condition applied to a node on the stent to prevent axial translation.*

Several trial simulations were conducted to correct the general issues and assess the effect of different mass scaling factors on the energies of the system and on the stent deformation to obtain the most suitable scenario. By comparing the results, it was concluded that the use of variable mass scaling allows for superior results. It was found that the problematic elements, which are mainly located in the complex regions of the stent, cause the initial stable time increment to be as small as 7.14×10^{-10} s. Hence, by defining a target stable time increment for the analysis step to be equal to the average stable time increment of the stent's mesh, i.e. 5.19×10^{-9}s, a good balance was achieved between speeding up the simulations and keeping the inertial effects lower than the recommended 10% threshold (see Figure 3.14). With this scenario, the crimping simulation took 4.5 h to complete. This is a major improvement compared to the simulation conducted at the end of Section 3.3.2, which did not make use of mass scaling. Therefore, the same approach was adopted for the other meshes during the mesh sensitivity study.

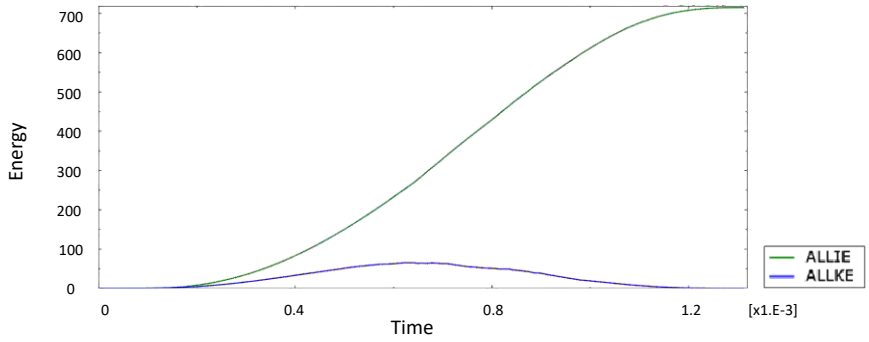

Figure 3.14 *The internal and kinetic energy (mJ) graphs of the mass scaled stent after its crimping simulation. The calculated KE/IE ratio is 8.2%.*

3.7.2 The mesh sensitivity study of the stent and validation of results

At the end of Section 3.2.2, two stent meshes were presented which were created by reviewing other similar studies and taking into account the recommendations on the element choice for bending dominated problems. In this section, a mesh sensitivity and validation study is conducted using those meshes in order to be able to choose the most suitable case that will allow for accurate and efficient TAVI simulations.

The crimping simulation involving the first mesh, in the previous section, was rerun with an additional analysis step in which the stent was allowed to recoil. With the results of this simulation at hand, a similar analysis model was created for the second mesh. Further, in order to assess the performance of incompatible mode elements, an additional analysis model was created with the first mesh, in which the element type was accordingly changed. The results of these simulations are shown in Figure 3.16. The time taken for each simulation along with the KE/IE and AE/IE ratios, and the percentage radial recoil and percentage lengthening were calculated for comparison with the experimental results for validation, and are shown in Table 3.3.

From a geometrical point of view, it can be seen that the recoiled geometry of the stent with incompatible mode elements is different to that observed in the laboratory experiment. The inward buckling of the scallops is also not observed in the simulations with the other two meshes. The recoiled geometries of S1 and S2 however are very similar to those of the laboratory experiment. The difference between the highest stress values observed in these two meshes is approximate 3.4%, which is relatively insignificant, specifically when the time taken for each simulation is also considered.

The calculated AE/IE ratios of S1 and S2 are 2.68% and 1.46%. Although at first this might indicate that the S1 results are affected by the hourglass control utilised; however it should be noted that the recommended threshold of 2% for this ratio is a general guideline and it can be seen that for this specific case, the result is not significantly affected and S1 provides

a good balance between accuracy and efficiency. Hence, S1 is seen to be the better of all the three meshes and was therefore chosen for the TAVI simulations.

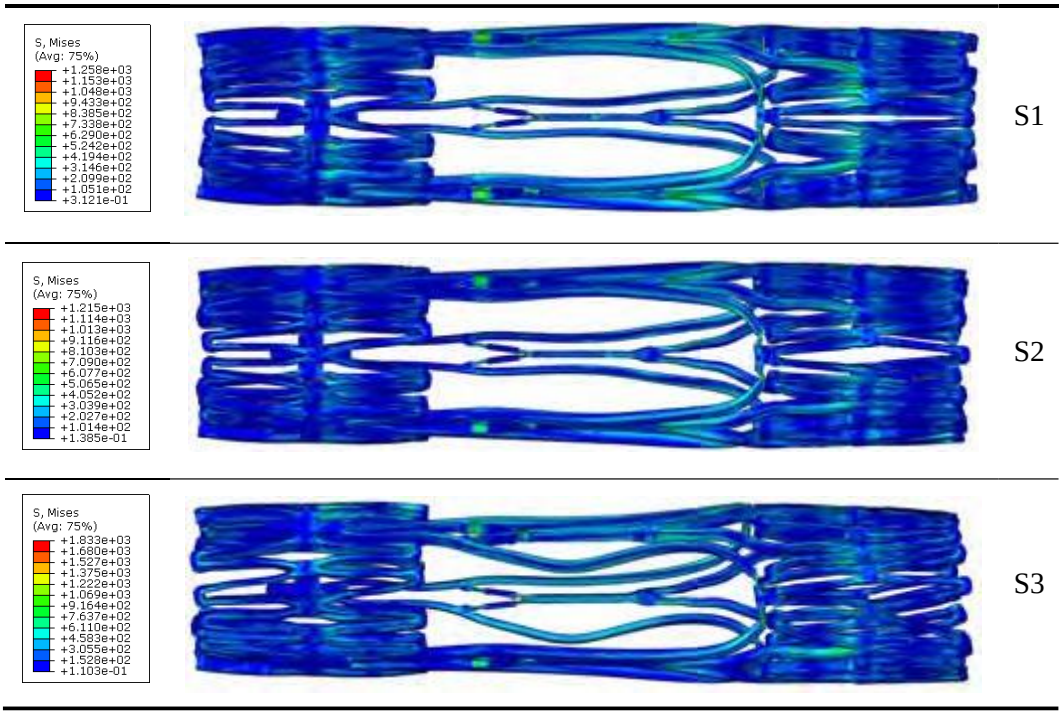

Figure 3.15 *The results of the mesh sensitivity simulations (MPa) that were conducted in order to choose the most appropriate stent mesh for the TAVI simulations. From the top: S1 mesh one with reduced-integrated element; S2 mesh two with reduced-integrated element; and S3 mesh one with incompatible mode element.*

Table 3.5 *The calculated percentage dimensional change and energy ratios of the mesh sensitivity simulations at the end of the recoiling step.*

Mesh	$R_{\%}^{Crimped}$ top	$R_{\%}^{Crimped}$ bottom	$L_{\%}^{Recoiled}$	AE/IE (%)	KE/IE (%)	Time (h)
Experiment	7.17	10.50	22.77	-	-	-
S1	6.83	8.83	25.75	2.60	8.22	9
S2	8.67	13.50	25.49	1.46	8.16	26
S3	6.50	10.83	25.05	-	8.08	53

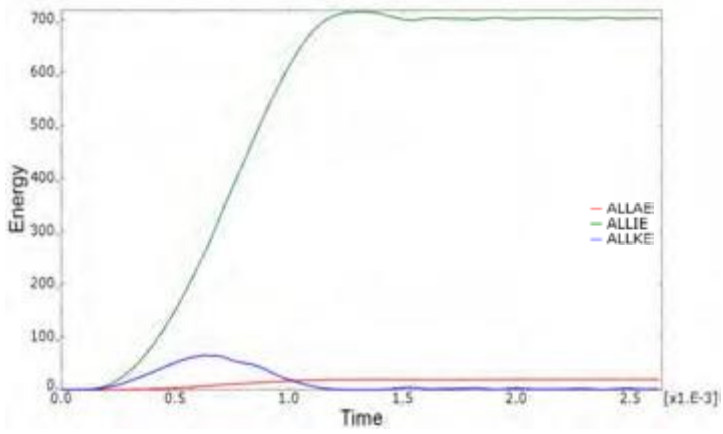

Figure 3.16 *The Artificial (AE), Internal (IE) and Kinetic (KE) energy-time graphs of the crimping and recoiling simulation of the first mesh of the stent (S1).*

3.8 The mesh sensitivity study of the prosthetic valve

An experimentally measured left ventricle and aortic pressure profile of a single systolic-diastolic cycle of a resting heart with a rate of 70 bpm was provided by SAT to be used for assessing the stent's performance after its deployment and subjection to cyclic loading as a result of interacting with the native valve and root. The pressure profile on the leaflets was acquired by subtracting the ventricular from the aortic pressure profile. In order to be able to include this pressure profile in the quasi-statically run mesh sensitivity simulations, its period had to be scaled down. This period had to equal the period associated with the leaflets' lowest structural frequency, which dictates the total simulation time. Therefore, a frequency analysis was performed on the leaflets and their structural mode frequency and associated period were found to be 83 Hz and 12 ms. The original and scaled pressure profiles are shown in Figure 3.17.

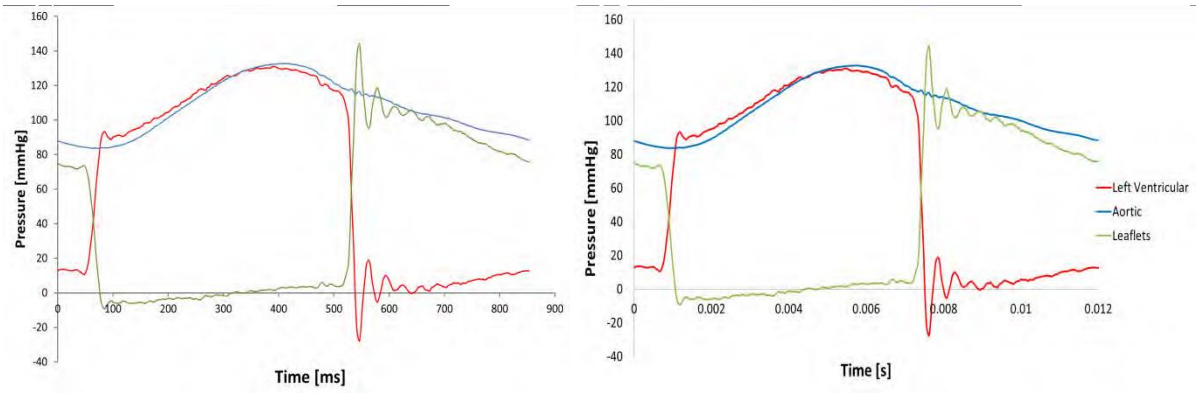

Figure 3.17 *The unscaled (left) and scaled (right) pressure profiles corresponding to the aortic region of the heart.*

An analysis model was created for each generated mesh of the leaflets, in which a displacement boundary condition was defined for the nodes on the edges of the leaflets to prevent them from any movement in order to mimic their connection to the stent. Thereafter, a pressure load was defined on the leaflets, using the generated scaled leaflet pressure profile. Figure 3.19 shows the highest von Mises stress observed at the end of one cardiac cycle in each mesh. The time taken for each simulation to complete is also indicated next to each data point. As can be seen, the difference between the maximum stresses of the fourth and fifth mesh is very small, i.e. approximately 0.28%. However, the time taken for the simulation with the fifth mesh is approximately 2.3 times higher. On the other hand, the difference between the maximum stress in the third mesh and the two proceeding meshes is 0.93 and 1.2% respectively, whilst this mesh is 3.6 and 8.5 times more efficient than the other two. This makes the third mesh a better choice than the fourth mesh since it offers a good balance between accuracy and efficiency.

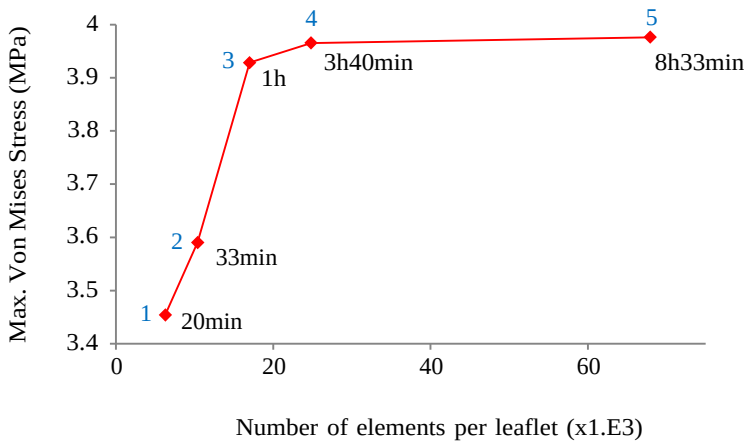

Figure 3.18 *The results of the mesh sensitivity study at the end of a cardiac cycle, conducted for the prosthetic leaflets.*

Chapter 4

Finite Element Models of the Aortic Roots and Native Leaflets, and Simulations of Patient-Specific TAVI

This chapter presents a description of the procedure followed in developing the finite element models of the aortic roots and leaflets of the two patients whose anatomies were extracted from MSCT images and presented at the end of the second chapter. Further, the steps taken in setting up the finite element analyses of TAVI for each patient are outlined. The flow chart below shows a summary of these processes:

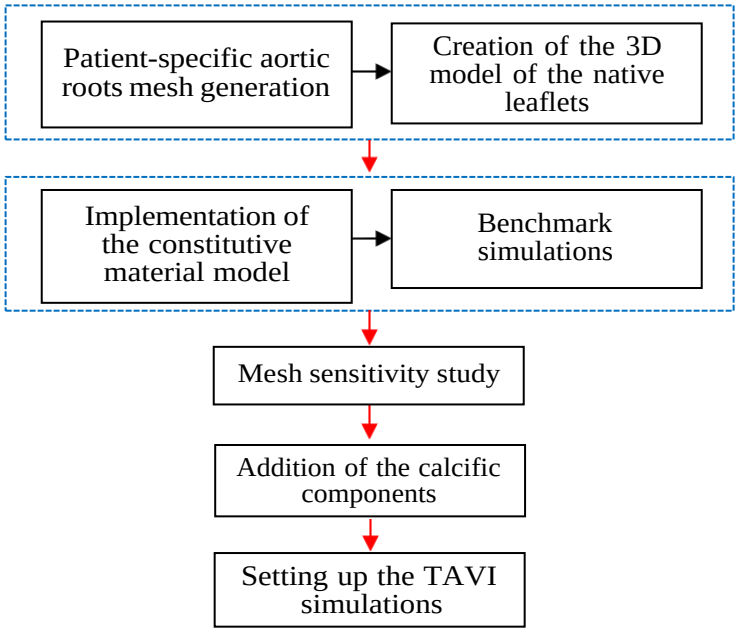

Figure 4.1 *The flow chart of the procedure followed in developing the finite element models of the patient-specific aortic root and leaflets, to be used in the finite element simulations of TAVI.*

4.1 The 3D models of the patient-specific aortic roots and leaflets and their mesh generation

4.1.1 Element selection

Modelling patient-specific aortic roots and leaflets as thin shells instead of solids is a common approach in computational studies [50,87-90] in order to reduce the analysis cost of the required simulations. In this study a similar approach is adapted and the aortic roots and leaflets were modelled as thin shells and meshed with reduced-integrated large-strain quadrilateral shell elements, in order to have an economical simulation and optimally capture the geometry of the models. This is a robust and efficient element and is suitable for a wide variety of applications. However, due to the reduced integration scheme used by this element, the artificial energy of the model, which is added to suppress hourglassing, should be monitored to be less than 1-2% of its internal energy [79].

4.1.2 The patient-specific aortic root mesh generation

After the extraction of the patient-specific aortic root models, they were imported into SolidWorks to be converted into shell models and to eliminate their ragged edges. In order to generate an optimal structured mesh for each patient-specific root, their complex areas were partitioned into several rectangular faces to help improve the structural quality of elements in those regions during mesh generation (see Figure 4.2). Thereafter, a combination of the meshing tools and techniques in Abaqus were utilized to mesh these faces.

Due to the geometrical complexity of these models, the generation of an optimal mesh that captured all the multifarious concave and convex surfaces of the roots was a challenging task and dictated an approximate global element size of less than 0.4 mm. Hence, the meshes for the both patients' roots were generated using an approximate global element size of 0.3 mm, which resulted in 31860 and 22755 elements respectively. Compared to similar studies that used comparable elements, the generated mesh is finer and is expected to offer relatively accurate results. In order to ensure of this, a second mesh was generated for the first patient with the approximate global element size of 0.2 mm, which resulted in 70794 elements, to be used in the mesh sensitivity study, so that the results of the two can be compared and an optimal element size can be chosen for meshing the patient-specific roots and leaflets.

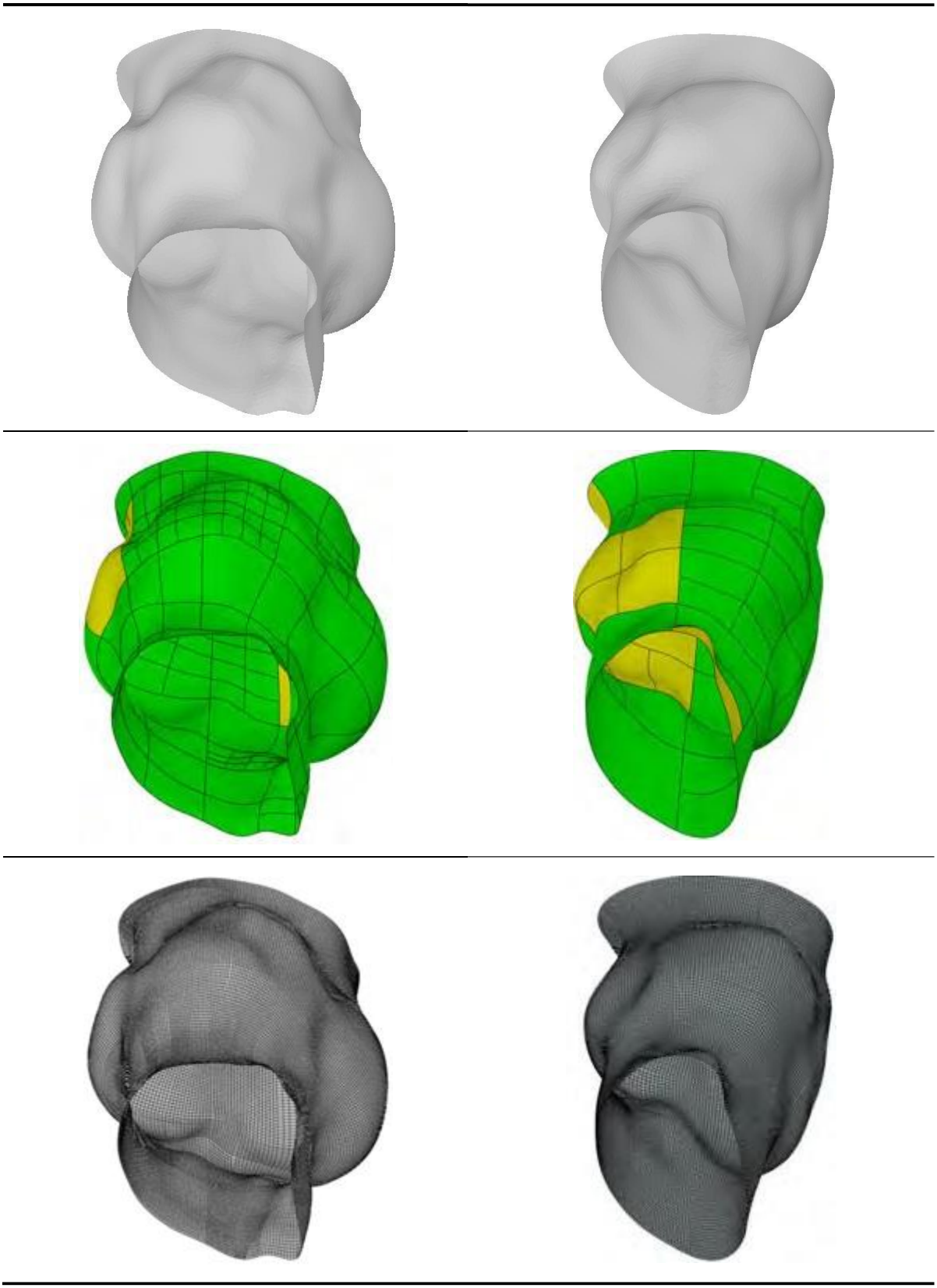

Figure 4.2 *The three stages of mesh generation for the first (left column) and second (right column) patient's 3D aortic root models. The last row shows the first generated mesh for both patients.*

4.1.3 Creation of the native valve leaflets

The native aortic valve leaflets were drawn and added to each root model in SolidWorks by mimicking their observed individual coaptation pattern in the MSCT images of the patients. They are then retracted slightly to create an opening configuration to avoid initial contact with the stent during its recoiling step. These models were then imported into Abaqus to be meshed. Since the geometry of these generated models was relatively simpler, no partitioning was required and these were meshed with the same approximate element size as the roots. Each set of leaflets were then attached to the appropriate root by constraining the degrees of freedom of the nodes on the attaching edges of the leaflet to move with those of the aortic root along this attachment edge.

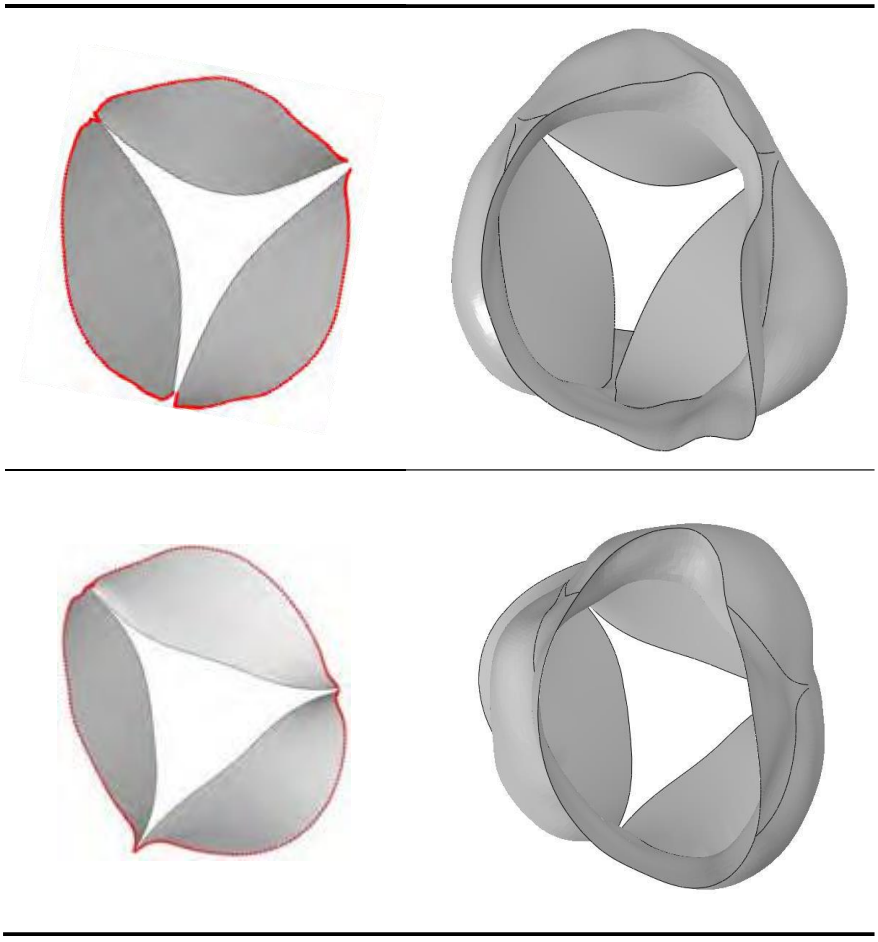

Figure 4.3 *The view from the left ventricle of the first (top) and second (bottom) patients' native leaflets, drawn based on the observations from the MSCT images and their attachment to the respective aortic roots. The nodes on the attachment edges that were used to assemble the leaflets on the respective root are shown in red. These leaflets were modelled with the thickness of 0.5 mm.*

4.2 The Constitutive Material Model of the Aortic Roots and Leaflets

As mentioned in the first chapter of this thesis, the aortic root and leaflet tissues are known to be nearly incompressible and can be modelled as a hyperelastic material with anisotropic response. In this study, the invariant based hyperelastic anisotropic material model proposed by Holzapfel et al. (2000) [39], which was further improved by Gasser et al. (2006) [42] for arterial wall tissue, is implemented for the patent-specific roots, by incorporating two families of collagen fibres (see Figure 4.4 (left)). In order to be able to do this, a global cylindrical coordinate system had to be defined for each of the aortic roots, which served as a guide for the individual elemental coordinate system to which the fibre direction are applied. For the native leaflets on the other hand, one family of collagen is defined circumferentially to mimic the architecture of the tissue. A separate local coordinate system was defined for each leaflet to be able to assign the fibres circumferentially to their elements (see Figure 4.4 (right)).

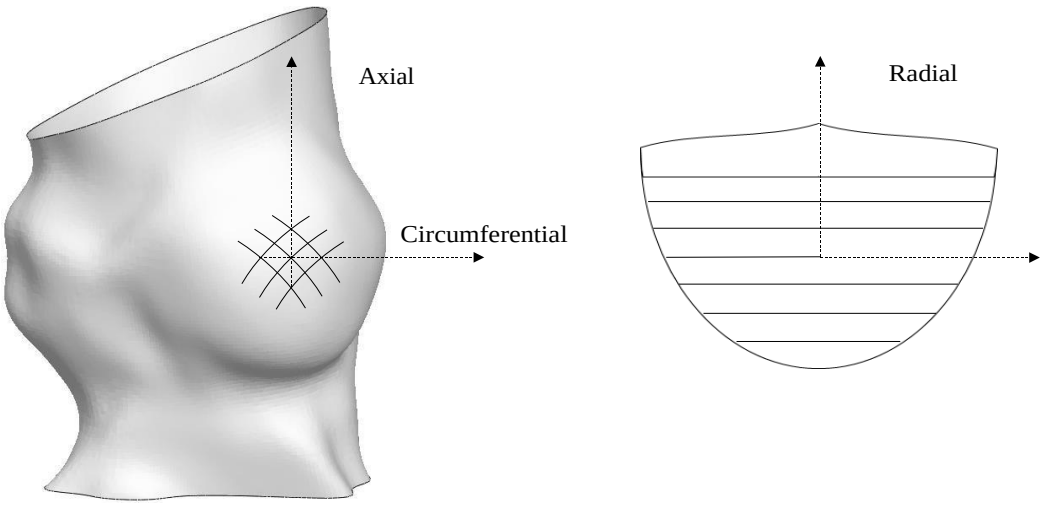

Figure 4.4 *The adapted fibre architecture for the aortic roots (left) and native leaflets (right).*

The material parameters of the material model were obtained from a study by Morganti [47] who used biaxial and uniaxial test data from studies by Martin et al. [37] and Stradins et al. [91] on the human aortic sinuses and leaflets tissues.

4.2.1 Continuum mechanical framework of the implemented constitutive material model

In order to summarize the general continuum mechanical equations that provide the description of the deformation and the stress response of anisotropic hyperelastic materials, consider a solid body $\mathcal{B}_0$ in the reference or undeformed configuration at t_0. Two neighbouring material points characterized by their position vectors $\mathbf{X}(t_0)$ and $\mathbf{Y}(t_0)$ relative to a fixed origin is defined on $\mathcal{B}_0$. It is then assumed that body $\mathcal{B}_0$ moves to acquire a new configuration $\mathcal{B}$ at time t, known as the deformed or current configuration, under the motion φ that carries the two material points to their new position denoted by $\mathbf{x} = \varphi(\mathbf{X},t)$ and $\mathbf{y} = \varphi(\mathbf{Y},t)$ on $\mathcal{B}$ (see Figure 4.5) [92].

A crucial quantity in nonlinear continuum mechanics is the deformation gradient **F**, which is a second order tensor that maps a line element d**X** in the reference configuration to d**x** in the deformed configuration, hence

$$\mathrm{d}\mathbf{x} = \mathbf{F}(\mathbf{X},t)\mathrm{d}\mathbf{X} \qquad \text{with the definition} \qquad \mathbf{F}(\mathbf{X},t) = \frac{\partial \boldsymbol{\varphi}(\mathbf{X},t)}{\partial \mathbf{X}} .$$

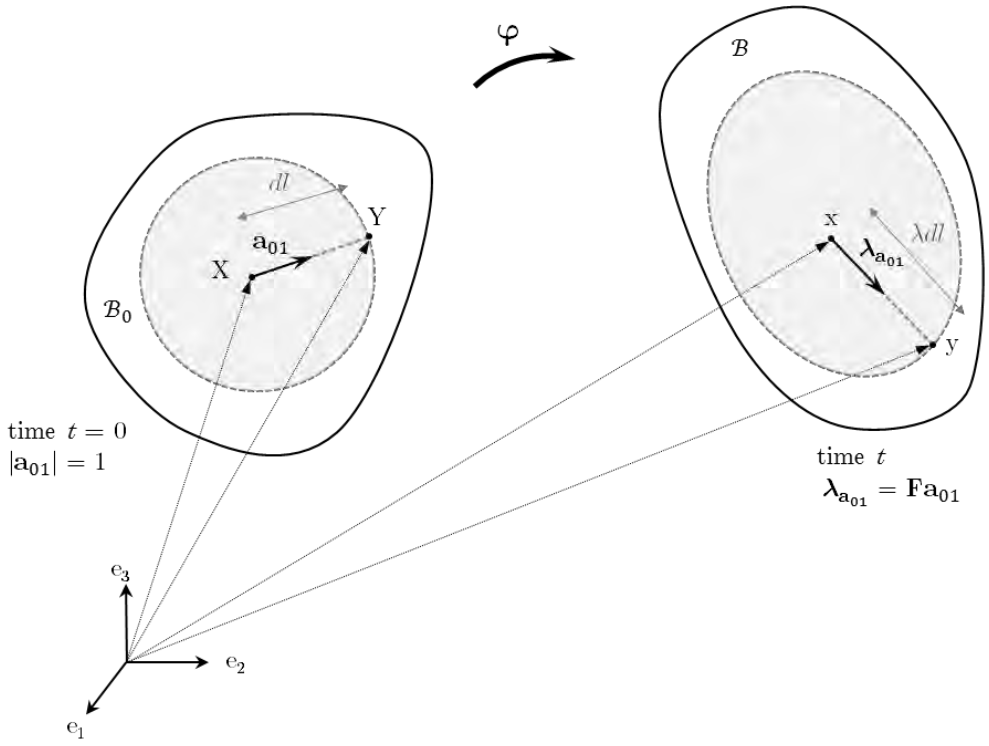

Figure 4.5 *Deformation of a line element* $\mathbf{dX} = \mathbf{Y} - \mathbf{X}$ *with* $\mathbf{a_{01}} = \frac{\mathbf{Y}-\mathbf{X}}{|\mathbf{Y}-\mathbf{X}|}$ *and* $dl = |\mathbf{Y} - \mathbf{X}|$ *in the reference configuration at t = 0 to* $\mathbf{dx} = \mathbf{y} - \mathbf{x}$ *with length* $|\mathbf{y} - \mathbf{x}| = \lambda dl$ *in the current configuration at time t (adapted from [92]).*

For a material that incorporates two families of fibres as reinforcements, the stress at a material point depends on $\mathbf{F}$ and the two preferred directions, commonly known as fibre direction. These directions at material point $\mathrm{X} \in \mathcal{B}_0$ are defined as two unit vectors $\mathbf{a}_{01}(\mathbf{X})$, $|\mathbf{a}_{01}| = 1$ and $\mathbf{a}_{02}(\mathbf{X})$, $|\mathbf{a}_{02}| = 1$ and their presence are assumed to be the only anisotropic property that the solid possess. Under a deformation, the fibres move with the material points of $\mathcal{B}_0$ and attain their new configuration at the deformed state $\mathcal{B}$. Therefore, the new fibre directions at point $\mathrm{x} \in \mathcal{B}_0$ are defined by the unit vectors $\mathbf{a}_1(\mathbf{x}, t)$, $|\mathbf{a}_1| = 1$ and $\mathbf{a}_2(\mathbf{x}, t)$, $|\mathbf{a}_2| = 1$. The length changes of the fibres can be determined by the stretch λ along their individual direction $\mathbf{a}_{01}$ and $\mathbf{a}_{02}$, which is the ratio of the length of a fibre element in the current and reference configurations. For a single fibre direction, shown in Figure 4.5, the stretch vector is defined as [92]

$$\boldsymbol{\lambda}_{\mathbf{a}_{01}}(\mathbf{X}, t) = \mathbf{F}(\mathbf{X}, t)\ \mathbf{a}_{01} \qquad \text{with } |\boldsymbol{\lambda}_{\mathbf{a}_{01}}| = \lambda\ , \tag{4.1}$$

$$\boldsymbol{\lambda}_{\mathbf{a}_{01}} = \lambda\ \mathbf{a}_1\ . \tag{4.2}$$

By combining (4.1) and (4.2), the following equation is driven to relate the fibre direction in the reference and current configurations

$$\lambda\ \mathbf{a}_1(\mathbf{x}, t) = \mathbf{F}(\mathbf{X}, t)\ \mathbf{a}_{01}(\mathbf{X})\ .$$

The square of stretch can then be found by

$$\lambda^2 = \boldsymbol{\lambda}_{\mathbf{a}_{01}} . \boldsymbol{\lambda}_{\mathbf{a}_{01}} = \mathbf{F}\mathbf{a}_{01}\ .\ \mathbf{F}\mathbf{a}_{01}$$

$$= \mathbf{a}_{01}\ .\ \mathbf{F}^{\mathrm{T}}\mathbf{F}\mathbf{a}_{01} = \mathbf{a}_{01}\ .\ \mathbf{C}\mathbf{a}_{01} \quad \text{with} \quad \mathbf{C} = \mathbf{F}^{\mathrm{T}}\mathbf{F}\ .$$

Hence, it can be seen that fibre stretch is dependent on the fibre's direction in the reference configuration $\mathbf{a}_{01}$, and the strain measure known as the right Cauchy-Green deformation tensor [92].

It is further assumed that the concerned solid is hyperelastic and characterized by Helmholtz free energy function Ψ (per unit reference volume). Since the directions are deformation dependent, it is required for the free energy to be explicitly dependent on the right Cauchy-Green deformation tensor $\mathbf{C}$ and the two fibre directions, $\mathbf{a}_{01}$ and $\mathbf{a}_{02}$, in the reference configuration. Since there is no restriction on the senses of the fibre directions, Ψ is taken to be an even function of $\mathbf{a}_{01}$ and $\mathbf{a}_{02}$. By introducing the second order structural tensors $\mathbf{A}_1$ and $\mathbf{A}_2$, which are the tensor product of $\mathbf{a}_{01} \otimes \mathbf{a}_{01}$ and $\mathbf{a}_{02} \otimes \mathbf{a}_{02}$, the Helmholtz free-energy function may then be written as [92]

$$\Psi = \Psi(\mathbf{C}, \mathbf{A}_1, \mathbf{A}_2)\ . \tag{4.3}$$

Now, in order to be able to express a scalar-valued tensor function in terms of principal invariants, a fundamental requirement needs to be satisfied. Known as the "representation theorem for invariants", it states that the free energy must remain unchanged if it undergoes any rotation denoted by the proper orthogonal tensor [92]

$$\Psi(\mathbf{C}, \mathbf{A}_1, \mathbf{A}_2) = \Psi(\mathbf{Q}\mathbf{C}\mathbf{Q}^{\mathrm{T}}, \mathbf{Q}\mathbf{A}_1\mathbf{Q}^{\mathrm{T}}, \mathbf{Q}\mathbf{A}_2\mathbf{Q}^{\mathrm{T}}) \ . \tag{4.4}$$

Since it is a requirement for the free energy to be independent of the coordinate system, hence satisfying the objectivity condition, and since $\mathbf{C}$, $\mathbf{A}_1$ and $\mathbf{A}_2$ are defined in the reference configuration, they remain unaffected by superimposition of rigid-body motion on the current configuration and consequently (4.4) is satisfied. Therefore, $\Psi(\mathbf{C}, \mathbf{A}_1, \mathbf{A}_2)$ may be expressed as a function of independent invariants of its arguments [92]

$$\begin{aligned}\Psi = \Psi[&I_1(\mathbf{C}), I_2(\mathbf{C}), I_3(\mathbf{C}), I_4(\mathbf{C}, \mathbf{a}_{01}), I_5(\mathbf{C}, \mathbf{a}_{01}), I_6(\mathbf{C}, \mathbf{a}_{02}),\\ &I_7(\mathbf{C}, \mathbf{a}_{02}), I_8(\mathbf{C}, \mathbf{a}_{01}, \mathbf{a}_{02}), I_9(\mathbf{a}_{01}, \mathbf{a}_{02})] \ ,\end{aligned} \tag{4.5}$$

with

$$\left.\begin{aligned} I_1(\mathbf{C}) &= \mathrm{tr}\mathbf{C} = \ \lambda_1^2 + \lambda_2^2 + \lambda_3^2 \ , \\ I_2\ \mathbf{C}\ &= \frac{1}{2}[(\mathrm{tr}\mathbf{C})^2 - \mathrm{tr}\ \mathbf{C}^2\ ] = \lambda_1^2\lambda_2^2 + \lambda_1^2\lambda_3^2 + \lambda_2^2\lambda_3^2 \ , \\ I_3(\mathbf{C}) &= \det\mathbf{C} = J^2 = \lambda_1^2\lambda_2^2\lambda_3^2 \ , \end{aligned}\right\} \tag{4.6}$$

$$\left.\begin{aligned} I_4\ \mathbf{C}, \mathbf{a}_{01}\ &= \mathbf{a}_{01} \ . \mathbf{C}\mathbf{a}_{01} = \lambda^2 \ , \\ I_5\ \mathbf{C}, \mathbf{a}_{01}\ &= \mathbf{a}_{01} \ . \mathbf{C}^2\mathbf{a}_{01} \ , \end{aligned}\right\} \tag{4.7}$$

$$\left.\begin{aligned} I_6(\mathbf{C}, \mathbf{a}_{02}) &= \mathbf{a}_{02} \ . \mathbf{C}\mathbf{a}_{02} = \lambda^2 \ , \\ I_7(\mathbf{C}, \mathbf{a}_{02}) &= \mathbf{a}_{02} \ . \mathbf{C}^2\mathbf{a}_{02} \ , \\ I_8(\mathbf{C}, \mathbf{a}_{01}, \mathbf{a}_{02}) &= \mathbf{a}_{01} \ . \mathbf{C}\mathbf{a}_{02} \ , \\ I_9(\mathbf{a}_{01}, \mathbf{a}_{02}) &= (\mathbf{a}_{01} \ . \mathbf{a}_{02})^2 \ . \end{aligned}\right\} \tag{4.8}$$

The invariants I_1, I_2 and I_3 are identical to those in the isotropic case. The pseudo-invariants I_4 and I_5 and I_6 to I_9 characterize the first and second family of fibres with

direction $\mathbf{a}_{01}$ and $\mathbf{a}_{02}$ respectively. The constitutive equation for the stress in the Lagrangian description, i.e. the second Piola-Kirchhoff stress $\mathbf{S}$, is found from [92]

$$\mathbf{S} = 2\frac{\partial \Psi(\mathbf{C}, \mathbf{A}_1, \mathbf{A}_2)}{\partial \mathbf{C}} = 2\sum_{a=1}^{8} \frac{\partial \Psi(I_{1,\dots,}I_8)}{\partial I_a}\frac{\partial I_a}{\partial \mathbf{C}} \ , \tag{4.9}$$

with

$$\left.\begin{aligned} \frac{\partial I_1}{\partial \mathbf{C}} &= \frac{\partial \mathrm{tr}\mathbf{C}}{\partial \mathbf{C}} = \frac{\partial(\mathbf{I}\colon \mathbf{C})}{\partial \mathbf{C}} = \mathbf{I} \ , \\ \frac{\partial I_2}{\partial \mathbf{C}} &= \frac{1}{2}\left(2\mathrm{tr}\mathbf{C}\mathbf{I} - \frac{\partial \mathrm{tr}(\mathbf{C}^2)}{\partial \mathbf{C}}\right) = I_1\mathbf{I} - \mathbf{C} \ , \\ \frac{\partial I_3}{\partial \mathbf{C}} &= I_3\mathbf{C}^{-1} \ , \end{aligned}\right\} \tag{4.10}$$

$$\left.\begin{aligned} \frac{\partial I_4}{\partial \mathbf{C}} &= \mathbf{a}_{01} \otimes \mathbf{a}_{01} \ , \\ \frac{\partial I_5}{\partial \mathbf{C}} &= \mathbf{a}_{01} \otimes \mathbf{C}\mathbf{a}_{01} + \mathbf{a}_{01}\mathbf{C} \otimes \mathbf{a}_{01} \ , \end{aligned}\right\} \tag{4.11}$$

$$\left.\begin{aligned} \frac{\partial I_6}{\partial \mathbf{C}} &= \mathbf{A}_2 \ , \\ \frac{\partial I_7}{\partial \mathbf{C}} &= \mathbf{a}_{02} \otimes \mathbf{C}\mathbf{a}_{02} + \mathbf{a}_{02}\mathbf{C} \otimes \mathbf{a}_{02} \ , \\ \frac{\partial I_8}{\partial \mathbf{C}} &= \frac{1}{2}(\mathbf{a}_{01} \otimes \mathbf{a}_{02} + \mathbf{a}_{02} \otimes \mathbf{a}_{01}) \ . \end{aligned}\right\} \tag{4.12}$$

By substituting (4.10), (4.11) and (4.12) in to (4.9), the expression for $\mathbf{S}$ can be rewritten as

$$\begin{aligned} \mathbf{S} = 2\Bigg[\left(\frac{\partial \Psi}{\partial I_1} + I_1\frac{\partial \Psi}{\partial I_2}\right)\mathbf{I} - \frac{\partial \Psi}{\partial I_2}\mathbf{C} + I_3\frac{\partial \Psi}{\partial I_3}\ \mathbf{C}^{-1} + \frac{\partial \Psi}{\partial I_4}\mathbf{A}_1 + \frac{\partial \Psi}{\partial I_5}\ (\mathbf{a}_{01} \otimes \mathbf{C}\mathbf{a}_{01} + \mathbf{a}_{01}\mathbf{C} \otimes \mathbf{a}_{01}) \\ + \frac{\partial \Psi}{\partial I_6}\mathbf{A}_2 + \frac{\partial \Psi}{\partial I_7}(\mathbf{a}_{02} \otimes \mathbf{C}\mathbf{a}_{02} + \mathbf{a}_{02}\mathbf{C} \otimes \mathbf{a}_{02}) + \frac{1}{2}\frac{\partial \Psi}{\partial I_8}(\mathbf{a}_{01} \otimes \mathbf{a}_{02} \\ + \mathbf{a}_{02} \otimes \mathbf{a}_{01})\Bigg] \ . \end{aligned} \tag{4.13}$$

For a hyperelastic material with one family of fibres, the free energy depends on $\mathbf{C}$ and $\mathbf{A}_1$, therefore

$$\Psi = \Psi(\mathbf{C}, \mathbf{a}_{01} \otimes \mathbf{a}_{01}) \ .$$

There are only two additional invariants to the isotropic case i.e. I_4 and I_5, and the stress is given by

$$\begin{aligned}\mathbf{S} &= 2\frac{\partial\Psi(\mathbf{C},\mathbf{a}_{01}\otimes\mathbf{a}_{01})}{\partial\mathbf{C}} = 2\sum_{a=1}^{5}\frac{\partial\Psi(I_{1,\ldots,}I_5)}{\partial I_a}\frac{\partial I_a}{\partial\mathbf{C}} \\ &= 2\left[\left(\frac{\partial\Psi}{\partial I_1}+I_1\frac{\partial\Psi}{\partial I_2}\right)\mathbf{I}-\frac{\partial\Psi}{\partial I_2}\mathbf{C}+I_3\frac{\partial\Psi}{\partial I_3}\ \mathbf{C}^{-1}\right) \\ &\quad+\ \frac{\partial\Psi}{\partial I_4}\mathbf{a}_{01}\otimes\mathbf{a}_{01}+\frac{\partial\Psi}{\partial I_5}\ (\mathbf{a}_{01}\otimes\mathbf{C}\mathbf{a}_{01}+\mathbf{a}_{01}\mathbf{C}\otimes\mathbf{a}_{01})\Big]. \qquad (4.14)\end{aligned}$$

The Cauchy stress $\boldsymbol{\sigma}$ for the two cases can then obtained by a push forward operation on (4.13) and (4.14) using the relation

$$\boldsymbol{\sigma} = J^{-1}\mathbf{F}\ \mathbf{S}\ \mathbf{F}^{\mathrm{T}}$$

$$\text{where}\quad J=\det\mathbf{F}.$$

4.2.2 An overview of the Holzapfel and Gasser (2006) constitutive material model and its parameters

In the material model proposed by Holzapfel et al. (2000), the Helmholtz free energy function is decoupled into volumetric U and isochoric $\overline{\Psi}$ parts to allow for modelling compressible behaviour of the arterial tissue and avoid numerical complication when full incompressibility cannot or is not desired to be implemented. Thus,

$$\Psi = U(J) + \overline{\Psi}(\overline{\mathbf{C}},\mathbf{a}_{01},\mathbf{a}_{02})$$

where $U(J)$ is the volumetric and $\overline{\Psi}$ is the isochoric contribution to the free energy. The proposed isochoric strain-energy function $\overline{\Psi}$ is split into isotropic and $\overline{\Psi}_{\mathrm{iso}}$ anisotropic $\overline{\Psi}_{\mathrm{aniso}}$ parts, with each part being associated with the respective response of the tissue at different strains. This is based on the histological findings that the wavy collagenous fibres in the arterial wall are not activated at low strains and hence, the isotropic part of the strain energy function is only associated the mechanical response of the matrix material. On the other hand, at relatively high strains, the collagenous fibres almost entirely provide resistance to the applied stretch and their mechanical response is assumed to be governed by $\overline{\Psi}_{\mathrm{aniso}}$. Hence, the proposed additive decomposition of the isochoric strain-energy function is [39]

$$\overline{\Psi}\ (\overline{\mathbf{C}},\mathbf{a}_{01},\mathbf{a}_{02}) = \ \overline{\Psi}_{\mathrm{iso}}(\overline{\mathbf{C}}) + \overline{\Psi}_{\mathrm{aniso}}(\overline{\mathbf{C}},\mathbf{a}_{01},\mathbf{a}_{02})\ , \qquad (4.15)$$

where $\overline{\mathbf{C}} = \overline{\mathbf{F}}^{\mathrm{T}}\overline{\mathbf{F}} = J^{-2/3}\mathbf{C}$, $\overline{\mathbf{F}} = (J^{-1/3}\mathbf{I})\mathbf{F}$.

Following (4.4) and (4.5), (4.15) is written as

$$\overline{\Psi}\ (\overline{\mathbf{C}}, \mathbf{A}_1, \mathbf{A}_2) = \overline{\Psi}_{\mathrm{iso}}(\overline{I}_1, \overline{I}_2) + \ \overline{\Psi}_{\mathrm{aniso}}(\overline{I}_1, \overline{I}_2, \overline{I}_4, \ldots, \overline{I}_8)\ . \tag{4.16}$$

In the case of assuming full incompressibility $\overline{I}_3 = \det\overline{\mathbf{C}} = 1$ and is therefore omitted form the function. For further simplification and minimizing the number of material parameters, the model adapts the reduced form given below, by omitting the invariants $\overline{I}_2$, $\overline{I}_5$, $\overline{I}_7$ and $\overline{I}_8$. Thus,

$$\overline{\Psi}\ (\overline{\mathbf{C}}, \mathbf{A}_1, \mathbf{A}_2) = \overline{\Psi}_{\mathrm{iso}}(\overline{I}_1) + \ \overline{\Psi}_{\mathrm{aniso}}(\overline{I}_4, \overline{I}_6)\ . \tag{4.17}$$

As mentioned in the previous section, $\overline{I}_4$ and $\overline{I}_6$ are the stretch measures for the two families of fibres in the $\mathbf{a}_{01}$ and $\mathbf{a}_{02}$ directions and the anisotropy in the model arise from their existence. The classical neo-Hookean model is adapted for the isotropic part of the strain energy. For the anisotropic part, on the other hand, the strain energy stored by the collagen fibres is described by an exponential function, which is motivated by their strong stiffening effect at high strains [39]

$$\overline{\Psi}_{\mathrm{iso}}(\overline{I}_1) = \ c_{10}(\overline{I}_1 - 3)\ , \tag{4.18}$$

$$\overline{\Psi}_{\mathrm{aniso}}(\overline{I}_4, \overline{I}_6) = \frac{k_1}{2k_2}\ \sum_{i=4,6}\{\exp[k_2(\overline{I}_i - 1)^2 - 1\}\ . \tag{4.19}$$

Combining (4.18) and (4.19), the further simplified free energy function of the model is given as

$$\overline{\Psi} = \ c_{10}\ (\overline{I}_1 - 3) + \ \frac{k_1}{2k_2}\ \sum_{i=1,2}\{\exp[k_2(\overline{I}_{4i} - 1)^2] - 1\}\ , \tag{4.20}$$

where i runs over the number of fibres, $\overline{I}_{4i}$ is the square of stretch in the i^{th} direction, the $c_{10} > 0$ and $k_1 > 0$ are stress like parameters, and k_2 is a dimensionless number. It should be noted that appropriate choices for k_1 and k_2 drive the histologically based assumption that at low strain, the collagen fibres do not influence the response of the tissue. Another important assumption in this model is that the fibres are only active in extension and cannot sustain compressive load due to their wavy structure. Hence, the anisotropic part of the strain-energy function would only contribute when the fibres are in extension i.e. when $\overline{I}_4 > 1$ and $\overline{I}_6 > 1$. If any of these conditions is not satisfied, the relevant part of the anisotropic function is discarded from (4.20) [39].

In the improved model, proposed by Gasser et al. (2006), the anisotropic part of the free energy function is modified to account for fibre dispersion

$$\overline{\Psi} = c_{10}\,(\bar{I}_1 - 3) + \frac{k_1}{2k_2}\sum_{i=1,2}\{\exp[k_2(\kappa\bar{I}_1 + (1-3\kappa)\bar{I}_{4i} - 1)^2] - 1\}\ . \qquad (4.21)$$

Here κ is a constant that incorporates the effect of fibre dispersion in the model and can be determined experimentally or with material parameter calibration. When $\kappa = 0$, no fibre dispersion is accounted for, i.e. perfect alignment of fibres with the specified directions, and when $\kappa = \frac{1}{3}$ the fibres are randomly distributed, resulting in isotropic response of the tissue [42].

For the aortic root and leaflet FE models, it was assumed that the material and structural properties were constant over their respective geometries and that the fibres are embedded in the plane of the individual elements with no radial component. The calibrated material parameters that are used for the roots and leaflets are given in Table 4.1. In this study, the two of family of fibres are assumed to have the same mechanical properties and hence having the same k_1 and k_2 values. Since Abaqus/Explicit has no mechanism to implement full incompressibility, a Poisson's ratio of 0.49 is used for both tissues, which is consistent with parameters acquired from the study by Morganti.

Table 4.1 *The calibrated material parameters for the Holzapfel and Gasser (2006) material model acquired from Morganti et al. [47]. Note that γ is the defined angle between the two families of fibers in degrees.*

Model	Material Parameters				
	c_{10}(kPa)	k_1(kPa)	k_2	κ	γ (deg)
Aortic Roots	38.01	852.5	2245	0.22	38.5
Leaflets	41	14.71	3.83	0.05	-

4.2.3 The benchmark simulations for validating the correct implementation of the constitutive material models

In order to ensure that the methodology used for the implementation of the fibre orientations is correct, the uniaxial benchmark simulations of the adventitial layer of human iliac arteries, which is modelled using the Holzapfel and Gasser (2006) material model with two families of collagen fibres presented in [79], are replicated and the results are compared. The orientation, dimensions, loading and boundary conditions applied to the two excised axial and circumferential specimens are shown in Figure 4.6. Similar to what is presented in [79],

the simulations were conducted using the Abaqus/Standard with material parameters shown in Table 4.2.

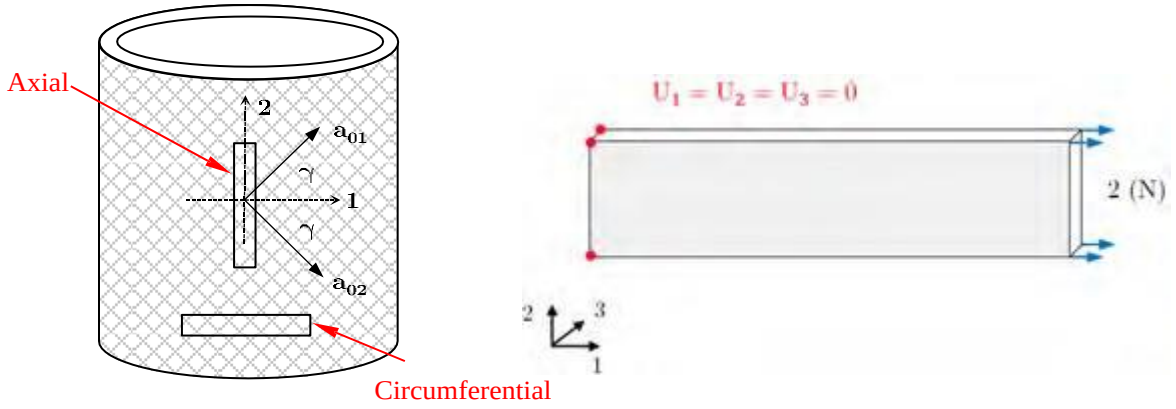

Figure 4.6 *The adapted definition of the orientation of the two families of collagen fibres on the two specimens from the adventitial layer of human iliac arteries presented in [79]. The loading and boundary conditions applied to the strips for the benchmark simulations are shown on the right.*

Table 4.3 *The Holzapfel and Gasser (2006) material model parameters used in the benchmark study (from [79]).*

Ψ	Material Parameters				
	c_{10}(kPa)	k_1(kPa)	k_2	κ	γ (deg)
Holzapfel and Gasser	3.82	996.6	524.6	0.226	49.98

In the simulations presented in [79], the reduced-integrated hexahedral element is used to mesh the specimens. Since in this study the aortic root and leaflets are meshed with the reduced integrated quadrilateral shell element, the replicated benchmark simulations are performed using this element so that the results can be compared for both correctness of implementation and elemental performance.

Figure 4.7 and 4.8 shows the results of the benchmark simulations. As can be seen, the stress distribution and the response of both the axial and circumferential specimens are very similar to that of the ones presented in [79]. As can be seen from Figure 4.8, the circumferential specimen has stretched more than the axial. This is due to γ being larger than $90-\gamma$ and hence the fibres having to rotate through a larger angle to become aligned with the load, resulting greater elongation of the specimen.

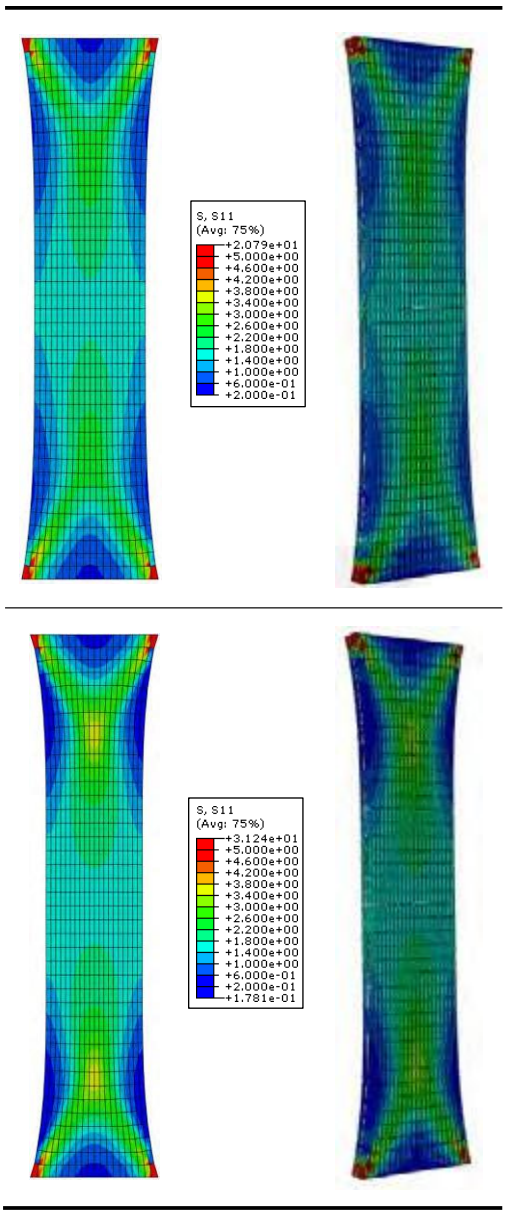

Figure 4.7 *The results of the benchmark simulations, showing the stress in the direction of the applied load for the specimens cut in axial (top) and circumferential (bottom) directions. The left column shows the results for the quadrilateral shell elements and the column on the right shows the results of the same simulation, using reduced-integrated hexahedral elements, presented in [79].*

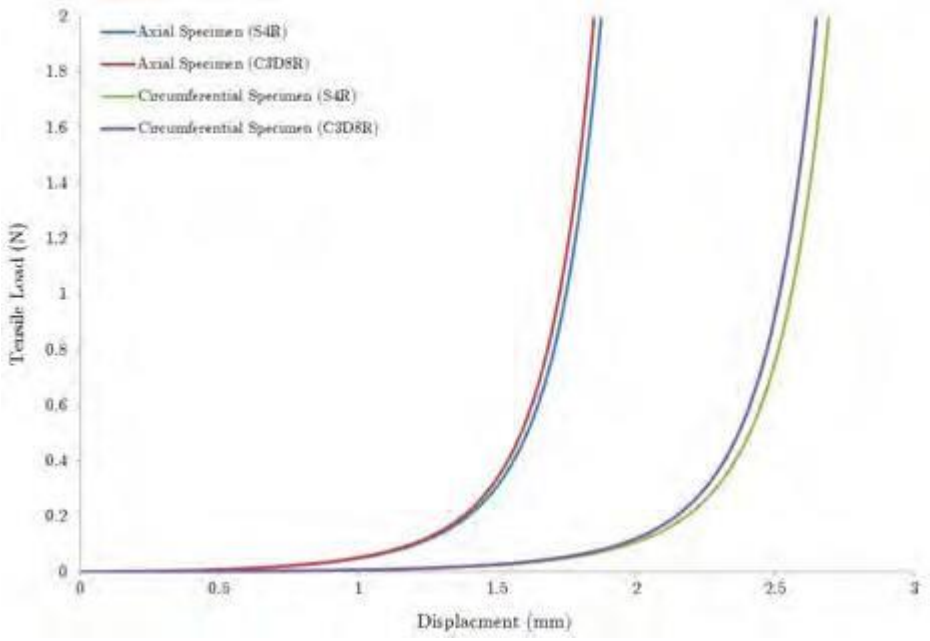

Figure 4.8 *The graph of load vs. displacement response of the benchmark simulations.*

4.3 Mesh sensitivity study of the aortic root and leaflets

In order to reduce the cost of the mesh sensitivity study, it was decided to conduct it in the form of valvuloplasty, using the created catheter. As mentioned in section 4.1.2, since the focus is on two topologically similar patient-specific anatomies, the mesh sensitivity study was only conducted for the first patient's generated meshes and the results were to be used to choose the most suitable global approximate element size for both patients. Hence, a separate analysis model was created for each mesh of the first patients' aortic root and leaflets. Before proceeding to import the balloon in to the assembly module of the analysis models, a frequency analysis was conducted to determine the lowest radial mode frequency of the root-leaflets assemblies and the associate period, which was found to be 11.6 Hz and 86 ms. Thereafter, the balloon was imported into the assemblies and aligned with their central axis. An explicit dynamic analysis step was then defined for each analysis model, assigning the respective time period associated with the found frequency as the duration. A radial displacement boundary condition with a smooth amplitude curve was prescribed for the catheter to expand to a diameter of 23 mm to mimic the action of a balloon. Following the work by Morganti et al. [48], a displacement boundary condition was defined for the edges of the root, i.e. the ventricular out flow tract and the ascending aortic side, to constrain them to their original plane of configuration, whilst allowing for radial movement. The interaction between the catheter, leaflets and the root was defined using a frictionless contact property. These simulations were conducted using a quadcore desktop computer.

By comparing the results of the two simulations, it was observed that the stress distribution pattern in both meshes was similar and that the peak stress in the second mesh was higher by 4.2%. For the native leaflets, these maximum stresses were mainly observed at their central/belly and commissures region. For the aortic root on the other hand, the maximum stresses were mainly observed at the interleaflet triangle regions. The time taken for these two simulations to complete was 4 and 7.5 days respectively. Despite the underestimation of the stress values by a narrow margin, the first mesh allowed for a simulation that was 1.87 times more efficient than that with the second mesh.

It should be noted that the stable time increment of the stent mesh is smaller than that of the other parts in the simulations and therefore dictates the time increment advancement of the entire simulations. With the relatively longer periods required for the analysis steps involving the loading of the aortic roots and leaflets, it can be seen that efficiency of TAVI simulations is highly dependent on the correct choice of the mesh density for these anatomies. With this in mind, it can be deduced that the mesh density associated with 0.3 mm approximate global elemental size will substantially improve the overall efficiency of the TAVI simulation, whilst allowing for an acceptable level of accuracy. Figure 4.9 shows the stress distribution in the chosen mesh.

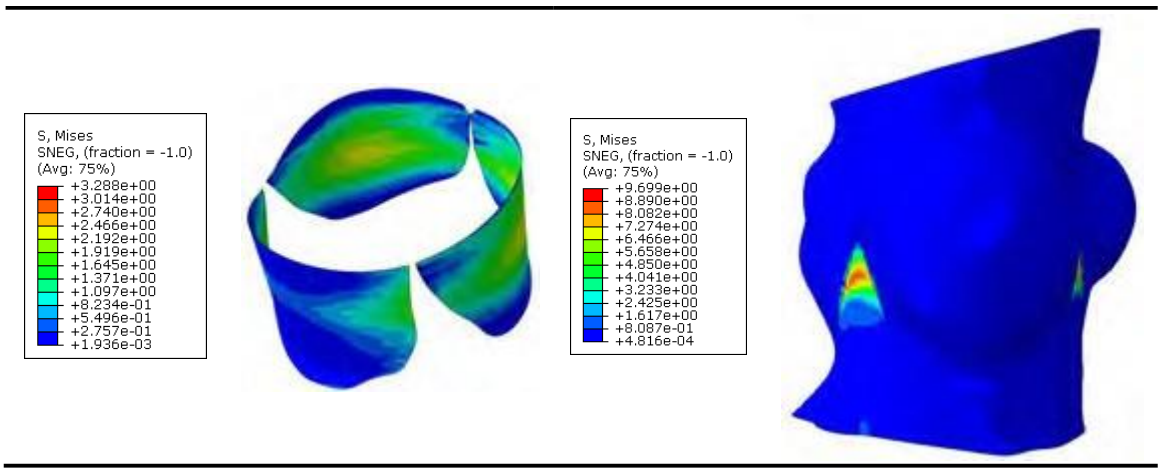

Figure 4.9 *The stress distribution (MPa) in the aortic root and leaflets of the chosen mesh.*

A similar valvuloplasty simulation was conducted for second patient's geometry, in order to assess its performance. It was discovered that at 21 mm expansion of the catheter, the root's tissue could not handle the induced amount of stretch. This was due to its noticeably smaller annular dimension relative to the stent. Hence it was decide to expand the stent to 20 mm diameter in the TAVI simulation, taking in to consideration the further narrowing of the root due to the addition of the calcific components to the leaflets.

4.4 Addition of the calcific components to the native leaflets

In order to be able to see the stenotic components, the MSCT images of the two patients were further processed using the available filtering tools in ScanIP. Thereafter, these components were segmented and converted to three-dimensional models in order to assess their proportions, position and individual shapes so that they could be replicated and added to the patient's leaflets models (see Figure 4.10).

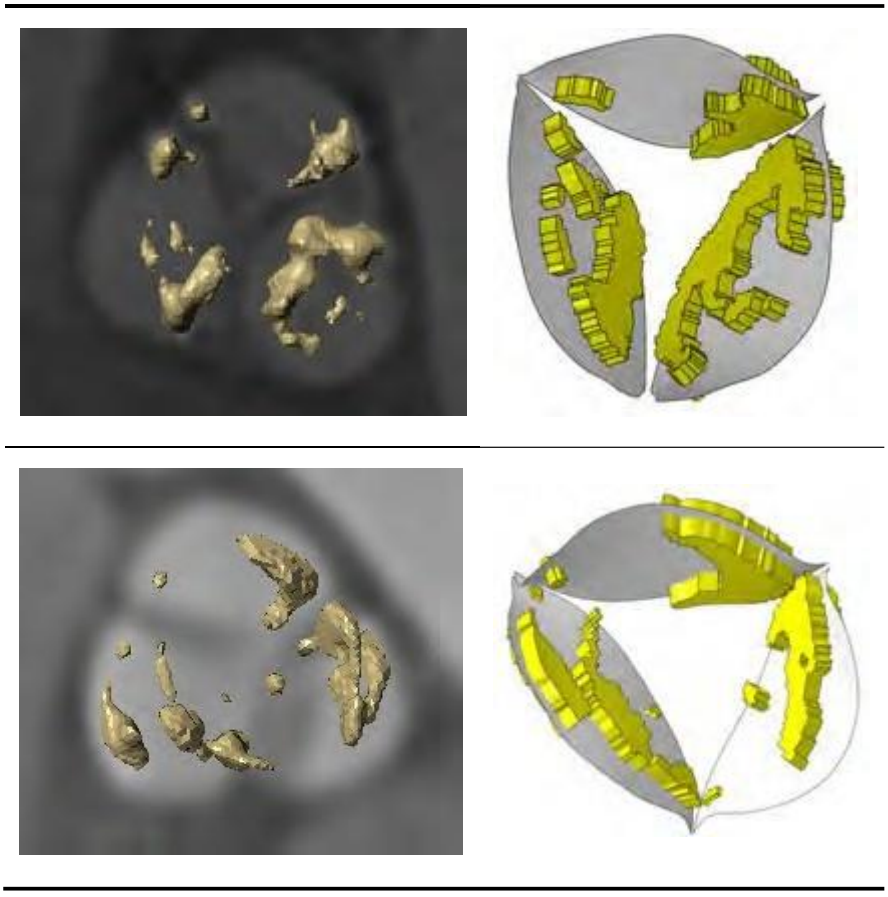

Figure 4.10 *The identified calcific components that were segmented and converted to 3D model (left) and the their FE model on the native leaflets (right) for the first (top) and second (bottom) patient.*

For both patients, no calcific components were observed on the concerned sections of the aortic roots; these were mainly concentrated on the leaflets. For each patient, the thickness of the segmented calcific components was measured and their average was calculated to be 2.7 and 2.3 mm for the first and second patient respectively, so that the entire lesion could be modelled with the same thickness. They were then added to the respective leaflets by initially marking their observed positions and then offsetting elements from the underlying

leaflets i.e. increasing their thickness, with linear hexahedral incompatible mode elements. Following the work by Morganti et al. (2014) [48] the calcifications was modelled using a density of 2000 kg/m^3, Young's modulus of 10 MPa, and Poisson ratio of 0.35.

4.5 Patient-specific finite element analyses models of TAVI procedure

The finite element analysis model of the TAVI procedure for each patient was set-up by creating an analysis model and importing the respective FE models of the patients's root and leaflets into its assembly module. The constraint defined for attaching the leaflets to the root, and the boundary condition defined for restraining the motion of the aortic root-leaflets assembly, mentioned in the previous section, was replicated for the second patient. The FE model of the stent was then added to the assemblies and aligned with their central axis which was also set to be the main alignment axis of the assembly. This was done by following the positioning and deployment instruction set out by SAT, which requires that the nadir of the stent scallops should approximately match with the nadir of the native leaflets. The SAT leaflet's FE model was then imported into assemblies, aligned with the stent, and attached to it by defining a similar attachment constraint that was defined for the roots and leaflets. Thereafter, the crimping plate was imported and tangentially aligned with the stent and patterned around it to form the crimping mechanism. The balloon and its protective cylinder were then imported and aligned with the central axis of the assemblies.

The following analysis steps and boundary conditions were then defined for each analysis model:

***Step 1**: Crimping*

In this step, a radial displacement boundary condition with a smooth amplitude curve was prescribed for the plates to crimp the stent from 23 mm to 6 mm diameter. The restraining displacement boundary condition defined to prevent axial movement of the stent, mentioned in the Section 3.7.1, was repeated here. The duration of the step was set to be equal to the calculated period associated with the stent's radial mode frequency. Each individual plate was only allowed to interact with the stent through frictionless contact since the required friction coefficient for the two materials was unknown.

***Step 2**: Recoiling*

In this step, the crimping plates are moved radially outwards, allowing the stent to recoil freely without any interaction with the surrounding parts in the assembly except for itself. The time period used for this step was the same as the previous step.

***Step 3**: Expansion/ Deployment*

For this step, a radial displacement boundary condition with a smooth amplitude curve was prescribed for the catheter to expand the stent to 23 mm diameter in the first, and 20 mm in the second patient's geometry. The displacement boundary condition that was applied to the edges of the root in the mesh sensitivity study to restrain their motion was repeated here. The required interaction between the catheter and the stent was defined using the same interaction property in step 1. A new interaction property was defined for the contact surfaces of the stent with that of the root, leaflets and calcific components to take into account the friction involved. Since the friction coefficients between stents and aortic root tissues are currently unknown, in this study the approach by Wang et al. [31] is adapted and a friction coefficient of 0.1 was defined for this property. The initial boundary condition used for the stent to prevent it from axial movement in step 1 was propagated to this step. The time period set for this analysis step was the calculated period associated with frequency of the radial mode of the concerned root and leaflets.

***Step 4**: Relaxation*

In this step, the balloon is crimped radially inward to leave the stent in its expanded state and allow it to go through its second recoiling phase. The time period set for this step was the same as the first step.

In order to be able to use the experimentally measured systolic-diastolic pressure profiles, shown in Figure 3.18, to assess the performance of the stent during its interaction with the aortic root and native valve for the individual TAVI simulations, their period had to be rescaled to that of the respective period associated with the frequency of the individual aortic root and leaflets. These profiles were then applied to the appropriate sections of the concerned anatomies, which are colour coded according to the respective pressure profile (see Figure 4.11).

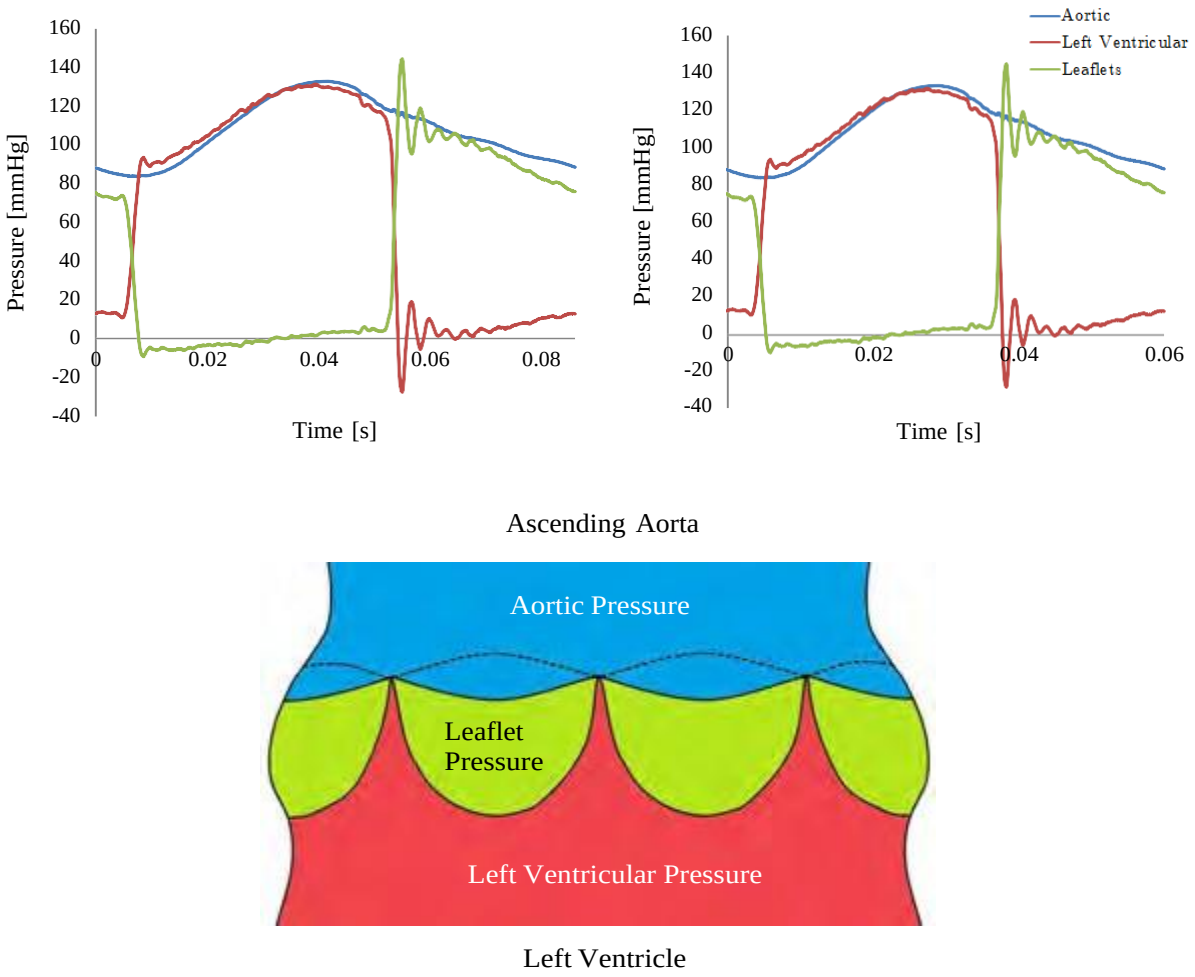

Figure 4.11 *The scaled pressure profiles of the first (left) and second (right) patients applied to the corresponding colour coded aortic region of the heart (bottom). Note that the leaflet pressure is applied to the prosthetic leaflets during the TAVI simulations.*

Hence the fifth analysis step was defined to be:

Step 5*: Interaction*

The pressure profiles are applied to their respective surfaces by defining a pressure load for each. The boundary condition defined for the aortic root edges in the preceding steps is propagated to this analysis step along with all of the interaction definition. The displacement boundary condition that was applied to the stent in steps 1-4 was however cancelled in this step to allow for the free interaction of the stent with the aortic root/leaflets and the calcific components. The time duration of this step was set to be the same as the third step.

Chapter 5

Results and Discussion

This chapter presents the results of the patient-specific TAVI simulations. Firstly, the general outcomes of the TAVI procedure for each patient are discussed, and thereafter the post-operative performance of the stent in each individual case is presented.

The simulations were carried out on a 16 core computer. Typical run times for the full simulations were well in excess of 15 days. For the second patient, some sections of the calcific components resulted in excessive element distortion and, as a result, difficulty in completing the simulation. Thus, while all four stages of the simulations were completed for patient 1, for patient 2 the simulation was stopped at the primary stages of step 4. Nevertheless, the results obtained for patient two sufficed to give a good indication of mechanical response of soft tissues and stent, during the implantation procedure, and these results are presented in this chapter along with those for patient one.

5.1 General outcomes of the TAVI simulations

Figure 5.1 shows the stress distribution in the deformed configuration of aortic root and native valves for the two patients at the end of the expansion/deployment simulation step. This is one of the most crucial stages in of the simulations, since at this point the aortic root and leaflet tissues have to stretch to accommodate the catheter and the stent, and may become damaged or torn during the process. As can be seen, the stress is mainly concentrated in the interleaflet triangle and annulus regions of the aortic root walls, which are the narrowest sections of the root that has to stretch relatively more in order to expand to the designated deployment diameter of the stent. The maximum principal stresses in the aortic root and valve tissues were observed to follow approximately the defined collagen fibre directions (See Figure 5.2). This is consistent with the results of previous studies, which implemented an anisotropic material model for the aortic root and valve [88].

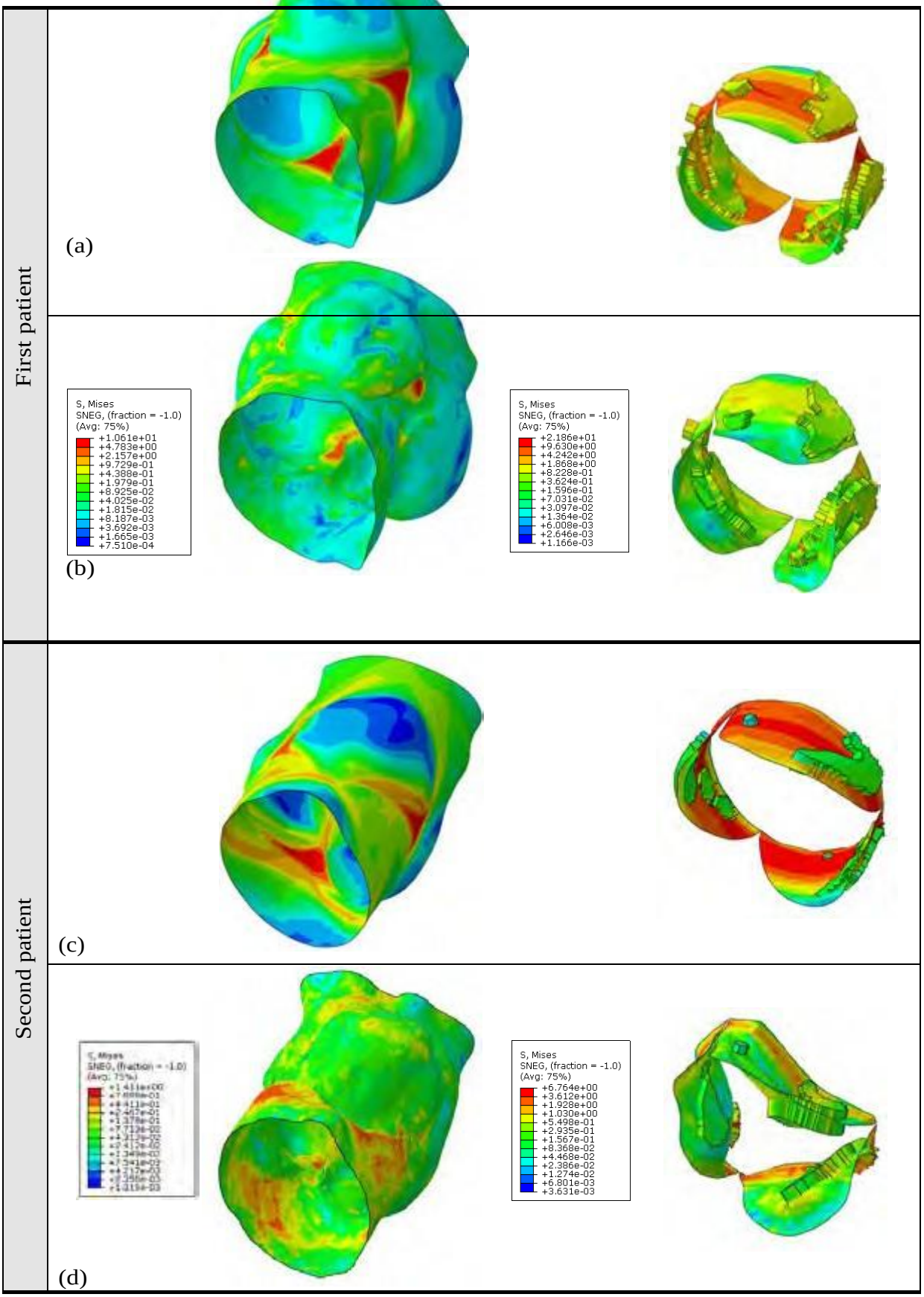

Figure 5.1 *The stress (logarithmic-MPa) distribution in the deformed configuration of aortic roots and leaflets for the two patients at the end of the expansion (a,c) and relaxation (b,d) simulation steps.*

For the leaflets, the stress concentration is observed to be mainly in the belly region and is distributed circumferentially. The circumferentially oriented family of fibres in the leaflet tissue, and the accumulated calcific components that have caused the severe narrowing of the valve regions and act as an obstruction during the deployment process, have led to the stiffer response of the tissue. The effect of the calcific components in particular can clearly be seen by comparing the results of the mesh sensitivity simulation conducted using the first patient's anatomy, presented in Figure 4.9, and the results presented in Figure 5.1 (a). It can be seen that the stress levels in the second case are higher by more than an order of a magnitude. This stiffening effect is consistent with the experimental and numerical results from other studies on calcified aortic valve leaflets.

Figure 5.2 outlines the distribution of the maximum principal stress in the root and leaflet tissues, along with its direction shown with blue arrows.

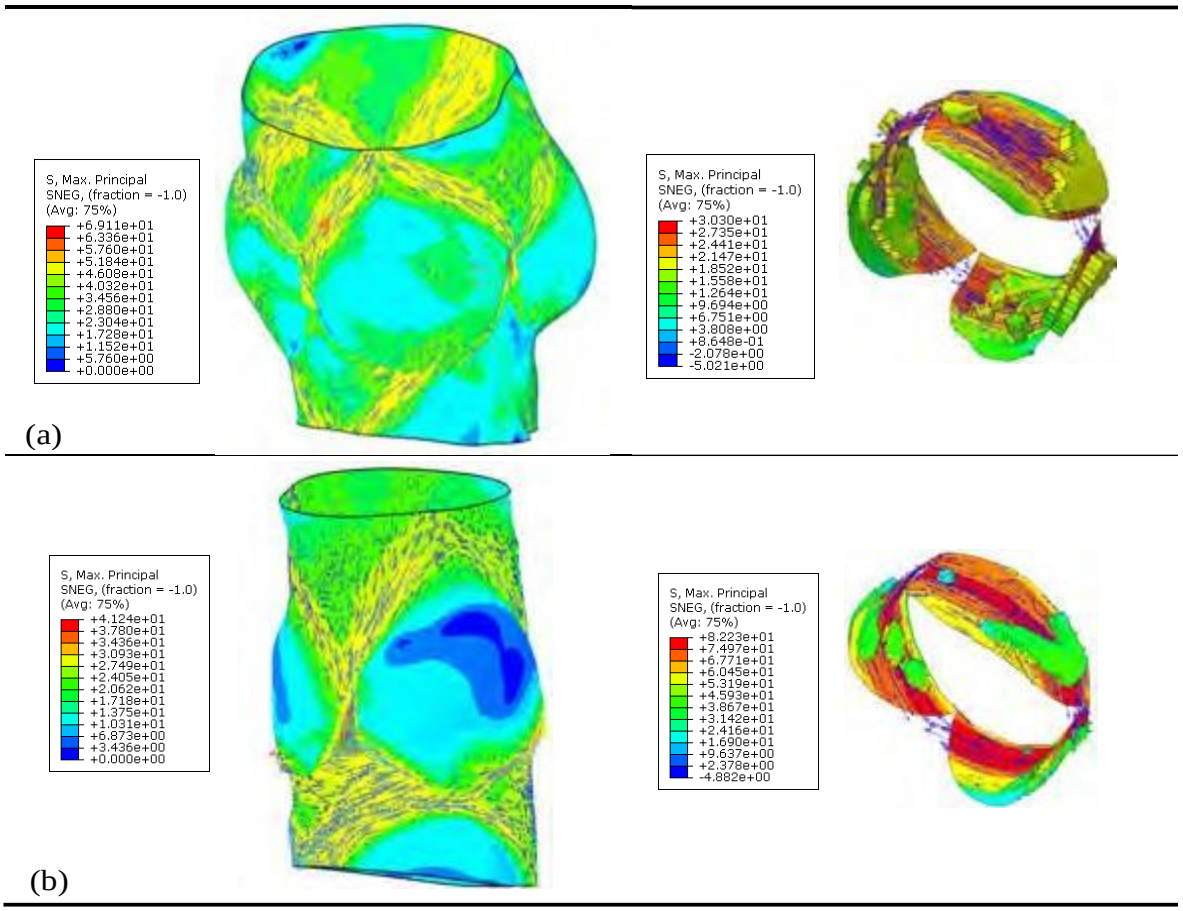

Figure 5.2 *The maximum principal stress distribution (MPa) in the aortic root and leaflet tissues of the first (a) and second (b) patient, outlining its alignment with the defined fibre directions. Note that the blue arrows are the principal stress directions. The defined fiber architecture in these tissues is show in Figure 4.4.*

As can be seen for the first patient the maximum principal stresses in the aortic root wall are more than twice than that in the leaflets tissue. For the second patient this is the opposite, indicating that in the likely case of tissue damage, there is a possibility of detachment of calcific components into the blood stream.

Figure 5.1 (b) and (d) shows that after the removal of the catheter and recoiling of the stent, the stress in the aortic root tissues was substantially reduced. It should be noted that the stress values in the second patient's leaflets were observed to be higher than those of the first patient by more than 3.5 times. This is mainly due to their noticeably smaller structure relative to the stent. By comparing the stress distribution in the aortic root tissue at the end of the expansion and relaxation simulation steps, it can be observed that for the first patient, the stress levels drop by approximately 6 times. For the second patient, however, this drop in stress levels is approximately 29 times, which might be an indication that the tissue was severely damaged during its expansion to accommodate the stent at 20 mm with the presence of the calcific components, and lost most of its elasticity.

Figure 5.3 shows the deployed stents in both patient geometries after the removal of the catheter. As can be seen, in the first patient, the aortic leaflets are successfully pushed behind by the stent and no obstruction of coronary ostia was observed. However, some parts of the leaflets belly region, along with the calcific components, protruded through the openings in the central parts of the stent, but did not impede the opening and coaptation of the prosthetic leaflets (see Figure 5.4 (b) and (c)). For the second patient however, the leaflets almost entirely protruded through the openings in the central parts of the stent. Although from the results it is clear that the stent was not deployed in the anticipated section of the root and should have been deployed at a slightly higher position, it can be seen that even in that case the leaflets would have protruded entirely through the opening of the stent. This will cause a major interference with the function of the prosthetic leaflets and the normal flow of blood during the cardiac cycle. In addition to this, obstruction of the coronary ostia could also be a possibility for this patient.

As mentioned before, the native leaflets and the calcific components are meant to be one the major anchorage providers for the stent. From the results it is evident that for both patients this is not the case. It can be seen that the stent is almost only supported by the annulus of the aortic root, which has result in the lack of adequate support.

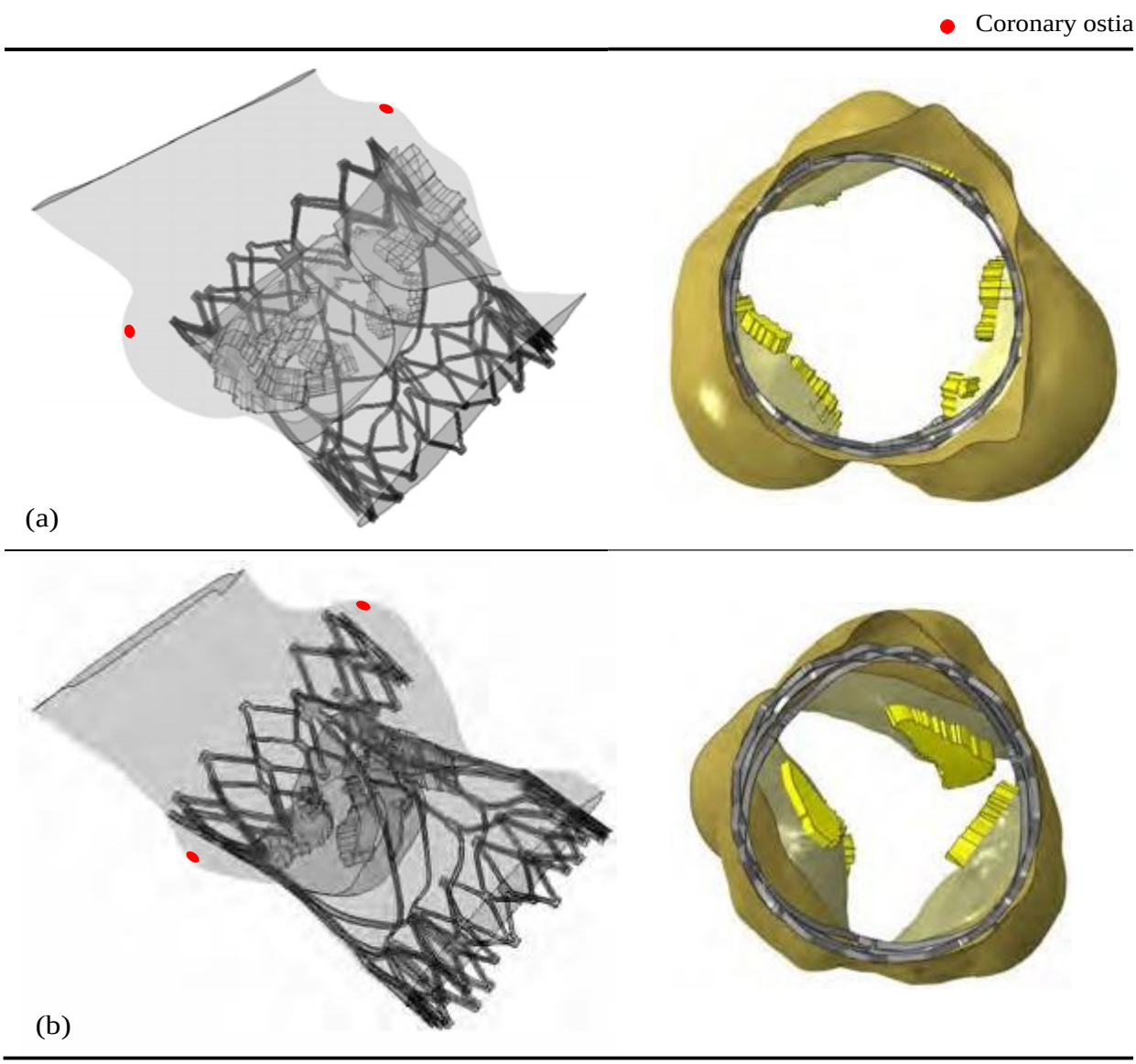

Figure 5.3 *The deployed stents in the first (a) and second (b) patient geometries after the removal of the catheter and its position with respect to the coronary ostia.*

Figure 5.4 shows the deployed stents in the first patient's aortic root, and the stress distribution in the prosthetic valve during the peak diastolic leaflet pressure in the last simulation step. As can be seen, there are two major openings that appears as a result of the recoiling of the stent and reduction in its diameter, and the expansion of the root under the applied aortic and ventricular pressure, which might result in paravalvular leakage. During this simulation step the stent was observed to move towards the left ventricle and back by approximately 3 mm at the peak leaflet pressure during the cardiac cycle. This is due to its inadequate anchorage on the host tissues, and is an indication that in the long term, the stent might migrate and cause further complications. From these observations it can be

concluded that the 23 mm valve might not be the correct choice for this patient, and that a larger valve is required to prevent paravalvular leakage and possible valve migration.

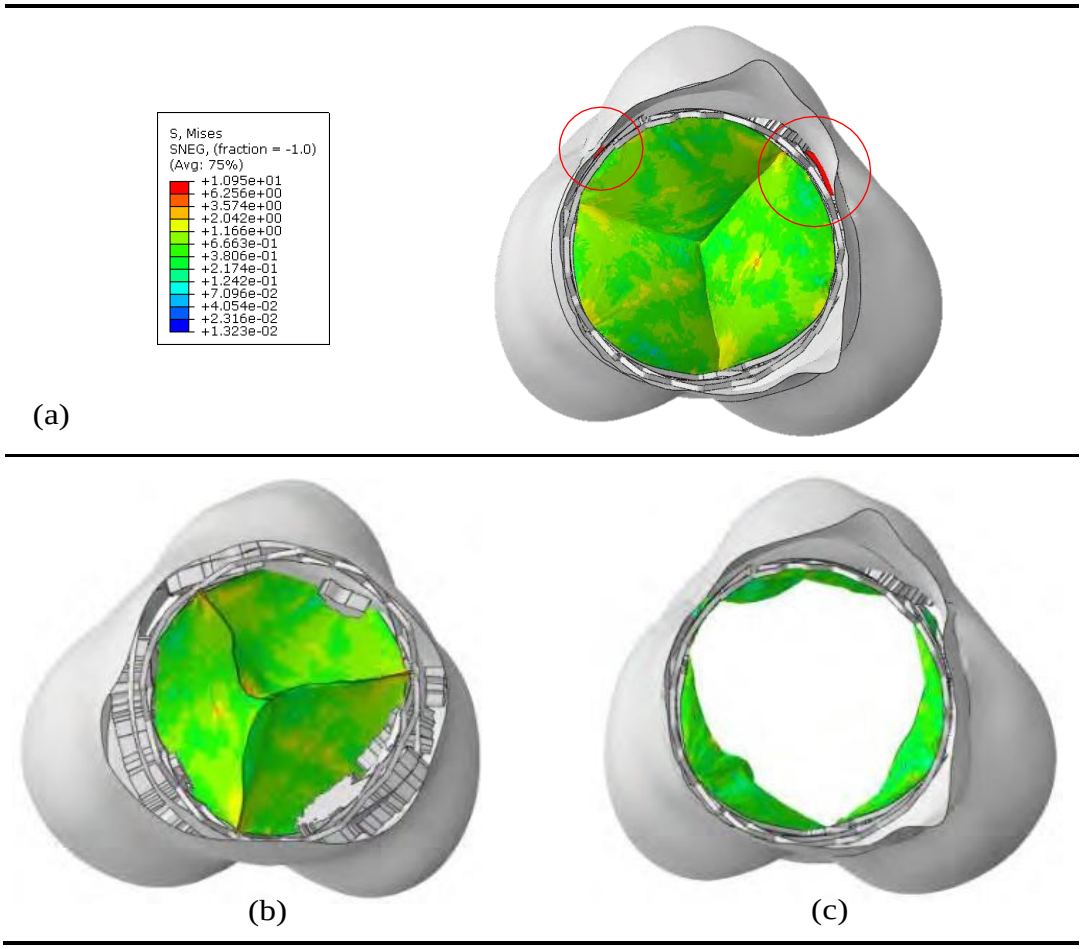

Figure 5.4 *The view from the left ventricle of the first patient's aortic root and the deployed stent, showing the stress (MPa) distribution in the prosthetic valve during the peak diastolic leaflet pressure in the last simulation step, and the possible paravalvular leakage locations (a). The aortic view of the coapted prosthetic leaflets at the same stage of simulations (b), and the view from the left ventricle, showing the prosthetic leaflets in their open positions during the systolic phase of the cardiac cycle.*

5.2 The assessment of the stent's post-operative performance

Figure 5.5 shows the stress distribution in the deformed shapes of the stent and prosthetic leaflets at the end of the crimping, recoiling and expansion simulation steps. The maximum von Mises stress at each individual simulation step is observed to prevail at the complex regions of the stent, i.e. the central and the upper side arms regions. This is due to the fact that these regions have a thinner cross-section and have to endure two phases of large plastic deformations, which makes them more susceptible to fatigue failure. The highest von Mises

stress is observed at the end of the expansion simulation step, when the stent has gone through its second plastic deformation process, and is under pressure from both the host tissue and the catheter.

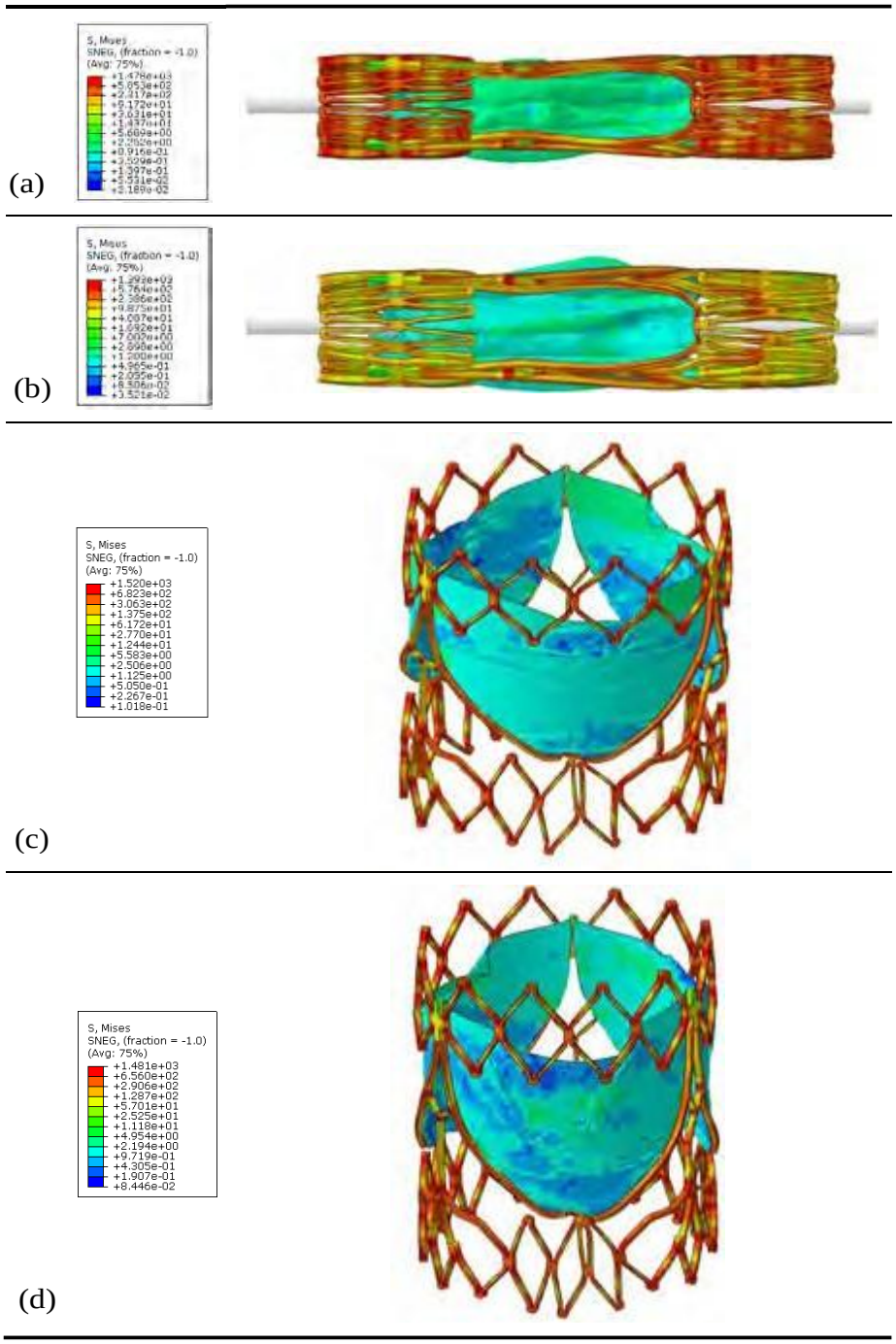

Figure 5.5 *The stress distribution (logarithmic-MPa) in the stent and the prosthetic leaflet' geometries at the end of the crimping (a), recoiling (b), and expansion/deployment simulations steps in the first (c) and second (d) patient.*

Figure 5.6 shows the stress distribution in the geometry of the deployed (recoiled) stent in both patients. It was observed that the topology of the aortic roots and the calcific components has caused the stent to acquire a somewhat elliptical shape after deployment. However, in the first patient, it was observed that throughout the last simulations step the stent maintained its structural integrity, which allowed the prosthetic leaflets to function properly. This is visible from Figure 5.4 where the ventricular and aortic views of the fully opened and closed prosthetic valves are shown. As can be seen, the stent has maintained the native aortic valve leaflets out of the path of the prosthetic leaflets, allowing them to function normally.

Table 5.1 shows the relevant measured dimensions and calculated topological parameters of the stents after deployment. The radial recoil $R_{\%}$ of the top and bottom crowns and the foreshortening $L_{\%}$ of the stent are calculated by using the following equations:

$$R_{\%} = \frac{D^{Expanded} - D_{avg}^{Deployed}}{D^{Expanded}} \times 100 \ ,$$

$$L_{\%} = \frac{L_{avg}^{Recoiled} - L_{avg}^{Deployed}}{L_{avg}^{Recoiled}} \times 100 \ .$$

Here D and L denote the diameter and length of the stent at a particular stage, indicated as a superscript. Note that $L_{avg}^{Recoiled}$ is the recoiled length of the stent at the end of the crimping.

Table 5.1 *The measured dimensions and calculated topological parameters of the deployed stents*

Stent in the:	Ø expanded	Ø top crown	$R_{\%}^{top}$	Ø bottom crown	$R_{\%}^{bottom}$	L deployed	$L_{\%}$
First patient	23	22.02	4.28	22.54	2	23.16	20
Second patient	20	19.46	2.71	19.25	2.71	25.33	12.48

As can be seen, the reduction of the stent's diameter as a result of its radial recoil is approximately between 2 to 4.28 % for the first, and 2.71 to 3.75% for the second patient. This indicates that the stent has the ability to maintain most of the induced radial deformation for its better anchorage in the deployment site. However, by calculating the first patient's average annulus diameter from Table 2.1 Chapter 2 to be 20.98 mm, and compare it with the average recoiled diameter of the stent's top and bottom crowns, which is 22.28 mm, it can be seen that the difference between these dimensions is only 5.83%. This indicates that these dimensions are very close and will result in a lack of adequate radial support from the host tissue; this is the main reason for the observed back and forth movement of the stent during the last simulation step. The same conclusion is drawn by doing a similar comparison for the second patient, with the calculated difference being

7.45%. However, this conclusion for the second patient may not be valid since the stent was designed to be expanded to 23 mm and not 20 mm.

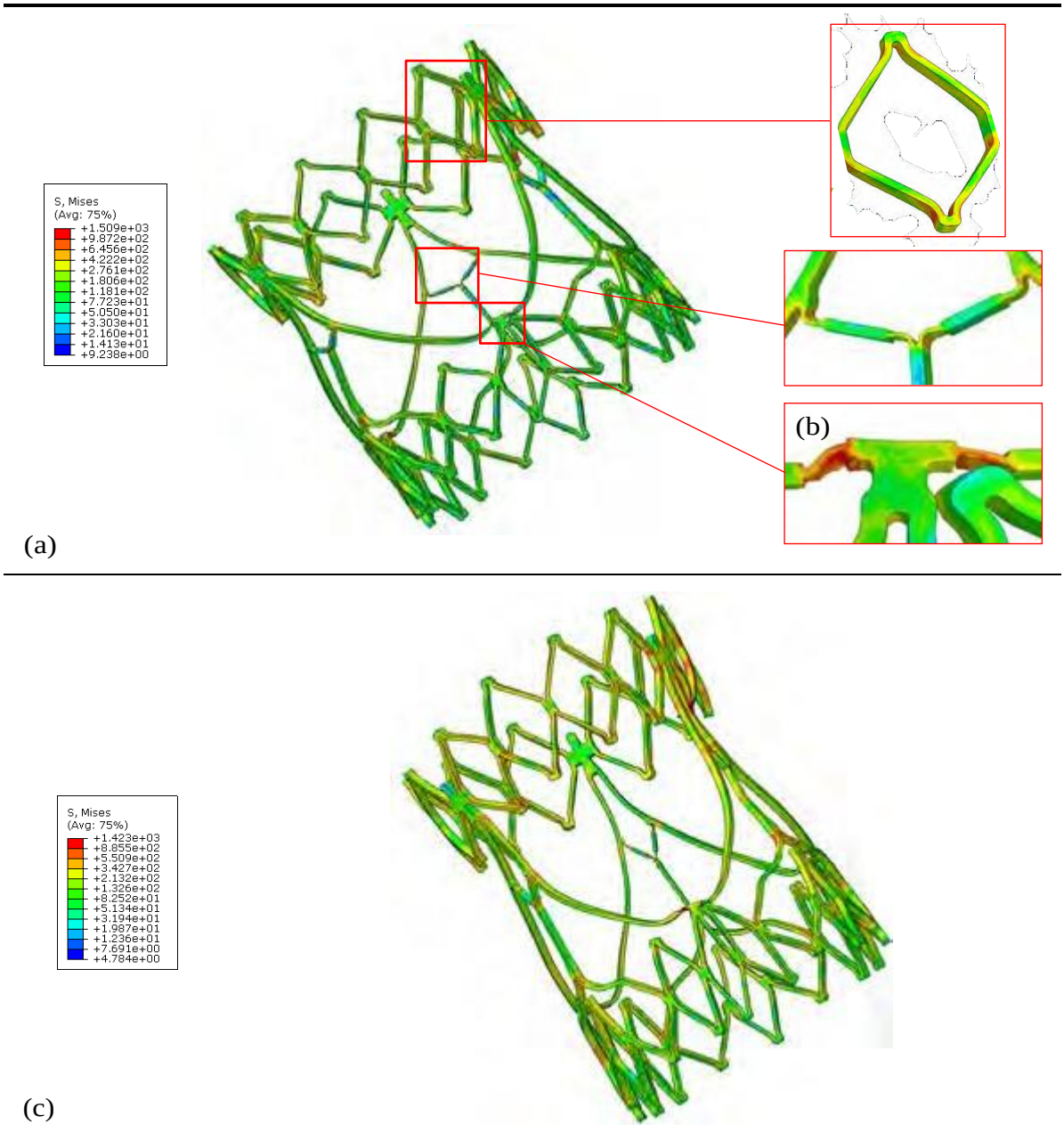

Figure 5.6 *The stress distribution (logarithmic-MPa) in the recoiled geometry of the stent after deployment and removal of the catheter in first (a) and second (c) patient, outlining the regions in which the highest stresses was observed.*

A common pattern of the stent behaviour observed in both patients is that one of the struts in the bottom crown section bundles with the central section of the stent strut after crimping (Figure 5.6 (b)), and stays in that position throughout the remaining steps in the simulation.

Although no significant damage or changes in stress levels were observed in either section at the end of last simulation step, in the long term the central strut section, which has a smaller cross-section, may experience damage due to the continuous interaction with the crown. This will reduce the fatigue life of the stent in this region and may result in its failure.

Chapter 6

Conclusions and Recommendations

6.1 Conclusions

Patient-specific 3D models of aortic roots and calcified valves of two patients, whose chest area MSCT scans were provided by SAT, were extracted and their FE models created in Abaqus. The anisotropic hyperelastic constitutive material model developed by Holzapfel and Gasser (2006) was implemented for their tissues. The 23 mm balloon expandable prosthetic aortic valve, developed by SAT, was used for the TAVI simulations for the purpose of its mechanical assessment and post-operative performance. The stent material was modelled as an isotropic elasto-plastic material, with a linear elastic initial response followed by plastic behaviour, with isotropic hardening, using the mechanical properties and the stress-strain experimental data provided by SAT. The isotropic hyperelastic material model proposed by Marlow (2003) was implemented for the prosthetic leaflets by using the provided uniaxial test data.

For the first patient, the stent was expanded to the designated 23 mm and the simulations were completed. For the second patient however, the annular dimension of the second patient was observed to be noticeable smaller relative to that of the stent diameter. This resulted in the rupture of this patient's geometry in the annular region at the 21 mm expansion increment. Hence, for this patient, the stent was only expanded to 20 mm in the TAVI simulation, which did not complete due to continuous excessive mesh distortion of the calcific components, and stopped at the end of the expansion/deployment simulation step.

From the first patient patient's results, it was observed that the stent maintained its structural integrity throughout the post-deployment simulation step, and successfully pushed the native leaflets back to keep the aortic root clear of the native leaflets. However, by comparing the average diameter of this patient's annulus with the recoiled average diameter of the stent, it can be concluded that the 23 mm stent might have not been the optimal choice for the first patient, since these values are very close. It was observed that

this resulted in the back and forth movement of the stent during the application of the cardiac cycle pressures, which in turn was due to the lack of necessary radial support that lead to its inadequate anchorage on the host tissue. This also resulted in the prevalence of two openings between the stent and the root that might lead to paravalvular leakage. However, no obstruction of the coronary ostia was observed, and prosthetic leaflets were seen to function normally. It was also observed that the impact of the patient-specific anatomical topology on the performance of prosthetic vale was negligible.

For the second patient, it was observed that the nadir of the stent scallops did not match with that of the native leaflets after deployment, as initially anticipated, and should have been deployed slightly higher in the root. However from the result in general it can be concluded that the 23 mm stent is too large for this patient and possibly will cause tissue damage. Even if this patient had a more compliant aortic tissue and the stent could be deployed to its designated 23 mm diameter, the native leaflets would have protruded through the opening in the central regions of the stent and interfered with the correct functioning of the valve and caused other complications.

Due to the nature of the application, which required simulating large deformations, excessive mesh distortion was a common occurrence in this project. In order to allow for the continuation of the simulations, the problematic elements, which were located in the calcific components, were deleted. Similarly, excessive incremental rotation of certain elements of the prosthetic leaflets and the aortic root, lead to continuous stoppage of the simulations. These were two of the main reasons for choosing to start with small approximate element size for meshing these parts.

6.2 Limitations of this work

In this study, the patient-specific aortic roots were models with shell elements. This was mainly to reduce the cost of the concerned analyses. However, hexahedral elements, particularly incompatible mode element, might offer a better and more accurate representation of the induced stresses. Further, pre-stress, which is known to exist in arterial tissues, was not included in the developed FE models of the aortic roots. This was mainly due to the time limitation. Its inclusion would have resulted in a more accurate prediction of the tissue response under the induced expansions. Generally, due to the complexity associated with development of TAVI simulation, inclusion of pre-stress in the aortic root's tissue is almost always omitted, and almost none of the similar studies found by the author accounted for it. Incorporation of a damage mechanism into the developed FE model was not part of the scope of this project. However, its inclusion will further improve the reliability of the model.

6.3 Recommendations for future work

In this study, the stent was meshed with reduced-integration linear hexahedral elements. The maximum stress and strain usually prevails on the surface of the stent due to the nature of the problem. Due to the fact that material calculations are conducted at the integration points, errors might have been introduced in the analysis results due to extrapolation over a larger distance relative to the fully integrated elements. In order to avoid this potential problem, maintaining the efficiency of the current mesh, and increasing the accuracy of the solution, overlay membrane elements can be used in conjunction with the reduced-integration linear hexahedral elements to introduce more integration points on the surface of the stent to avoid underestimation of the stresses.

From the observations made during post-processing of the results, it is recommended to apply the required boundary condition for constraining the stent from axial movement to one of the end surfaces. This will avoid the observed stress localisation at a point, when this boundary condition was applied to a single node on the stent structure, which is unfortunately the most common axial constraining method used by previous studies.

In order to be able to assess the post-operative performance of the stent more comprehensively, it is recommended that a fatigue life assessment study be performed on the stent's deformed geometry at the end of the last simulation step. For this to be possible, it is necessary to acquire mechanical properties of the MP35N alloy used for the stents.

With regard to the patient-specific aortic root FE models, the incompatible model element, which has been used previously in other similar studies, should be used in the future to be able to model the response of the tissue more accurately, and capture the local peak stress and strain on the surface and through the thickness, when time is not a major limitation. For the leaflets, it is recommended that a smaller element size be used in future to avoid mesh distortions of the calcific components.

References

[1] World Health Organization. Cardiovascular diseases (CVDs). Internet: http://www.who.int/mediacentre/factsheets/fs317/en/, January 2015 [May 11, 2015].

[2] American Heart Association Statistics Committee and Stroke Statistics Subcommittee. Heart Disease, Stroke and Research Statistics At-a-Glance. Internet: http://www.heart.org/idc/groups/ahamah-public/@wcm/@sop/@smd/documents/downloadable/ucm480086.pdf, December 16, 2015 [May 11, 2015].

[3] Statistics South Africa. Mortality and causes of death in South Africa, 2011: Findings from death notification. *Statistical Release Publication,* vol. 309, 2014.

[4] F. H. Netter. *Atlas of Human Anatomy.* Philadelphia, PA: Elsevier Health Sciences, 2010.

[5] M. D. Seckeler and T. R. Hoke. The worldwide epidemiology of acute rheumatic fever and rheumatic heart disease. *Journal of Clinical Epidemiology,* vol. 3, pp. 67-84, 2011.

[6] Johns Hopkins Medicine Health Library. Anatomy and Function of the Heart Valves. Internet: http://www.hopkinsmedicine.org/healthlibrary/conditions/cardiovascular diseases/anatomy and function of the heart valves 85,P00252/, 2015 [June 23, 2015].

[7] V. T. Nkomo. Epidemiology and prevention of valvular heart diseases and infective endocarditis in Africa. *Heart,* vol. 93, pp. 1510-1519, 2007.

[8] B. Iung, G. Baron, E. G. Butchart, F. Delahaye, C. Gohlke-Barwolf, O. W. Levang, P. Tornos, J. L. Vanoverschelde, F. Vermeer, E. Boersma, P. Ravaud and A. Vahanian. A prospective survey of patients with valvular heart disease in Europe: The Euro Heart Survey on Valvular Heart Disease. *European Heart Journal,* vol. 24, pp. 1231-1243, 2003.

[9] A. Malhotra. The Changing Burden of Valvular Heart Disease. Internet: http://www.bcs.com/pages/news_full.asp?NewsID=19792059, June 7, 2012 [May 11, 2015].

[10] A. Cribier. Percutaneous Implantation of Aortic Valve Prostheses in Patients with Calcific Aortic Stenosis–Technical Advances. *ICR,* vol. 2, pp. 68-69, 2007.

[11] U.S. National Library of Medicine. Aortic valve surgery - open. Internet: https://www.nlm.nih.gov/medlineplus/ency/article/007408.htm, August 8, 2015 [May 19, 2015].

[12] Michigan Heart & Vascular Specialists. Minimally Invasive Surgery. Internet: http://www.michiganhvs.com/surgery/minimally-invasive-surgery.html, 2015 [July 20, 2015].

[13] J. Dominik and P. Zacek. *Heart Valve Surgery: An Illustrated Guide.* Heidelberg, DE: Springer Science & Business Media, 2010.

[14] P. Pibarot and J. G. Dumesnil. Prosthetic heart valves: selection of the optimal prosthesis and long-term management. *Circulation,* vol. 119, pp. 1034-1048, 2009.

[15] A. Cribier. Development of transcatheter aortic valve implantation (TAVI): a 20-year odyssey. *Archives of Cardiovascular Diseases,* vol. 105, pp. 146-152, 2012.

[16] H. Davies. Catheter-mounted valve for temporary relief of aortic insufficiency. *The Lancet,* vol. 285, pp. 250, 1965.

[17] S. Phillips, M. Ciborski, P. Freed, P. Cascade and D. Jaron. A temporary catheter-tip aortic valve: hemodynamic effects on experimental acute aortic insufficiency. *Annals of Thoracic Surgery,* vol. 21, pp. 134-137, 1976.

[18] H. R. Andersen, L. L. Knudsen and J. M. Hasenkam. Transluminal implantation of artificial heart valves-Description of a new expandable aortic valve and initial results with implantation by catheter technique in closed chest pigs. *European Heart Journal,* vol. 13, pp. 704-708, 1992.

[19] P. Bonhoeffer, Y. Boudjemline, Z. Saliba, J. Merckx, Y. Aggoun, D. Bonnet, P. Acar, J. Le Bidois, D. Sidi and J. Kachaner. Percutaneous replacement of pulmonary valve in a right-ventricle to pulmonary-artery prosthetic conduit with valve dysfunction. *The Lancet,* vol. 356, pp. 1403-1405, 2000.

[20] D. Stoeckel, A. Pelton and T. Duerig. Self-expanding nitinol stents: material and design considerations. *European Radiology,* vol. 14, pp. 292-301, 2004.

[21] Edwards Lifesciences-NewHeartValve. Treatment Options for Severe Aortic Stenosis (SAS). Internet: http://newheartvalve.com/severe-aortic-stenosis-treatment-options, 2015 [July 20, 2015].

[22] J. L. Zamorano, A. Goncalves and R. Lang. Imaging to select and guide transcatheter aortic valve implantation. *European Heart Journal,* vol. 35, pp. 1578-1587, 2014.

[23] A. M. Kasel, S. Cassese, S. Bleiziffer, M. Amaki, R. T. Hahn, A. Kastrati and P. P. Sengupta. Standardized imaging for aortic annular sizing: implications for transcatheter valve selection. *JACC: Cardiovascular Imaging,* vol. 6, pp. 249-262, 2013.

[24] S. Achenbach, V. Delgado, J. Hausleiter, P. Schoenhagen, J. K. Min and J. A. Leipsic. SCCT expert consensus document on computed tomography imaging before transcatheter aortic valve implantation (TAVI)/transcatheter aortic valve replacement (TAVR). *Cardiovascular Computed Tomography,* vol. 6, pp. 366-380, 2012.

[25] P. W. Serruys, N. Piazza, A. Cribier, J. Webb, J. Laborde and P. de Jaegere. *Transcatheter Aortic Valve Implantation: Tips and Tricks to Avoid Failure.* New York, USA: CRC Press, 2010.

[26] A. Selle, H. R. Figulla, M. Ferrari, W. Rademacher, B. Goebel, A. Hamadanchi, M. Franz, A. Schlueter, T. Lehmann and A. Lauten. Impact of rapid ventricular pacing during TAVI on microvascular tissue perfusion. *Clinical Research in Cardiology,* vol. 103, pp. 902-911, 2014.

[27] J. G. Webb, S. Pasupati, K. Humphries, C. Thompson, L. Altwegg, R. Moss, A. Sinhal, R. G. Carere, B. Munt, D. Ricci, J. Ye, A. Cheung and S. V. Lichtenstein. Percutaneous transarterial aortic valve replacement in selected high-risk patients with aortic stenosis. *Circulation,* vol. 116, pp. 755-763, 2007.

[28] E. Grube, G. Schuler, L. Buellesfeld, U. Gerckens, A. Linke, P. Wenaweser, B. Sauren, F. Mohr, T. Walther and B. Zickmann. Percutaneous aortic valve replacement for severe aortic stenosis in high-risk patients using the second-and

current third-generation self-expanding CoreValve prosthesis: device success and 30-day clinical outcome. *American College of Cardiology,* vol. 50, pp. 69-76, 2007.

[29] P. Y. Pang, P. T. Chiam, Y. L. Chua and Y. K. Sin. A survivor of late prosthesis migration and rotation following percutaneous transcatheter aortic valve implantation. *European Journal of Cardiothoracic Surgery,* vol. 41, pp. 1195-1196, 2012.

[30] T. E. David. Aortic valve sparing operations. *Annals of Thoracic Surgery,* vol. 73, pp. 1029-1030, 2002.

[31] Q. Wang, E. Sirois and W. Sun. Patient-specific modeling of biomechanical interaction in transcatheter aortic valve deployment. *Journal of Biomechanics,* vol. 45, pp. 1965-1971, 2012.

[32] R. E. Clark and G. A. Butterworth. Characterization of the mechanics of human aortic and mitral valve leaflets. *Surgical Forum,* vol. 22, pp. 134-136, 1971.

[33] R. E. Clark. Stress-strain characteristics of fresh and frozen human aortic and mitral leaflets and chordae tendineae. Implications for clinical use. *Journal of Thoracic Cardiovascular Surgery,* vol. 66, pp. 202-208, 1973.

[34] K. Balachandran, P. Sucosky and A. P. Yoganathan. Hemodynamics and mechanobiology of aortic valve inflammation and calcification. *International Journal of Inflammation,* vol. 2011, pp. 1-15, 2011.

[35] C. Martin and W. Sun. Biomechanical characterization of aortic valve tissue in humans and common animal models. *Biomedical Materials Research Part A,* vol. 100, pp. 1591-1599, 2012.

[36] K. L. Billiar and M. S. Sacks. Biaxial mechanical properties of the natural and glutaraldehyde treated aortic valve cusp—part I: experimental results. *Journal of Biomechanical Engineering,* vol. 122, pp. 23-30, 2000.

[37] C. Martin, T. Pham and W. Sun. Significant differences in the material properties between aged human and porcine aortic tissues. *European Journal of Cardiothoracic. Surgery,* vol. 40, pp. 28-34, 2011.

[38] Y. C. Fung, K. Fronek and P. Patitucci. Pseudoelasticity of arteries and the choice of its mathematical expression. *American Journal of Physiology,* vol. 237, pp. H620-31, 1979.

[39] G. A. Holzapfel, T. C. Gasser and R. W. Ogden. A new constitutive framework for arterial wall mechanics and a comparative study of material models. *Journal of Elasticity and the Physical Science of Solids,* vol. 61, pp. 1-48, 2000.

[40] R. Ogden. Large deformation isotropic elasticity-on the correlation of theory and experiment for incompressible rubberlike solids. *Proceedings of the Royal Society of London A: Mathematical, Physical and Engineering Sciences,* 1972, pp. 565-584.

[41] O. Yeoh. Some forms of the strain energy function for rubber. *Rubber Chemistry and Technology,* vol. 66, pp. 754-771, 1993.

[42] T. C. Gasser, R. W. Ogden and G. A. Holzapfel. Hyperelastic modelling of arterial layers with distributed collagen fibre orientations. *Journal of the Royal Society Interface,* vol. 3, pp. 15-35, 2006.

[43] E. Trowbridge, M. Black and C. Daniel. The mechanical response of glutaraldehyde-fixed bovine pericardium to uniaxial load. *Journal of Material Science,* vol. 20, pp. 114-140, 1985.

[44] J. M. Lee, S. A. Haberer and D. R. Boughner. The bovine pericardial xenograft: I. Effect of fixation in aldehydes without constraint on the tensile viscoelastic properties of bovine pericardium. *Journal of Biomedical Material Research,* vol. 23, pp. 457-475,

1989.

[45] M. Mooney. A theory of large elastic deformation. *Journal of Applied Physics,* vol. 11, pp. 582-592, 1940.

[46] R. Rivlin, Large elastic deformations of isotropic materials. IV. Further developments of the general theory. *Philosophical Transactions of the Royal Society of London A: Mathematical, Physical and Engineering Sciences,* vol. 241, pp. 379-397, 1948.

[47] S. Morganti. Finite Element Analysis of Aortic Valve Surgery. Doctoral thesis, Universita degli Studi di Pavia, Italy, 2011.

[48] S. Morganti, M. Conti, M. Aiello, A. Valentini, A. Mazzola, A. Reali and F. Auricchio. Simulation of transcatheter aortic valve implantation through patient-specific finite element analysis: two clinical cases. *Journal of Biomechanics.* vol. 47, pp. 2547-2555, 2014.

[49] F. Auricchio, M. Conti, S. Morganti and A. Reali. Simulation of transcatheter aortic valve implantation: a patient-specific finite element approach. *Computer Methods in Biomechanics and Biomedical Engineering,* vol. 17, pp. 1347-1357, 2014.

[50] C. Capelli, G. Bosi, E. Cerri, J. Nordmeyer, T. Odenwald, P. Bonhoeffer, F. Migliavacca, A. Taylor and S. Schievano. Patient-specific simulations of transcatheter aortic valve stent implantation. *Medical and Biological Engineering and Computing,* vol. 50, pp. 183-192, 2012.

[51] M. J. Underwood, G. El Khoury, D. Deronck, D. Glineur and R. Dion. The aortic root: structure, function, and surgical reconstruction. *Heart,* vol. 83, pp. 376-380, Apr, 2000.

[52] R. H. Anderson. The surgical anatomy of the aortic root. *Multimedia Manual of Cardio-Thoracic Surgery,* vol. 2007, pp. mmcts. 2006.002527, 2007.

[53] E. A. Miranda. Nodules of Arantius. Internet: http://clinanat.com/mtd/705-nodules-of-arantius, January 20, 2015 [July 2, 2015].

[54] Sauren, Alfons Aloisius Henricus Johannes, The Mechanical Behaviour of the Aortic Valve. Doctoral thesis, Technische Hogeschool Eindhoven, 1981.

[55] J. A. Leopold. Cellular mechanisms of aortic valve calcification. *Circulation: Cardiovascular Intervention,* vol. 5, pp. 605-614, 2012.

[56] A. Cheung and K. M. Lichtenstein. Illustrated techniques for transapical aortic valve implantation. *Annals of Cardiothoracic Surgery,* vol. 1, pp. 231, 2012.

[57] J. De Hart, G. Peters, P. Schreurs and F. Baaijens. A three-dimensional computational analysis of fluid–structure interaction in the aortic valve. *Journal of Biomechanics,* vol. 36, pp. 103-112, 2003.

[58] D. U. Silverthorn, W. C. Ober, C. W. Garrison, A. C. Silverthorn and B. R. Johnson. *Human Physiology: An Integrated Approach.* San Francisco, CA: Pearson/Benjamin Cummings, 2009.

[59] I. Vesely. The role of elastin in aortic valve mechanics. *Journal of Biomechanics,* vol. 31, pp. 115-123, 1997.

[60] L. Wallby. Signs of inflammation in different types of heart valve disease: The VOCIN study. Doctoral thesis, Linkoping University, 2008.

[61] R. I. Bashey, S. Torii and A. Angrist. Age-related collagen and elastin content of human heart valves. *Journal of Gerontology,* vol. 22, pp. 203-208, 1967.

[62] J. De Hart, G. Peters, P. Schreurs and F. Baaijens. Collagen fibres reduce stresses and stabilize motion of aortic valve leaflets during systole. *Journal of Biomechanics,* vol. 37, pp. 303-311, 2004.

[63] J. De Hart, G. Cacciola, P. Schreurs and G. Peters. A three-dimensional analysis of a fibre-reinforced aortic valve prosthesis. *Journal of Biomechanics,* vol. 31, pp. 629-638, 1998.

[64] G. R. Cacciola. Design, Simulation and Manufacturing of Fibre Reinforced Polymer Heart Valves. Doctoral thesis, Technische Universiteit Eindhoven, 1998.

[65] A. Tsamis, J. T. Krawiec and D. A. Vorp. Elastin and collagen fibre microstructure of the human aorta in ageing and disease: a review. *Journal of the Royal Society Interface,* vol. 10, 2013.

[66] M. J. Thubrikar, *The Aortic Valve.* New York, USA: CRC press, 1989.

[67] A. Cataloglu, R. E. Clark and P. L. Gould. Refined stress analysis of human aortic heart valves. *Journal of the Engineering Mechanics Division,* vol. 102, pp. 135-150, 1976.

[68] M. Back, T. C. Gasser, J. B. Michel and G. Caligiuri. Biomechanical factors in the biology of aortic wall and aortic valve diseases. *Cardiovascular Research,* vol. 99, pp. 232-241, 2013.

[69] T. Smith and British Medical Association. *The British Medical Association Complete Family Health Encyclopedia.* London: Dorling Kindersley, 1995.

[70] Cleveland Clinic. Bicuspid Aortic Valve Disease. Internet: http://my.clevelandclinic.org/services/heart/disorders/heart-valve-disease/bicuspid_aortic_valve_disease, 2015 [June 16, 2015].

[71] H. Baumgartner, J. Hung, J. Bermejo, J. B. Chambers, A. Evangelista, B. P. Griffin, B. Iung, C. M. Otto, P. A. Pellikka, M. Quinones and EAE/ASE. Echocardiographic assessment of valve stenosis: EAE/ASE recommendations for clinical practice. *European Journal of Echocardiography.* vol. 10, pp. 1-25, 2009.

[72] M. R. Dweck, N. A. Boon and D. E. Newby. Calcific aortic stenosis: a disease of the valve and the myocardium. *Journal of American College of Cardiology,* vol. 60, pp. 1854-1863, 2012.

[73] G. A. Holzapfel. Biomechanics of soft tissue. *The Handbook of Materials Behavior Models,* vol. 3, pp. 1049-1063, 2001.

[74] F. Wuyts, V. Vanhuyse, G. Langewouters, W. Decraemer, E. Raman and S. Buyle. Elastic properties of human aortas in relation to age and atherosclerosis: a structural model. *Physics in Medicine and Biology,* vol. 40, pp. 1577, 1995.

[75] N. R. Mollet, F. Cademartiri and P. J. de Feyter. Non-invasive multislice CT coronary imaging. *Heart,* vol. 91, pp. 401-407, 2005.

[76] Simpleware. Internet: http://www.simpleware.com/software/scanip/, 2015 [July 21, 2015].

[77] R. D. Cook, *Finite Element Modeling for Stress Analysis.* US: Wiley, 1995.

[78] Q. Wang, S. Kodali, C. Primiano and W. Sun. Simulations of transcatheter aortic valve implantation: implications for aortic root rupture. *Biomechanics and Modeling in Mechanobiology,* vol. 14, pp. 29-38, 2015.

[79] Dassault Systemes. Abaqus v6.13 Online Documentation. Internet: http://129.97.46.200:2080/v6.13, Simulia Corp, 2013

[80] T. J. R. Hughes. *The Finite Element Method: Linear Static and Dynamic Finite Element Analysis.* New Jersey: Prentice-Hall, Inc, 1987.

[81] M. Niinomi, T. Narushima and M. Nakai. *Advances in Metallic Biomaterials.* Heidelberg, DE: Springer, 2015.

[82] C. W. De Silva, *Vibration and Shock Handbook.* New York, USA: CRC Press, 2005.

[83] R. Marlow, A general first-invariant hyperelastic constitutive model. *Constitutive Models for Rubber,* pp. 157-160, 2003.

[84] J. A. Grogan, S. B. Leen and P. E. McHugh. Comparing coronary stent material performance on a common geometric platform through simulated bench testing. *Journal of the Mechanical Behavior of Biomedical Materials,* vol. 12, pp. 129-138, 2012.

[85] S. B. King and A. C. Yeung. *Interventional Cardiology.* New York: McGraw-Hill Medical, 2007.

[86] S. Pant, N. W. Bressloff and G. Limbert, Geometry parameterization and multidisciplinary constrained optimization of coronary stents, *Biomechanics and Modeling in Mechanobiology,* vol. 11, pp. 61-82, 2012.

[87] F. Auricchio, M. Conti, A. Ferrara, S. Morganti and A. Reali. Patient-specific simulation of a stentless aortic valve implant: the impact of fibres on leaflet performance. *Computer Methods in Biomechanics and Biomedical Engineering,* vol. 17, pp. 277-285, 2014.

[88] T. Koch, B. D. Reddy, P. Zilla and T. Franz. Aortic valve leaflet mechanical properties facilitate diastolic valve function. *Computer Methods in Biomechanics and Biomedical Engineering,* vol. 13, pp. 225-234, 2010.

[89] R. Haj-Ali, G. Marom, S. B. Zekry, M. Rosenfeld and E. Raanani. A general three-dimensional parametric geometry of the native aortic valve and root for biomechanical modeling. *Journal of Biomechanics,* vol. 45, pp. 2392-2397, 2012.

[90] F. Auricchio, M. Conti, S. Demertzis and S. Morganti. Finite element analysis of aortic root dilation: a new procedure to reproduce pathology based on experimental data. *Computer Methods in Biomechanics and Biomedical Engineering,* vol. 14, pp. 875-882, 2011.

[91] P. Stradins, R. Lacis, I. Ozolanta, B. Purina, V. Ose, L. Feldmane and V. Kasyanov. Comparison of biomechanical and structural properties between human aortic and pulmonary valve. *European Journal of Cardiothoracic Surgery,* vol. 26, pp. 634-639, 2004.

[92] G. A. Holzapfel. *Nonlinear Solid Mechanics.* Chichester: Wiley, 2000.

Appendix A

The approval of the University of Cape Town's Ethics Committee on the usage of the MSCT images

UNIVERSITY OF CAPE TOWN
Faculty of Health Sciences
Human Research Ethics Committee

Room E52-24 Old Main Building
Groote Schuur Hospital
Observatory 7925
Telephone [021] 406 6338 • **Facsimile** [021] 406 6411
Email: sumayah.ariefdien@uct.ac.za
Website: www.health.uct.ac.za/fhs/research/humanethics/forms

14 August 2015

HREC REF: 365/2015

Dr J Scherman
Department of Surgery
Chris Barnard Division of Cardiothoracic Surgery
D-24
NGSH

Dear Dr Scherman

PROJECT TITLE: THREE-DIMENSIONAL COMPUTED TOMOGRAPHY GEOMETRY OF THE AORTIC ROOT IN PATIENTS SCREENED FOR TRANSCATHETER AORTIC VALVE IMPLANTATION (MSc Candidate – Mr M Shirzadi)

Thank you for your response letter dated 31 July 2015, addressing the issues raised by the Human Research Ethics Committee (HREC).

It is a pleasure to inform you that the HREC has formally approved the above-mentioned study.

Approval is granted for one year until the 30th August 2016.

Please submit a progress form, using the standardised Annual Report Form if the study continues beyond the approval period. Please submit a Standard Closure form if the study is completed within the approval period.
(Forms can be found on our website: www.health.uct.ac.za/fhs/research/humanethics/forms)

We acknowledge that the following student: Mehdi Shirzadi is also involved in this project.

Please quote the HREC reference no in all your correspondence.

Please note that the ongoing ethical conduct of the study remains the responsibility of the principal investigator.

Yours sincerely

PROFESSOR M BLOCKMAN
CHAIRPERSON, FHS HUMAN RESEARCH ETHICS COMMITTEE
Federal Wide Assurance Number: FWA00001637.
Institutional Review Board (IRB) number: IRB00001938

Hrec/ref:365/2015

This serves to confirm that the University of Cape Town Research Ethics Committee complies to the Ethics Standards for Clinical Research with a new drug in patients, based on the Medical Research Council (MRC-SA), Food and Drug Administration (FDA-USA), International Convention on Harmonisation Good Clinical Practice (ICH GCP) and Declaration of Helsinki guidelines.

The Research Ethics Committee granting this approval is in compliance with the ICH Harmonised Tripartite Guidelines E6: Note for Guidance on Good Clinical Practice (CPMP/ICH/135/95) and FDA Code Federal Regulation Part 50, 56 and 312.

ERi F cutty: As ment of E:th In R -arch Pro cts

Any person planning to undertake research in the Faculty of Engineering and the Built Environment at the University of Cape Town is required to complete this form before collecting or analysing data. When completed it should be submitted to the supervisor (where applicable) and from there to the Head of Department. If any of the questions be been answered YES, and the applicant is NOT a fourth year student, the Head should forward this form for app ie Faculty EIR committee: submit to Ms Zakiya Chikte (Zakiya.chikte@uct.ac.za); New EBE Building, Ph 0 39).

Please note – It is important to keep a signed copy of this form as students must include pyo1 J!le **completed form** wr 1w llOnimNI'Si t **a Mlliim** itbol!I illmin:2tic,

Name of Principal Researcher/Student: M. Shirzadi **Department:** M

If a Student: **Degree:** MSc Mec Eng **Upti'Y :or.** fh, . , . ..\J

If a Research Contract indicate source of funding/sponsorship:

Rona,ch RlfOJoct TI r.: O q" '\\- o l h\..f - c "l. 'k e\.t-1,.\ Mo:b. o i vr PeaJvrt.

O •rt - - or Itihlca• ,lo you"" ch PIIIOJ

Question 1: Is there a possibility that your research could cause harm to a third party (i.e. a person not involved in your project)?	YES	NO
Question 2: Is your research making use of human subjects as sources of data? If your answer is YES, please complete Addendum 2.	YES	NO
Question 3: Does your research involve the participation of or provision of services to communities? If your answer is YES, please complete Addendum 3.	YES	NO
Question 4: If your research is sponsored, is there any potential for conflicts of interest? If your answer is YES, please complete Addendum 4.	YES	NO

If you have answered YES to any of the above questions, please append a copy of your research proposal, as well as any interview schedules or questionnaires (Addendum 1) and please complete further addenda as appropriate.

hereby undertake to carry out my research In such i way th.at

- there is no apparent legal objection to the nature or the method of research; and
- the research will not compromise staff or students or the other responsibilities of the University;
- the stated objective will be achieved, and the findings will have a high degree of validity;
- limitations and alternative interpretations will be considered;
- the findings could be subject to peer review and publicly available; and
- I will comply with the conventions of copyright and avoid any practice that would constitute plagin m.

Signed by:

Principal Researcher/Student:	Full name and signature	
	M°'na.... J Mehdi Gk:,z:	1/2/2016

This application is approved by:

Supervisor (if applicable):		1/2/2016
HOD (or delegated nominee): Final authority for all assessments with NO to all questions and for all undergraduate research.		03/02/2016
Chair : Faculty EIR Committ For applicants other than und students who have answered of the above questions.		

ADDENDUM 1:
Please append a copy of the research proposal here, as well as any interview schedules or questionnaires:

ADDENDUM 2: To be completed if you answered YES to Question 2:

It is assumed that you have read the UCT Code for Research involving Human Subjects (available at http://web.uct.ac.za/depts/educate/download/uctcodeforresearchinvolvinghumansubjects.pdf) in order to be able to answer the questions in this addendum.

2.1 Does the research discriminate against participation by individuals, or differentiate between participants, on the grounds of gender, race or ethnic group, age range, religion, income, handicap, illness or any similar classification?	YES	NO
2.2 Does the research require the participation of socially or physically vulnerable people (children, aged, disabled, etc) or legally restricted groups?	YES	NO
2.3 Will you not be able to secure the informed consent of all participants in the research? (In the case of children, will you not be able to obtain the consent of their guardians or parents?)	YES	NO
2.4 Will any confidential data be collected or will identifiable records of individuals be kept?	YES	NO
2.5 In reporting on this research is there any possibility that you will not be able to keep the identities of the individuals involved anonymous?	YES	NO
2.6 Are there any foreseeable risks of physical, psychological or social harm to participants that might occur in the course of the research?	YES	NO
2.7 Does the research include making payments or giving gifts to any participants?	YES	NO

If you have answered YES to any of these questions, please describe how you plan to address these issues (append to form):

ADDENDUM 3: To be completed if you answered YES to Question 3:

3.1 Is the community expected to make decisions for, during or based on the research?	YES	NO
3.2 At the end of the research will any economic or social process be terminated or left unsupported, or equipment or facilities used in the research be recovered from the participants or community?	YES	NO
3.3 Will any service be provided at a level below the generally accepted standards?	YES	NO

If you have answered YES to any of these questions, please describe how you plan to address these issues (append to form)

ADDENDUM 4: To be completed if you answered YES to Question 4

4.1 Is there any existing or potential conflict of interest between a research sponsor, academic supervisor, other researchers or participants?	YES	NO
4.2 Will information that reveals the identity of participants be supplied to a research sponsor, other than with the permission of the individuals?	YES	NO
4.3 Does the proposed research potentially conflict with the research of any other individual or group within the University?	YES	NO

If you have answered YES to any of these questions, please describe how you plan to address these issues(append to form)

Appendix B

The stress-strain data used in the constitutive material models of the stent and the prosthetic leaflets

Table B.1 *The post-yield material data of MP35N alloy (from SAT)*

True Stress(MPa)	True Plastic Strain
599	0.04879
704	0.09531
906	0.182322
1090	0.262364
1250	0.336472
1400	0.405465
1520	0.470004

Table B.2 *The summarised stress-strain results of the uniaxial test, conducted by SAT on the type of polymer that the prosthetic leaflets are made form, for characterizing its mechanical response.*

Nominal Stress (MPa)	Nominal Strain
0.027636357	0.029020486
0.088279956	0.034022725
0.169897955	0.03903433
0.247695664	0.044045935
0.325292392	0.049057554
0.398684101	0.054069155
0.472678756	0.059071403
0.545181729	0.064073651
0.615830379	0.069075854
0.682588492	0.074078103
//	//
43.30065449	5.376641187
43.38173984	5.38165018
43.46668121	5.386663669
43.54146169	5.391663669
43.62232343	5.396668165
0.074453995	5.401677158
0.062993237	5.406681655
0.060698227	5.411695144
0.060267358	5.416704137
0.056638015	5.421708633
0.055983583	5.426605216